ELOINY GUIMARÃES BARBOSA

SOLAR THERMAL ENERGY COLLECTION BY COMPOUND PARABOLIC COLLECTOR AND ITS STORAGE IN A PACKED-BED SYSTEM: NUMERICAL AND EXPERIMENTAL ANALYSIS

Thesis submitted to the Agricultural Engineering Graduate Program of the Universidade Federal de Viçosa in partial fulfillment of the requirements for the degree of *Doctor Scientiae*.

Adviser: Marcio Arêdes Martins

VIÇOSA - MINAS GERAIS
2023

Ficha catalográfica elaborada pela Biblioteca Central da Universidade Federal de Viçosa - Campus Viçosa

T
B238s
2023

Barbosa, Eloiny Guimarães, 1994-
Solar thermal energy collection by compound parabolic collector and its storage in a packed-bed system: numerical and experimental analysis / Eloiny Guimarães Barbosa. – Viçosa, MG, 2023.
1 tese eletrônica (144 f.): il. (algumas color.).

Texto em inglês.
Orientador: Márcio Arêdes Martins.
Tese (doutorado) - Universidade Federal de Viçosa, Departamento de Engenharia Agrícola, 2023.
Inclui bibliografia.
DOI: https://doi.org/10.47328/ufvbbt.2023.531
Modo de acesso: World Wide Web.

1. Energia solar. 2. Energia - Armazenamento. 3. Coletores solares. I. Martins, Márcio Arêdes, 1972-. II. Universidade Federal de Viçosa. Departamento de Engenharia Agrícola. Programa de Pós-Graduação em Engenharia Agrícola. III. Título.

CDD 22. ed. 621.47

Bibliotecário(a) responsável: Alice Regina Pinto Pires CRB-6/2523

ELOINY GUIMARÃES BARBOSA

SOLAR THERMAL ENERGY COLLECTION BY COMPOUND PARABOLIC COLLECTOR AND ITS STORAGE IN A PACKED-BED SYSTEM: NUMERICAL AND EXPERIMENTAL ANALYSIS

Thesis submitted to the Agricultural Engineering Graduate Program of the Universidade Federal de Viçosa in partial fulfillment of the requirements for the degree of *Doctor Scientiae*.

APPROVED: July 27, 2023.

Assent:

gov.br Documento assinado digitalmente
ELOINY GUIMARAES BARBOSA
Data: 01/09/2023 13:38:24-0300
Verifique em https://validar.iti.gov.br

Eloiny Guimarães Barbosa
Author

gov.br Documento assinado digitalmente
MARCIO AREDES MARTINS
Data: 01/09/2023 15:57:55-0300
Verifique em https://validar.iti.gov.br

Marcio Arêdes Martins
Adviser

ACKNOWLEDGEMENTS

Becoming a Doctor in Agricultural Engineering has been a dream that started years ago when I discovered the potential to contribute to the advancement of humanity through research. I have always believed that progress flourishes first in academia before spreading to industry or the field. Throughout this long journey, I have met people who played an indispensable role in making this dream a reality. To them, I express my sincerest gratitude.

I once heard that when given the opportunity to express gratitude, it is best to do so. Therefore, I would like to take this chance to express my appreciation...

First and foremost, I am grateful to God, my refuge and strength. You are the beginning and the end of all wisdom, and without You, none of this would have been possible. When faced with storms, Your mighty hand sustained me and remained my unshakable foundation in every moment.

To my parents and siblings, the pillars of my life, thank you for your unconditional love and unwavering dedication. Despite the physical distance, your support and encouragement have been my guiding light during the most challenging times.

To Marcos, my life partner and academic companion, for his love, care, and dedication. From the days spent assembling the experiment under the sun to sleepless nights, your constructive criticism, valuable suggestions, and immeasurable patience have been invaluable. You have been my greatest source of encouragement, often setting aside your own concerns to support me. The strength of our connection and our mutual dedication reassure me that we can overcome any challenge that life presents. Together, we are an unstoppable force.

To Professor Marcio Arêdes Martins, who not only shared his distinguished knowledge and experience but also inspiring me to strive for higher academic achievements. Professor, your dedication and guidance have contributed to both my academic and personal growth in immeasurable ways. Thank you for opening doors I never thought possible. With utmost certainty, I can say that I am leaving UFV with the finest education I could have received. I will always remember the impact you have had on my life.

To Professor Paulo Cesar Corrêa and Professor Tetuo Hara, for always welcoming me into their laboratory and providing invaluable guidance that has made a significant difference in this journey. Their cheerful personalities, ability to see positivity in every situation, and willingness to share motivating (and very funny) stories have truly made my time in their lab a memorable experience. I am grateful for the opportunity to have spent time with both of you, professors.

To Professor Maria Joselma de Moraes, the first person to believe in my potential at the beginning of my academic journey, thank you for teaching, motivating, and always cheering me on. You have played an indispensable role in shaping my education and in my personal life. I am grateful for the trust and bond we have developed throughout this journey.

To my friends at the Biofuels Laboratory, thank you for the exchange of knowledge and assistance. A special thanks to Javier, someone I had the privilege of meeting during my doctorate and who has become a great friend. Thank you for making this journey an incredible experience filled with countless laughs and fond memories.

To the women's handball team of the Academic Athletic Association of UFV (LUVE), thank you for making this journey lighter, enjoyable, and victorious. This experience allowed me to add one of the best parts of my life, handball, into my academic journey.

To the University of Illinois at Urbana-Champaign, the Environment-Enhancing Energy (E2-E) Laboratory, and especially Professor Yuanhui Zhang, thank you for providing me with an unique growth experience, expanding my academic horizons, and showing me the incredible possibilities of interdisciplinary research.

To the Federal University of Viçosa and the Department of Agricultural Engineering for the opportunity to pursue this course.

This study was financed in part by the Coordenação de Aperfeiçoamento de Pessoal de Nível Superior – Brasil (CAPES) – Finance Code 001.

To the Conselho Nacional de Desenvolvimento Científico e Tecnológico (CNPq), thank you for granting me the doctoral scholarship (grant 141368/2019-5) and the doctoral sandwich international scholarship (grant 202655/2020-2).

"If I have seen further, it is by standing on the shoulders of Giants".

(Isaac Newton)

BIOGRAPHY

Eloiny Guimarães Barbosa, daughter of Vanderley Ferreira Barbosa and Aparecida Luiz Guimarães, was born on May 6, 1994, in the city of Anápolis, Goiás, Brazil.

In August 2012, she began her undergraduate studies in Agricultural Engineering at the State University of Goiás (UEG) and completed her degree in July 2017. From August 2013 to July 2017, she was engaged in research projects at the same university.

In August 2017, she joined the Graduate Program in Agricultural Engineering at the Federal University of Viçosa, specializing in Energy in Agriculture, pursuing a Master's degree. In February 2019, she successfully defended her dissertation to obtain the title of *Magister Scientiae*.

From 2018 to 2021, she was a member of the women's handball team of the Academic Athletic Association of UFV (LUVE) and became a two-time champion of the state university championship (Jogos Universitários Mineiros – JUMS) in 2018 and 2019.

In March 2019, she enrolled in the Graduate Program in Agricultural Engineering at the Federal University of Viçosa, continuing her studies in the field of Energy in Agriculture at the doctoral level. From April 2022 to March 2023, she conducted a doctoral sandwich program at the University of Illinois at Urbana-Champaign in the United States. In July 2023, she successfully defended her thesis to obtain the title of *Doctor Scientiae*.

"For from ***Him*** and ***through Him*** and to ***Him*** are ***all things***"
(Romans 11:36)

GENERAL ABSTRACT

BARBOSA, Eloiny Guimarães, D.Sc., Universidade Federal de Viçosa, July, 2023. **Solar thermal energy collection by compound parabolic collector and its storage in a packed-bed system: numerical and experimental analysis**. Adviser: Marcio Arêdes Martins.

The use of renewable energy sources is crucial for maintaining the sustainability of the planet, reducing reliance on finite resources, and mitigating the environmental consequences of fossil fuel combustion. Among the various avenues of solar energy utilization, solar thermal energy has gained increasing prominence. Thermal storage systems have significantly enhanced the reliability and predictability of solar systems. This study aimed to establish parameters, explore different dryer configurations, and highlight the importance of thermal energy storage methods. Additionally, the thermal and economic performance of a U-tube compound parabolic collector (CPC) was evaluated in a prototype. Different filling fluids (water, air, and thermal oil) within the evacuated tube and varying mass flow rates (0.007, 0.009, 0.014, and 0.021 kg s^{-1}) were examined. In the final section, a numerical evaluation was conducted on a packed bed thermal energy storage (PBTES) system. The optimization of this system considered various heat storage materials (concrete, quartzite rock, and cast iron) and particle sizes (0.02, 0.03, and 0.04 m). The evaluated CPC collector demonstrated an optical efficiency of approximately 63.6%. The use of thermal oil as the filling fluid led to a higher average thermal efficiency (41.2%) compared to water (31.7%) and air (31.1%). The lowest evaluated mass flow rate resulted in the highest average thermal efficiency (41.2%). Regarding the PBTES analysis, the utilization of materials with lower thermal conductivity led to an increased temperature difference between the heat transfer fluid and the solid material. The configuration of multilayer materials had a significant impact on loading and unloading times, as well as on stored and released thermal energy. Among the cases evaluated, Case 9 exhibited the highest stored thermal energy (27.2 MJ) and demonstrated commendable charge (87.5%), discharge (80.5%), and exergy (70.5%) efficiencies. Clearly, the variability in particle diameter and material type had a substantial influence on stratification and heat transfer within the PBTES.

Keywords: Environmentally friendly system. Evacuated U tube solar collector. Renewable and sustainable energy. Solar energy. Thermocline thermal storage system.

RESUMO GERAL

BARBOSA, Eloiny Guimarães, D.Sc., Universidade Federal de Viçosa, julho de 2023. **Coleta de energia solar térmica por um coletor parabólico composto e seu armazenamento num sistema de leito compactado: análise numérica e experimental**. Orientador: Marcio Arêdes Martins.

O uso de fontes de energia renováveis é essencial para garantir a sustentabilidade do planeta, reduzindo a dependência de recursos finitos e minimizando os impactos ambientais causados pelo uso de combustíveis fosseis. Dentre os tipos de aproveitamento da energia solar, a energia solar térmica tem ganhado cada vez mais atenção. Os sistemas de armazenamento térmico têm aumentado a confiabilidade e melhorado a previsibilidade dos sistemas solares. Esse estudo objetivou fornecer parâmetros, abordar diferentes tipos de secadores e enfatizar a importância dos métodos de armazenamento de energia térmica. Além disso, o desempenho térmico e econômico de um coletor parabólico composto (CPC) com tubo em U foi avaliado em um protótipo. Diferentes fluidos de enchimento do tubo evacuado (água, ar e óleo térmico) e diferentes vazões mássicas (0,007, 0,009, 0,014 e 0,021 kg s^{-1}) foram avaliados. No tópico final, um sistema de armazenamento térmico de leito empacotado (PBTES) foi avaliado numericamente. A otimização desse sistema avaliou diferentes materiais de armazenamento de calor (concreto, rocha de quartzo e ferro fundido) e diferentes tamanhos de partícula (0,02, 0,03 e 0,04 m). O coletor CPC avaliado neste estudo apresentou uma eficiência óptica de cerca de 63,6%. Verificou-se que o uso do óleo térmico como fluido de preenchimento (FF) resultou em maior eficiência térmica média (41,2%) em relação à água (31,7%) e ao ar (31,1%). A menor vazão mássica avaliada resultou na maior eficiência térmica média (41,2%). Em relação à análise do PBTES, o uso de materiais com menor condutividade térmica resultou em um aumento da diferença de temperatura entre o fluido de transferência de calor e o material sólido. A configuração multicamadas de materiais apresentou maior influência sobre os tempos de carga e descarga, assim como na energia térmica armazenada e liberada. O caso 9 apresentou o maior valor para Q_C (27,2 MJ) e para as eficiências de carga (87,5%), descarga (80,5%) e exergética (70,5%). Comprovou-se que o diâmetro de partículas variável e o tipo de material influencia na estratificação e transferência de calor no PBTES.

Palavras-chave: Sistema ambientalmente amigável. Coletor solar evacuado com tubo U. Energia renovável e sustentável. Energia solar. Sistema de armazenamento térmico de termoclina.

SUMMARY

GENERAL INTRODUCTION

Due to the intense industrial development, there is a constant increase in the world demand for energy in the most diverse forms, as energy plays a crucial role in the economic and social development of humanity. Over the years, global energy consumption has increased rapidly, predominantly supplied by fossil energy sources (Alptekin and Ezan, 2020; Sahin et al., 2020; REN21, 2022). However, the search for renewable and sustainable energy resources has intensified as an alternative to reduce environmental impacts and promote greater energy security (Azevedo et al., 2019; Khanlari et al., 2020). Among renewable sources, solar energy has received increasing attention due to its vast energy potential, abundant availability, inexhaustibility, and versatility (Hatami et al., 2020; Wu et al., 2020). In addition, Chen and Yang (2021) highlighted that solar thermal energy is the most abundant, affordable, and promising source to decarbonize residential and industrial heat demand.

Approximately 60% of the thermal energy used in the industrial sector is intended for process heat applications at temperatures up to 250 °C (Sharma et al., 2017; Barbosa et al., 2020). Although high-concentration solar collectors can reach these temperature ranges, their use is limited due to the high cost and complexity of the solar tracking system. On the other hand, compound parabolic collectors (CPCs), which are low concentration solar collectors, offer a more attractive, affordable, and popular alternative for these low and medium temperature applications. Furthermore, the heat generation cost per unit is considerably lower compared to collectors that require solar tracking (Kurhe et al., 2020). The use of evacuated glass tubes (ETs) in these collectors plays a key role, providing vacuum insulation and selective coating to reduce heat losses and improve absorption of solar radiation (Olfian et al., 2021).

Among the thermal energy transfer techniques, the use of a U-shaped tube inside the evacuated tube is widely applied due to its simple geometry, reduced manufacturing cost, practical applicability, and good efficiency (Naik et al., 2019). A key factor to improve the performance of these collectors is the heat transfer between the evacuated tube of the absorber and the U-tube, since the contact surface between them is very small. In recent decades, many researchers have sought to improve this transfer using different approaches (Essa et al., 2021; Olfian et al., 2021; Chen and Yang, 2022). The use of filling materials in the evacuated tube is a simple, viable and economical technique, as it does not require modification in the structure of the collector. However, there are still many gaps to be filled regarding the use of this technique.

The efficiency of technologies based on solar energy not only depends on the energy collection system but is also directly linked to the ability to store the collected energy for long periods, as well as convert it into a useful form of energy when needed (Gautam et al. Saini, 2020). In this scenario, thermal energy storage (TES) plays a crucial role in increasing the efficiency and reliability of solar systems, allowing the use of stored energy during periods of solar intermittency (Azaizia et al., 2020; Murali et al., 2020). Among the various structures considered for the thermal energy storage system, packed beds have stood out for their superior thermal performance compared to other types mentioned in the literature (Al-Alzawii et al., 2019; He et al., 2019).

The packed bed storage system (PBTES) consists of an insulated reservoir filled with a solid material to store thermal energy. In this system, a heat transfer fluid (HTF) is pumped into the reservoir, enabling heat transfer between the fluid and the solid material in charge and discharge cycles (Cárdenas and Garvey, 2019). During the charging process, HTF flows from the top to the bottom of the reservoir, heating the solid material as it passes through the packed bed. As a result, the fluid temperature gradually decreases along the bed, with the lowest temperature being observed at the bottom of the reservoir. On the other hand, during the heat discharge process, the flow direction is reversed, and the HTF is heated by the thermal energy stored in the solid material (Seyitini et al., 2023). The separation between the hot and cold zones is obtained due to buoyancy effects, through the formation of a temperature gradient, called thermocline (Palomba and Frazzica, 2022).

PBTES is considered a simple and efficient technology that can be used over a wide temperature range and incorporated into different thermal operations (Esence et al., 2017; Cárdenas and Garvey, 2019). The use of a PBTES provides a higher storage density and a smaller volume, which can reduce its cost by up to 37% compared to the conventional two-tank system (Chang et al., 2020). In these systems, different solid materials can be used to store energy in the form of sensible heat, such as rocks, metals, sand and ceramics. Among the factors that influence the performance of the PBTES, the type of HTF used, the size and type of the particle, the operating temperature and the flow rate can be mentioned (Gautam and Saini, 2020).

The complexity and transient nature of the systems discussed, along with their integration, make it difficult to conduct experiments, which are costly and consume a significant amount of time. Computational fluid dynamics (CFD) is a highly versatile tool that has been used in the study of several complex processes (Prommuak et al., 2020). This approach allows

an in-depth understanding of the phenomena involved in the analyzed processes and for some processes it offers the possibility of optimizing the systems even before their construction (Prakash et al., 2016). The CFD technique offers the advantage of saving costs and time during experimentation, while overcoming the limitations of analytical solutions (Jubaer et al., 2019). Furthermore, this tool plays a crucial role in simulating unusual operating conditions, such as high temperatures or hazardous environments, which would not be feasible in real experiments (Malekjani and Jafari, 2018). Thus, CFD emerges as a promising alternative for the investigation of phenomena related to different operations and work configurations.

Although the importance of using solar energy is proven, and the industrial demand for thermal energy is increasing daily, the lack of information, complexity and price of some technologies have limited the adoption of solar technologies on a large scale. Therefore, this study aimed to experimentally evaluate the thermal and economic performance of a CPC with a U-tube, using different filling fluids and mass flowrates. This study also sought to optimize a packed bed thermal storage system by numerically evaluating (CFD) the effect of different materials, particle diameters and configurations. In addition, an extensive review was carried out to provide parameters, address different types of dryers and emphasize the importance of thermal energy storage methods. The importance of computational numerical modeling to verify the phenomena of heat and mass transfer in drying systems and thermal energy storage was also presented.

REFERENCES

Al-Azawii, M.M.S., Theade, C., Bueno, P., Anderson, R. Experimental study of layered thermal energy storage in an air-alumina packed bed using axial pipe injections. **Applied Energy**, v.249, p.409-422, 2019.

Alptekin, E., Ezan, M.A. Performance investigations on a sensible heat thermal energy storage tank with a solar collector under variable climatic conditions. **Applied Thermal Engineering**, v.164, 114423, 2020.

Azaizia, Z., Kooli, S., Hamdi, I., Elkhal, W., Guizani, A.A. Experimental study of a new mixed mode solar greenhouse drying system with and without thermal energy storage for pepper. **Renewable Energy**, v.145, p.1972-1984, 2020.

Azevedo, S.G., Santos, M., Antón, J.R. Supply chain of renewable energy: A bibliometric review approach. **Biomass and Bioenergy**, v.126, p.70-83, 2019.

Barbosa, E.G., Araujo, M.E.V., Lopes, R.P., Martins, M.A., Moraes, M.J., Barbosa, E.G., Falconí, J.H.H. Exergetic, economic and environmental (3E) analysis of a low cost solar heater in different configurations. **Renewable Energy** v.160, p.1096–1104, 2020.

Cárdenas, B., Garvey, S.D. A load-based approach for optimizing a packed-bed thermal store. **Journal of Energy Storage**, v.25, 100835, 2019.

Chang, Z., Li, X., Falcoz, Q., Wang, Z., Neveu, P., Fasquelle, T. Approximate analytical characterization and multi-parametric optimization design of single-tank thermocline heat storage system. **Applied Thermal Engineering**, v.181, 116010, 2020.

Chen, X., Yang, X. Heat transfer enhancement for U-pipe evacuated tube solar absorber by high-emissivity coating on metal fin. **Journal of Building Engineering**, v.50, 104213, 2022.

Chen, X., Yang, X. Solar collector with asymmetric compound parabolic concentrator for winter energy harvesting and summer overheating reduction: Concept and prototype device. **Renewable Energy**, v.173, p.92-104, 2021.

Esence, T., Bruch, A., Molina, S., Stutz, S., Fourmigué, J-F. A review on experience feedback and numerical modeling of packed-bed thermal energy storage systems. **Solar Energy**, v.153, p.628-654, 2017.

Essa, M.A., Asal, M., Saleh, M.A., Shaltout, R.E. A comparative study of the performance of a novel helical direct flow U-Tube evacuated tube collector. **Renewable Energy**, v.163, p.2068-2080, 2021.

Gautam, A., Saini, R.P. A review on technical, applications and economic aspect of packed bed solar thermal energy storage system. **Journal of Energy Storage**, v.27, 101046, 2020.

Hatami, S., Payganeh, G., Mehrpanahi, A. Energy and exergy analysis of an indirect solar dryer based on a dynamic model. **Journal of Cleaner Production**, v.244, 118809, 2020.

He, Z., Wang, X., Du, X., Amjad, M., Yang, L., Xu, C. Experiments on comparative performance of water thermocline storage tank with and without encapsulated paraffin wax packed bed. **Applied Thermal Engineering**, v.147, p.188-197, 2019.

Jubaer, H., Afshar, S., Xiao, J. Chen, X.D., Selomulya, C., Woo, M.W. On the effect of turbulence models on CFD simulations of a counter-current spray drying process. **Chemical Engineering Research and Design**, v.141, p.592-607, 2019.

Khanlari, A., Güler, H.Ö., Tuncer, A.D., Şirin, C., Bilge, Y.C., Yılmaz, Y., Güngör, A. Experimental and numerical study of the effect of integrating plus-shaped perforated baffles to solar air collector in drying application. **Renewable Energy**, v.145, p.1677-1692.

Kurhe, N., Pathak, A., Deshpande, K., Jadkar, S. Compound parabolic solar collector – Performance evaluation as per standard test method and actual field conditions for industrial process heat application in Indian context. **Energy for Sustainable Development**, v.57, p.98-108, 2020.

Malekjani, N., Jafari, S.M. Simulation of food drying processes by Computational Fluid Dynamics (CFD); recent advances and approaches. **Trends in Food Science & Technology**, v.78, p.206-223, 2018.

Murali, S., Amulya, P.R., Alfiya, P.V., Delfiya, D.S.A., Samuel, M.P. Design and performance evaluation of solar - LPG hybrid dryer for drying of shrimps. **Renewable Energy**, v.147, p.2417-2428, 2020.

Naik, B.K., Bhowmik, M., Muthukumar, P. Experimental investigation and numerical modelling on the performance assessments of evacuated U – Tube solar collector systems. **Renewable Energy**, v.134, p.1344-1361, 2019.

Olfian, H., Ajarostaghi, S.S.M., Farhadi, M., Ramiar, A. Melting and solidification processes of phase change material in evacuated tube solar collector with U-shaped spirally corrugated tube. **Applied Thermal Engineering**, v.182, 116149, 2021.

Palomba, V., Frazzica, A. Application of numerical methods for the design of thermocline thermal energy storage: Literature review and critical analysis. **Journal of Energy Storage**, v.46, 103875, 2022.

Prakash, O.; Laguri, V.; Pandey, A.; Kumar, A.; Kumar, A. Review on various modelling techniques for the solar dryers. **Renewable and Sustainable Energy Reviews**, v.62, p.396-47, 2016.

Prommuak, C., Tharangkool, N., Pavasant, P., Ponpesh, P., Jarunglumlert, T. Computational fluid dynamic design of spent coffee ground cabinet dryer using recycled heat from air compressor. **Chemical Engineering Research and Design**, v.153, p.75-84, 2020.

REN21. **Renewables 2022 Global Status Report** (Paris: REN21 Secretariat). In Tech. Rep. p.1-311, 2022.

Sahin, A.Z., Uddin, M.A., Yilbas, B.S., Al-Sharafi, A. Performance enhancement of solar energy systems using nanofluids: An updated review. **Renewable Energy**, v.145, p.1126-1148, 2020.

Seyitini, L., Belgasim, B., Enweremadu, C.C. Solid state sensible heat storage technology for industrial applications – A review. **Journal of Energy Storage**, v.62, 106919, 2023.

Sharma, A.K., Sharma, C., Mullick, S.C., Kandpal, T.C. Solar industrial process heating: A review. **Renewable and Sustainable Energy Reviews**, v.78, p.124-137, 2017.

Wu, H., Liu, Q., Bai, Z., Xie, G., Zheng, J., Su, B. Thermodynamics analysis of a novel steam/air biomass gasification combined cooling, heating and power system with solar energy. **Applied Thermal Engineering**, v.164, 114494, 2020.

CHAPTER 1

THERMAL ENERGY STORAGE SYSTEMS APPLIED TO SOLAR DRYERS: CLASSIFICATION, PERFORMANCE, AND NUMERICAL MODELING: AN UPDATED REVIEW

Abstract: Drying is a complex process involving simultaneous heat and mass exchanges, and it is considered one of the oldest unit operations performed for preserving agricultural products. This process requires a significant amount of energy, and researchers have conducted different studies to improve energy efficiency, reduce drying time and preserve product quality. Dryers based on solar energy have gained more space, as this energy source is free and abundant. Thermal energy storage techniques can increase the reliability of solar energy for drying. These techniques allow the stored energy to be used in periods of no solar incidence. The complex processes involving each element of the solar drying process have made experiments quite expensive. Several studies have bet on the use of advanced techniques of computer simulation to minimize this problem. Studies have shown the effectiveness of using these techniques for different solar dryers, achieving satisfactory results. Therefore, this study aims to provide parameters, address different types of dryers, and emphasize the importance and methods of thermal energy storage. In addition, this study also addresses the use of computational numerical modeling to verify the phenomena of heat and mass transfer in drying systems and thermal energy storage.

Keywords: Clean resources. Computational and numerical simulations. Drying. Heat and mass transfer. Renewable energy. Sustainable energy. Turbulence.

Greek letters

ρ	–	Specific mass, kg m^{-3}.
β_t	–	Thermal expansion coefficient, K^{-1};
ΔH	–	Melting enthalpy, kJ kg^{-1};
$\Delta\tau$	–	Time interval, s;
ΔP	–	Pressure loss, Pa;
ΔT	–	Temperature variation, K;
ΔZ	–	Distance between points, m;
α, β, γ	–	Constants that depend on the product;
η	–	Efficiency;

Symbols list

$\overline{cpi}$	–	Average thermal capacity of flue gas, kJ mol^{-1} K^{-1};
$\dot{m}$	–	Mass flow rate, kg s^{-1};
$\dot{n}$	–	Molar flow rate of combustion product in the flue gas, mol s^{-1};
$\dot{Q}$	–	Flow rate, m^3 s^{-1};
$\dot{V}$	–	Volumetric flow, m^3 s^{-1};
$\dot{W}$	–	Energy consumed, W;
A	–	Collector aperture area, m^2;
C	–	Specific heat, J kg^{-1} K^{-1};
E	–	Total energy, kJ;
EQ	–	Energy, kWth;
g	–	Gravity acceleration, m s^{-2};
H	–	Total specific enthalpy, kJ kg^{-1};
h	–	Specific enthalpy, kJ kg^{-1};
HR	–	Distance between the cold and hot side of the reservoir, m;
I	–	Solar radiation incident on the aperture area, W m^{-2};
j	–	Points where temperature measurements;
L	–	Product Layer Height, m;
LHV	–	Lower calorific value, kJ m^{-3}, kJ kg^{-1};
LV	–	Latent heat of vaporization of water in the product, J kg^{-1};
LVW	–	Latent heat of vaporization of water, kJ kg^{-1};
M_f	–	Total mass, kg;
N	–	Number of points;
P	–	Power consumed, W;

r – Radius, m;
S – Reservoir cross-sectional area, m^{-2};
T – Temperature, K;
T^0 – Reference temperature of 273 K;
U' – Product water content, % b.s.;
v – Superficial velocity, m s^{-1};
V – Air flow, m^3 s^{-1} m^{-2};
w – Water content, %.

Subscripts

(t) – Instantaneous;
0 – Outlet;
aair – Ambient air;
bf – Burner feed;
Bio – Biomass dryer;
bt – Bottom of the reservoir;
ca – Air inlet into the combustion chamber;
cf – Circulating fluid;
ch – Drying chamber;
chloss – Loss from the chimney;
cm – Capsule material;
comb – Combustion process;
conv – Conversion;
cs – Capsule shell;
elec – Electrical;
et – Fluid at the inlet of the transport element;
evap – To evaporate water from the product;
ew – Evaporated water;
f – Fluid;
fa – Variation between the inlet and outlet of the heated fluid;
fan – Fan;
ff – Furnace feed;
FG – Flue gas;
Fi – Fluid inlet;
Fo – Fluid outlet;

Fsec – Drying fluid;

fuel – Fuel;

gas – Gas, gas dryer;

i – Inlet;

infuel – Generated by the combustion of fuel;

ini – Initial;

lpcm – PCM liquid phase;

PCM – Phase change material;

q – Gas burning;

rm – Raw material;

s – Superficial;

sdc – Supplied to the drying chamber;

sec – Overall drying;

Sol – Solar;

spcm – PCM solid phase;

st – Fluid at the outlet of the transport element;

Tc – Variation of thermocline levels;

tf – Transferred to the fluid;

tp – Top of the reservoir;

trans – Heat transport process;

tube – Inlet tube;

v – Volumetric.

1. INTRODUCTION

Drying is one of the oldest processing methods for preserving agricultural products. This process can prevent chemical reactions such as enzymatic and non-enzymatic browning and provides maximum retention of macronutrients (proteins, sugars, fibers), micronutrients (vitamins, minerals), and bioactive compounds (phenolic compounds, carotenoids, isoflavones) (Menon et al., 2020). In addition, dehydration contributes to reducing transport and storage costs and prolongs the shelf life of products. Despite the imminent benefits of reducing the water content of the products, some points, such as the high energy demand and long drying time, are obstacles to be overcome. Drying is an energy-intensive process, and its consumption can represent up to 20% of the total energy consumption of the industrial sector. It can correspond to up to 90% of the processing costs (Simo-Tagne et al., 2020). Researchers have made substantial efforts to investigate and implement more efficient technologies for the drying process. Phonetip et al. (2018) conducted a study to show the effect of intermittency on wood drying. According to the authors, intermittent drying can improve the quality of the final product and result in energy savings for the process. Berrocal et al. (2017) evaluated the effect of using different schedules during drying. In the study, the authors tested three different schedules to reduce drying time and energy consumption. Araujo et al. (2021) carried out a study of the infrared drying of pear slices. The authors point out that infrared drying is faster and more efficient than traditional methods using ovens. The authors also perform an energetic and exergetic analysis of the infrared dryer, showing that increasing the drying temperature significantly reduces the specific energy consumption and positively affects the energetic and exergetic efficiencies.

Due to the intense industrial development, there is a constant increase in the world's demand for energy in various forms. Fossil fuels are still responsible for supplying most of the energy demand of the world (REN21, 2019), including the thermal energy consumed for drying. However, the environmental impacts related to the use of these fuels and the gradual depletion of their reserves impose substantial limitations on their use. As a result of the current awareness of the environment and the development of sustainable energy policies, renewable energy sources assume a crucial role as alternatives for a more environmentally friendly and secure energy future (Achkari and El Fadar, 2020). As it has the most significant energy potential among renewable sources and is free, inexhaustible, widely available, and versatile, solar energy has attracted increasing attention. Undoubtedly, optimizing drying operations is essential from an economic and environmental point of view. However, many countries still

have a predominantly non-renewable energy matrix, and the search for dryers based on solar energy has gained prominence today. Bekkioui et al. (2020) highlighted that traditional dryers and kilns (based on fossil fuels) are still widely used, although harmful environmental effects are imminent. The advantages of solar dryers over traditional kilns and dryers go far beyond the environmental impact. The use of solar dryers can reduce overall drying costs by up to 80%, promotes obtaining a higher quality final product, eliminates greenhouse gas emissions, and is easy to implement and use (Jain et al., 2023). Although solar dryers have already proven their economic and environmental contribution, it is always worth conducting studies to optimize the collection, conversion, and use of available solar energy. Optimizing dryers based on solar energy ensures faster drying and allows more product to be dried with the same energy.

One of the main obstacles related to the use of solar energy is its temporal intermittence (Barbosa et al., 2019). Therefore, the efficiency of technologies based on solar energy depends on more than just the energy harvesting system. It is also closely related to storing the collected energy for considerable periods and converting it into the necessary applicable energy form. According to the main reports dealing with renewable energies (IEA, 2010; SunShot, 2012; Mehos et al., 2017) published in recent years, the primary efforts to consolidate concentrated collectors should focus on improving their capacity to supply the heat demand for days, weeks or seasons. Thus, thermal energy storage (TES) systems are at the forefront of the future development of the solar system. Researchers can achieve sustainable, more efficient, and economical applications in this scenario by designing solar thermal systems integrated with TES.

In the search for the optimization of solar drying systems, studies are constantly carried out to obtain a final quality product using the least amount of time and energy possible. Khouya (2020) carried out a study evaluating the effect of several parameters on the efficiency of a solar oven for drying wood. In the study, the authors evaluated the use of a heat exchanger and a latent heat storage unit on the thermal performance of the solar oven. The results of the study were auspicious. The authors verified that using an air heater to recover part of the energy released to the atmosphere (the heater uses the heat of the humid air to preheat the air that enters the thermal storage) could reduce the drying time by up to 62.4 %. In addition, they demonstrated that using the thermal storage system minimizes the drying time by up to 40%. The combination of these systems reduced energy consumption by up to 54%. Similar results were previously observed by Khoyua and Draoui (2019). In the study, the authors observed that

heat recovery and thermal storage systems could reduce drying time by up to 47 and 26.5%, respectively. The authors reached a maximum drying efficiency of 85% with these systems.

Despite the advantages of using dryers based on solar energy with thermal storage, the heat and mass transfer mechanisms of these systems and the flow regime are very complex. For this reason, in addition to experimental studies, the computational fluid dynamics (CFD) method has been used in several research studies to design and evaluate different types of drying systems (Guler et al., 2020). For complex processes with significant constraints, CFD can be beneficial. The CFD framework typically provides opportunities to investigate various phenomena and their combined implications from a generic perspective. Computational numerical simulation is one of the primary analysis methodologies used to predict variations in heat, mass transfer, and fluid flow in drying systems (Motahayyer et al., 2019). Although using the CFD technique only partially replaces physical experiments, it can significantly reduce the cost and time required for experimental work.

Due to the importance of the topic, different studies have been carried out over the years to gather information on advances in solar drying and thermal storage systems. Bal et al. (2010) systematically reviewed solar dryers with thermal energy storage systems for drying agricultural products. The authors focused on addressing the different forms of storage and their use in solar drying applications. In their study, Kant et al. (2016) contemplated similar objectives, adding a brief topic on using computational tools to optimize solar drying systems. Lingayat et al. (2020) recently reviewed indirect-type solar dryers for crops. The approach adopted by the authors included the different types of dryer configurations and the use of thermal energy storage materials for these systems. Although the literature shows studies focused on solar dryers and thermal energy storage, studies have yet to comprehensively contribute to applying them in conjunction with thermal storage, their performance, and their numerical modeling. Small and large-scale industries and farmers can adopt this application of renewable energy; therefore, this topic has a high potential for interest. This work helps to understand the drying process, the different types of dryers and their performance, the types of thermal energy storage systems, and the numerical modeling behind all these processes. In addition, it is worth pointing out that this work contributes to a topic badly discussed in research related to drying, the turbulence in porous media.

2. DRYING PROCESS

Interest in preserving and developing new and innovative products has increased the importance of the drying process as a processing method. The drying operation is widely used to preserve agricultural products, as reducing the water content to certain levels inhibits microbial growth and enzymatic modifications (Araujo et al., 2020). In addition, it provides less volume and mass for transport, requiring less space for storage. On the other hand, drying food products also promotes changes in color and texture, shrinkage, and losses of different nutritional bio compounds. These changes, especially losses of thermolabile bio compounds, are generally more significant as temperature and drying time increase (Vallespir et al., 2018).

Drying is a complex process that simultaneously involves heat and mass transfers, which are affected by the internal and external resistances of the product. During the drying of agricultural products, the internal mechanism of moisture transfer is mainly composed of capillary forces in the period of constant drying rate and diffusion in the period of decreasing drying rate (Yu et al., 2020). As for the external resistances, these are mainly dependent on the temperature, flow, and relative humidity of the drying medium. The detailed knowledge of the parameters of heat and mass transfer, diffusion, and drying behavior of the product is considered essential for the conceptualization, simulation, and optimization of this process. (Kouhila et al., 2020).

The high energy consumption can now be considered one of the most practical challenges for traditional drying techniques. One of the main objectives of the desorption process is to use a minimum amount of energy for maximum moisture removal for the desired final conditions of the product (Yogendrasasidhar and Setty, 2018). In most cases, this goal is far from reality. In this sense, developing and employing economically efficient drying techniques that reduce time and energy consumption and maintain product quality is crucial. Implementing renewable energy in drying technologies is considered a fundamental approach since renewable energy is becoming an essential alternative for replenishing and diversifying the world's energy matrix.

2.1. The energy efficiency of the drying process

There is a great debate among the scientific community regarding using an appropriate method to calculate the energy efficiency of drying systems. The energy efficiency of the drying process, often adopted, is related to the energy used for the evaporation of the water contained

in the product. The basic approach to evaluating energy efficiency is calculating the ratio between the energy used or required for a given process and the amount of energy supplied or made available. Figure 1 shows a typical schematic of a dryer. M, EQ, T, Y, Fs, X, and Eh, represent airflow (kg s^{-1}), associated energy (kJ h^{-1}), temperature (°C), absolute air humidity (kg H_2O kg dry air^{-1}), feed rate (kg h^{-1}), the water content of the product (kg H_2O kg dry $matter^{-1}$) and the energy supplied to the drying process (kJ h^{-1}), respectively. The drying process can be divided into three stages: heat generation, heat transport, and drying. The energy efficiency of each of these steps can be defined separately. Optimizing any of the steps consequently increases the overall energy efficiency of the process.

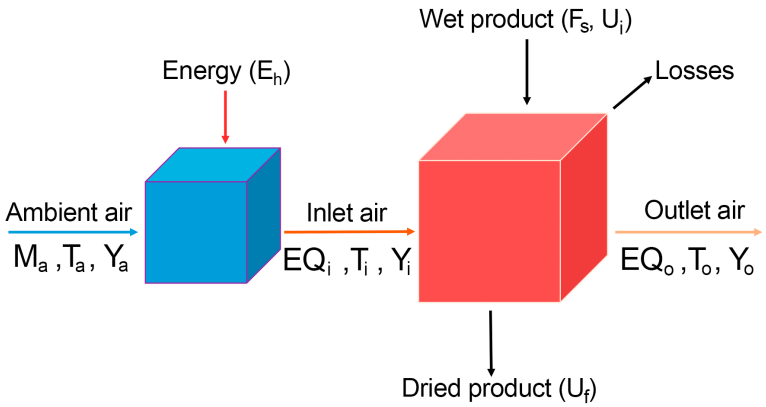

Fig. 1. Typical layout of a dryer.

2.1.1. Thermal energy generation

The most used sources for the generation of thermal energy from the drying process of agricultural products are biomass, natural gas/biogas/LPG, and solar energy. The determination of the efficiency of this generation can be carried out in different ways and depends primarily on the source used. In addition to the sources cited separately, many studies focus on using two or more sources to construct and evaluate hybrid dryers (Zoukit et al., 2019; Ananno et al., 2020; Ndukwu et al., 2020). In general, hybrid dryers combine solar energy with some other source of thermal energy. The objective of these dryers is to reduce the cost and drying time, allowing the continuous drying of the product even in the absence of solar energy.

Different authors present different methodologies to quantify the efficiency of biomass conversion in generating thermal energy. Carvalho et al. (2018) proposed a method to determine energy losses associated exclusively with the latent and sensible heat of the flue gases that leave the furnace chimney. In this methodology, the authors evaluated the velocity, temperature, and composition of the flue gases at intervals of 20 seconds, and the combustion efficiency was

determined using Eqs (1) to (3). Lee et al. (2018) evaluated the efficiency of the same process using a different methodology. The authors assessed efficiency as the ratio between the energy gained by the fluid and the total energy supplied by the raw material (Eqs (4) to (6)).

$$\eta_{conv} = \frac{E\dot{Q}_{in} - E\dot{Q}_{chloss}}{E\dot{Q}_{in}} \quad (1)$$

$$E\dot{Q}_{in} = \dot{m}_{ff}\, LHV_{fuel} + \dot{m}_{ca}\, h_{aair} \quad (2)$$

$$E\dot{Q}_{chloss} = \sum_{i=1}^{i=n} \dot{n}_i\, \overline{cpi}\, (T_{FG} - T^0) + \dot{m}_{ff}\, w_{fuel}\, LVW \quad (3)$$

$$\eta_{conv} = \frac{EQ_o}{EQ_i} \quad (4)$$

$$EQ_i = \dot{m}_{ff}\, LHV_{fuel} \quad (5)$$

$$EQ_o = \dot{m}_{ca}\, C_f\, (T_{Fo} - T_{Fi}) \quad (6)$$

In the heat generation strategy using natural gas, biogas, or LPG (Liquefied Petroleum Gas), burner efficiency represents the energy absorbed by the fluid and the total energy supplied by the gas (Eq. 7) (Karki et al., 2019). Using a semi-confined combustion flame in this generation can significantly increase thermal efficiency (Kuntikana and Prabhu, 2019). Many conventional burners typically rely on an open combustion flame (or free flame). A large amount of energy can be lost through the flue gases, leading to relatively low thermal efficiency.

$$\eta_{conv} = \frac{\dot{m}_{ca}\, C_{cf}\, \Delta T_{fa}}{\dot{Q}_{bf}\, LHV_{gas}} \quad (7)$$

Heat generation from solar energy is undoubtedly one of the most promising and researched today. The solar collector converts the energy absorbed from the solar radiation into useful thermal energy. The conversion efficiency varies significantly with the intensity of solar radiation, ambient temperature, the inlet temperature of the working fluid, and the use or not of forced convection. The efficiency of converting solar energy into heat can be calculated

according to Eq. (8), which considers the energy absorbed by the fluid and the energy available in the collector area (Barbosa et al., 2020b).

$$\eta_{conv} = \frac{\dot{m}_{fa}\, C_{fa}\, (T_{Fo} - T_{Fi})}{A\, I} \tag{8}$$

2.1.2. Heat transport

The heat generated from any source can be used immediately in integrated dryers or transported to the dryer for the drying process. Thermal losses that occur in different elements during heat transport cause a reduction in the overall efficiency of the process. Thus, using short, well-insulated features to minimize thermo-hydraulic losses is preferable. Heat transport efficiency can be obtained by performing energy and mass balances (Eq. 9). This equation is a relationship between energy leaving and energy entering the transport element (Araujo et al., 2021).

$$\eta_{trans} = \frac{\dot{m}_{st}\, T_{st}}{\dot{m}_{et}\, T_{et}} \tag{9}$$

2.1.3. Drying

Drying is one of the industrial processes with the highest thermal energy consumption. This process focuses on several studies to improve efficiency in different types of dryers. The overall drying efficiency estimates how much of the energy supplied by the dryer is used to remove water from the product. Then, the drying efficiency can be calculated according to Eq. (10) (Araujo et al., 2021). During drying, all the energy transferred is not necessarily consumed to reduce the water content of the product. One of the primary energy losses in the drying chamber is the energy loss associated with the exhaust air. This energy can be recovered to some extent if it is recirculated in the drying chamber. The recovery of part of this energy is possible through recirculation in the drying chamber. Studying these discrepancies and optimizing operational and design parameters are the main objective of energy analysis in this type of process.

$$\eta_{sec} = \frac{E_{evap}}{E_{sdc}} \tag{10}$$

In forced convection direct-type solar dryers, the overall efficiency, including the energy consumed by the fans, can be estimated according to Eq. (11). The dryer efficiency is calculated according to Eq. (12) whether natural convection governs airflow (Altobelli et al., 2014). As they are related to direct-type dryers, these equations consider the total energy supplied by the sun in the collector opening area. In indirect solar dryer systems, drying efficiency is determined considering the thermal energy delivered to the dryer, that is, the energy readily available in the drying chamber, according to Eq. (13) (Goud et al., 2019; Lingayat et al., 2020).

$$\eta_{Sol} = \frac{\dot{m}_{ew}\, LV}{A\, I + P_{fan}} \tag{11}$$

$$\eta_{Sol} = \frac{\dot{m}_{ew}\, LV}{A\, I} \tag{12}$$

$$\eta_{Sol} = \frac{\dot{m}_{ew} LV}{\dot{m}_{fa}\, C_{fa}\, T_{Fsec} + P_{fan}} \tag{13}$$

In drying, where biomass is used as a source for heat generation, it is easy to deduce that the drying efficiency is given by the ratio between the energy used for drying and the energy provided by the combustion process, as can be seen in Eq. (14) (Okoroigwe et al., 2015). The same concept can apply to drying using gas burners, replacing the energy source, resulting in Eq. (15) (Zoukit et al., 2019; Murali et al., 2020).

$$\eta_{Bio} = \frac{\dot{m}_{ew}\, LV}{\dot{m}_{ff}\, LHV_{fuel}\, \eta_{comb} + P_{fan}} \tag{14}$$

$$\eta_{Gás} = \frac{\dot{m}_{ew}\, LV}{\dot{Q}_{gas}\, LHV_{gas}\, \eta_q + P_{fan}} \tag{15}$$

2.2. State of the art of dryers

Solar energy and biomass are currently some of the main thermal energy sources used in drying agricultural products due to the low cost of generating heat. However, in regions where prices are competitive, other sources such as natural gas, biogas, and LPG are used to

dry products. The share corresponding to solar energy is constantly growing, but some obstacles have limited its dissemination, such as the economic viability and reliability of dryers. The variety of solar dryers of different types and sizes can make it difficult for users to choose the right one. Therefore, it is crucial to collect all details of solar dryers of different types so that their usefulness for other applications can be considered (Lingayat et al., 2020).

Different authors have conducted several studies on the efficiency of biomass dryers over the years. A characteristic generally observed in these dryers is low efficiency. Chavan et al. (2008) evaluated the performance of a biomass dryer (eucalyptus wood) for drying fish and observed that the average drying efficiency was only 4.90%. Okoroigwe et al. (2015) evaluated the efficiency of a potato dryer powered by charcoal and obtained an average efficiency of less than 3.34%. Aiming to increase the efficiency of a biomass-powered dryer, Tippayawong et al. (2008) studied the importance of exhaust air recirculation. The authors found that much of the exhaust air still had drying potential, and the recirculation of this air increased drying efficiency from 29 to 35%.

Using gas/biogas/LPG to generate heat for drying can improve the process because the conversion is highly efficient in some burners. Zoukit et al. (2019) obtained an average drying efficiency of approximately 35% by maintaining the chamber temperature at about 71 °C for drying tomato slices. López-Vidaña et al. (2013) evaluated the performance of a hybrid solar-gas dryer for the dehydration of tomato slices. The dryer efficiency varied between 86 and 7%. This difference occurs because a large amount of free water evaporates easily at the beginning of drying. As the drying process progresses, removing water from the product becomes more complex, and part of the heat supplied is not efficiently used.

Solar drying is one of the most studied, as the search for renewable sources for thermal energy generation is highly relevant. Despite the benefits of using solar energy for drying agricultural products, the low drying capacity compared to conventional dryers limits the development of solar dryers (Motahayyer et al., 2019). This situation can be alleviated with TES, allowing drying in times of no sunlight. Altobelli et al. (2014) evaluated a direct solar dryer with forced air convection and achieved instantaneous efficiencies between 7 and 70%. The authors performed to evaporate water in open trays. The observed variations are attributed to temporal intermittence, as thermal energy collection becomes more efficient at times close to noon and declines at other times. Daghigh et al. (2020) investigated the efficiency of a solar dryer coupled to an evacuated tube collector for drying tarkhineh (a soup based on wheat and yogurt in mountainous regions) and found an average efficiency of 28.2%.

Table 1 presents a summary of research that evaluated the drying efficiency of different types of dryers over the years. Biomass dryers and direct-type solar dryers are the least efficient. Indirect solar and gas dryers provide a reasonable average efficiency, considering that the variation in efficiency observed during the drying process is unavoidable. As noted, the efficiency of hybrid dryers is highly dependent on the secondary source associated with solar energy. The use of solar energy thermal storage systems can guarantee to dry in periods of no solar incidence and eliminate the need for an auxiliary energy source, resulting in reduced drying costs.

Table 1. Summary of average efficiencies of various types of dryers used over the years

Reference	Dryer type	Product	Average efficiency
Prasad e Vijay, 2005	Biomass	Turmeric, Ginger, Guduchi	3.4 – 7.1%
Madhlopa e Ngwalo, 2007	Biomass	Pineapple slices	11.0 – 15.0%
Amer et al., 2010	Solar-electric hybrid	Banana	65.0%
López-Vidaña et al., 2013	Gas	Tomato slices	46.8%
Condorí et al., 2017	Indirect solar	Onion	30.0 – 35.0%
Fudholi et al., 2014	Indirect solar	Red seaweed	27.0%
Kareem et al., 2017	Indirect solar	Roselle	36.2%
Chaouch et al., 2018	Direct solar	Camel meat	7.8 – 10.4%
Wang et al., 2018	Indirect solar	Mango slices	33.8%
Yahya et al., 2018	Biomass-solar hybrid	Rice	15.4%
Atalay, 2019	Indirect solar	Orange	34.4%
Bhardwaj et al., 2019	Indirect solar	Medicinal plants	26.1%
Goud et al., 2019	Indirect solar	Okra	26.1%
Zoukit et al., 2019	Gas	Tomato slices	35.0%
	Gas-solar hybrid		37.0%
Iranmanesh et al., 2020	Indirect solar	Apple	33.0 – 39.0%
Murali et al., 2020	Gas-solar hybrid	Shrimp	36.7%
Hadibi et al., 2021	Solar-electric hybrid	Garlic cloves	79.7%
Singh et al., 2021	Indirect solar	Fenugreek leaves, turmeric	23.6 – 34.1%
Sözen et al., 2021	Indirect solar	Onion	56.3 – 71.3%
Simo-Tagne, et al., 2022	Indirect solar	Cocoa bean	5.0 – 18.0%

3. SOLAR ENERGY

In general, solar energy can be grouped into two categories: photovoltaic solar energy and solar thermal energy. Photovoltaic energy is a sustainable solution for directly converting sunlight into electrical energy. Photovoltaic cells use the photoelectric effect of semiconductor materials. This principle establishes that, under certain conditions, an electron present in a material can absorb the energy associated with a photon. By absorbing this energy, the electron can leave the valence band and be elevated to the conduction band, contributing to generating an electric current (Hernández-Callejo et al., 2019). However, photovoltaic cells still have low efficiencies (15 to 25%). A significant range of the solar spectrum is not used in this conversion and dissipates heat during their operation (Riahi et al., 2020).

Thermal solar energy aims to convert solar radiation into heat. This conversion is based on well-known heat transfer phenomena (radiation, conduction, and convection) (Kreith, 1976). Thermal solar collectors are devices that absorb solar radiation and convert it into useful thermal energy at different temperature levels. These collectors can be classified based on the concentration rate into concentrated and non-concentrated solar collectors (Alam et al., 2021). The main characteristic of a non-concentrated collector is that the area of interception and absorption of solar radiation is the same, leading to low use of available energy. Thus, this type of collector is used for low-temperature applications such as home heating.

Concentrating collectors use mirrors to focus solar radiation onto a central receiver, which absorbs solar energy and converts it into heat through a heat transfer fluid (HTF). The increased operating temperature and heat collected per unit area provide greater thermal efficiency. In contrast, the smaller absorption surface area significantly decreases heat losses from the system (Cabeza et al., 2017). Four main concentrator collectors are available: central receiver concentrator, parabolic dish collector, linear Fresnel collector, and parabolic trough collector (PTC). These collectors are classified according to their design (geometry), the configuration of mirrors and receivers, the type of HTF used, and whether they have thermal storage.

PTC is one of the most widespread technologies among concentrated solar energy systems. It presents advantages such as high efficiency and power density, durability, versatility, and possible integration with TES systems (Barbosa et al., 2020a). Several factors and components have been extensively researched and reported in the literature aimed at improving this energy collection system (PTC), such as the improvement of the receiver tube (Bellos et al., 2018; Norouzi et al., 2020), the use of nanofluids (Bozorg et al., 2020), the

geometry and structure of the collector (Biencinto et al., 2019; Winkelmann et al., 2020), among others. Such efforts made possible the development of increasingly efficient and consolidated PTCs. However, the efficiency of solar energy systems depends not only on the energy harvesting element but also on its storage capacity to reduce the impacts of the temporal intermittence of solar energy.

4. THERMAL STORAGE SYSTEMS

The TES system plays a crucial role in increasing the efficiency and reliability of solar energy systems, as it allows for storing energy during intermittency periods. This can balance energy supply and demand at different times and applications (Achkari and El Fadar, 2020). The TES are classified according to the form of thermal energy storage and the technique used. Choosing the best storage system primarily depends on your specific application.

4.1. Classification according to the form of heat storage

There are three ways to store thermal energy in TES: sensible, thermochemical, or latent heat. In sensible heat storage systems, thermal energy is stored by increasing the temperature of the material (usually liquid or solid). This type of storage is considered a mature technology, already implemented in different applications and commercially available (Yang and Cai, 2019). The sensible heat storage in each material mainly depends on its heat capacity (ρc_p), related to the stored energy density. It also depends on its thermal diffusivity ($k/\rho c_p$), which determines the rate at which stored energy can be released and extracted. The amount of energy stored is the product of the mass of the stored material, its specific heat, and the temperature variation that occurs during the process. The main advantages of a sensible heat storage system are low cost and ease of operation, while its main disadvantage is low storage capacity (Kalaiarasi et al., 2020). Water, thermal oil, concrete, and rocks are the most used materials in these systems.

In latent heat storage, thermal energy is stored through phase change processes at a constant temperature. The enthalpy of fusion, vaporization, or sublimation is stored when a given material changes its phase from solid to liquid, liquid to gas, or solid to gas, respectively (Mehari et al., 2020). The change from the solid to the liquid phase is preferable in these systems mainly due to their low volumetric expansion. In addition, a wide melting temperature range can be obtained from different phase change materials (PCM), making this type of storage

suitable under various operating conditions. The latent heat storage capacity is not only governed by the specific heat of the material but also by the enthalpy of phase change. This technology is a more efficient and cost-effective alternative when compared to sensible heat storage systems. Its main advantages are high stored energy density (five to fourteen times higher than sensible storage), low cost, and stable outlet temperature (Faraj et al., 2020). However, most PCMs have low thermal conductivity, leading to slow charging and discharging rates. The main PCMs used in this type of storage are paraffin, hydrated salts, and fatty acids.

In thermochemical storage, thermal energy is stored based on reversible, non-isothermal chemical reactions of the medium, in which molecular bonds are repeatedly broken and rearranged (Romaní et al., 2019). In general, thermochemical energy storage consists of a charging step in the endothermic reactor and a discharging step in the exothermic reactor (Yan et al., 2020). Metal hydrides and ammonia are examples of materials used in this type of conversion. Its main advantages are operational flexibility, long storage life, and high energy density. According to Wu et al. (2018), this density can be, on average, fifteen times higher than sensitive storage and six times higher than latent storage. However, the development of this technology is still incipiently compared to other storage forms. In this type of storage system, technological coupling and heat and mass transfer are still so complex that they affect their operation and design, making their development only at the laboratory scale phase (Feng et al., 2020). Due to its favorable characteristics, this type of storage has been the focus of numerous recent research studies. Still, much remains to be done to achieve commercial viability.

4.2. Classification according to the technique used

The TES can be classified as active or passive based on the technique used to store energy. Active systems can be subdivided into direct and indirect. In a direct active system, the HTF also acts as the storage medium, while in the indirect system, the HTF and the storage medium are different. In the passive system, the storage medium (usually solid) is kept immobile in the reservoir and is heated or cooled by the circulation of the HTF (Pelay et al., 2017). Usually, in the passive system, storage is carried out by dual means; the HTF passes through the storage only to load or unload a solid material. The HTF transports the collected energy to the storage medium during charging and receives energy from the medium during discharging (Kumar et al., 2019).

The main active systems are two-tank and single-tank systems (thermocline). The first two tanks are used, one for storing the hot fluid (charge) and the other for the cold fluid (discharge). The advantages of this system are the ease of operation and control and the possibility of raising the operating temperature and consequently increasing efficiency. Its primary disadvantage is the high cost (Wan et al., 2020). The hot and cold fluid portions are stored in the same tank in the single-tank system. A thermal gradient ideally stabilized and preserved by buoyancy effects, called a thermocline, develops within the system. An ideal thermocline has an imaginary layer of perfect thermal insulation, vertically movable, protecting the fluid mixture. However, it is difficult to perfectly separate hot and cold fluids (Baba et al., 2020). The main advantage of this system is its low cost, while the disadvantage is the need for greater control during the charge and discharge process to maintain thermal stratification.

The packed bed storage system is most used in passive storage systems. Most packed bed systems are single tank systems that act as a thermocline (Yang and Cai, 2019). This system consists of an insulated reservoir filled with a solid material to store thermal energy. An HTF is pumped to the reservoir, where heat transfers between the fluid and the stored solid in charge and discharge cycles. During the charging process, the HTF flows from the top of the reservoir to the bottom, heating the solid material. On the other hand, during the heat discharge process, the flow direction is reversed, and the HTF is heated by the thermal energy stored in the solid material (Baba et al., 2020). To increase the energy density stored in these systems, encapsulated PCMs as a storage medium has been increasingly investigated. However, the additional cost and stability of the PCM package still need to be overcome.

4.3. State of the art of TES system applied to solar dryers: a historical approach

Over the years, numerous researchers have bet on using TES systems to improve the efficiency and reliability of solar systems and overcome their main obstacle, temporal intermittence. It is estimated that these researches started in the 60s for space applications. Since then, this technology has experienced significant advances, and new forms and storage materials have been investigated, seeking to reach ever higher levels of development in various applications. The use of thermal storage systems has also been reported in solar dryers. Garg et al. (1985) experimentally evaluated a solar air collector integrated into a rock heat storage system for agricultural use. The authors highlighted that the ideal thickness of the bedrock depends mainly on the amount of incident solar radiation. A grain drying system integrated with rock heat storage was investigated by Tiwari et al. (1994) on wheat drying. The rock heat

storage considerably reduced the drying temperature fluctuation. Until then, the studies on solar dryers integrated into thermal storage systems were restricted to sensible heat storage (Maroulis and Saravacos, 1986; Chauhan et al., 1996; Ayensu, 1997; Aboul-Enein et al., 2000; Jain, 2005). It is also worth mentioning that in such studies, the storage medium is usually allocated in the drying chamber or the energy collection system. Therefore, using a thermal reservoir solely for heat storage is rare for this application.

In 2006, Devahastin and Pitaksuriyarat evaluated using a latent heat storage system to reduce the extra energy required for solar drying and its effect on sweet potato drying kinetics. The storage system consisted of a cylindrical reservoir filled with paraffin. A finned copper tube in a "U" shape inside the reservoir was a heat exchanger between the drying air and the paraffin. The storage system contributed to an increase in initial and operational costs. However, it saved around 40% of the additional energy required during drying. In recent years many studies have been carried out for storage systems integrated with solar dryers. In most recent studies, the same configuration of the TES is still observed. Most research still focuses on storing latent heat in the drying chamber (Jain and Tewari, 2015; Bhardwaj et al., 2019; Azaizia et al., 2020; Yadav and Chandramohan, 2020) or on the waste energy collection system (El khadraoui et al., 2017; Abubakar et al., 2018; Vásquez et al., 2019; Arun et al., 2020). Figure 2 shows a schematic of solar dryers with thermal storage (A) in the drying chamber and (B) in the energy collection system. This can limit the amount of energy stored and consequently impact your efficiency. In these systems, the most used PCM is paraffin due to its low melting temperature, wide availability, and low cost.

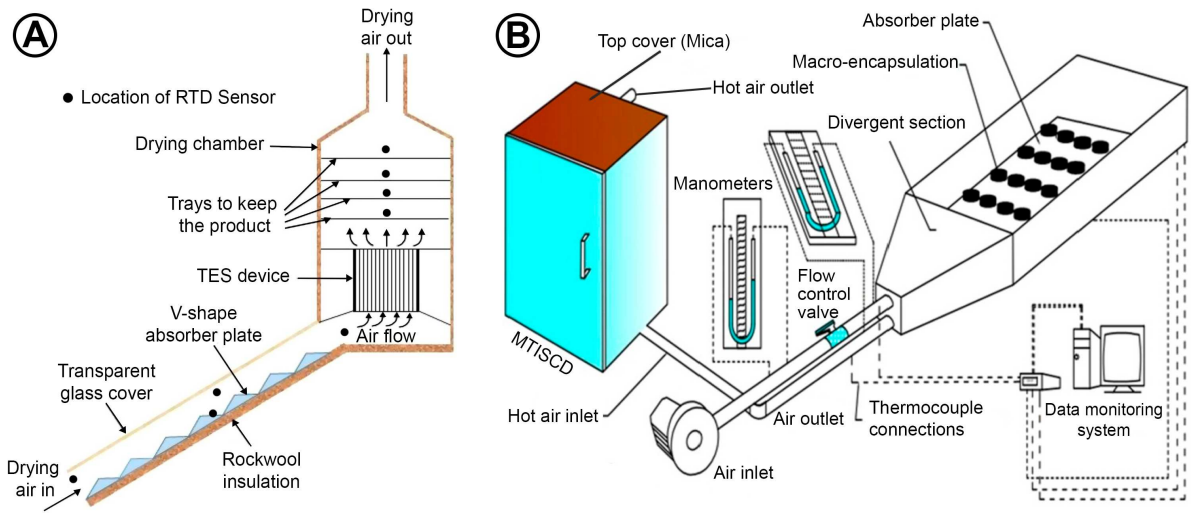

Fig. 2. Schematic of solar dryers with thermal storage (A) in the drying chamber (Yadav and Chandramohan, 2020) and (B) in the energy collection system (Arun et al., 2020).

Lakshmi et al. (2018) evaluated a mixed-mode solar dryer integrated with latent heat storage to dry black turmeric (Fig. 3). The storage system was a shell-and-tube heat exchanger. The HTF and PCM used were air and paraffin, respectively. The drying time was reduced by about 60.7% compared to the most used drying method (sun drying). Atalay (2020) performed the energy and economic analysis of two energy storage systems for drying. The thermal storage evaluated was a packed bed system with pebble stones (PBTES) and a PCM system with paraffin (PCM). The average efficiencies were close, 68.2% for PBTES and 68.5% for PCM. However, PBTES had an initial cost of about 10.5% lower than PCM. Iranmanesh et al. (2020) performed a numerical and experimental analysis of a solar tray dryer equipped with an evacuated tube solar collector and latent heat thermal storage. In the study, the working fluid was water, and the PCM was paraffin. The dryer was evaluated with and without PCM in drying apple slices. Using PCM reduced drying time by up to 10.2% and increased the thermal energy entering the dryer. A summary of the most recent research on TES-integrated solar dryers and their main findings are presented in Table 2.

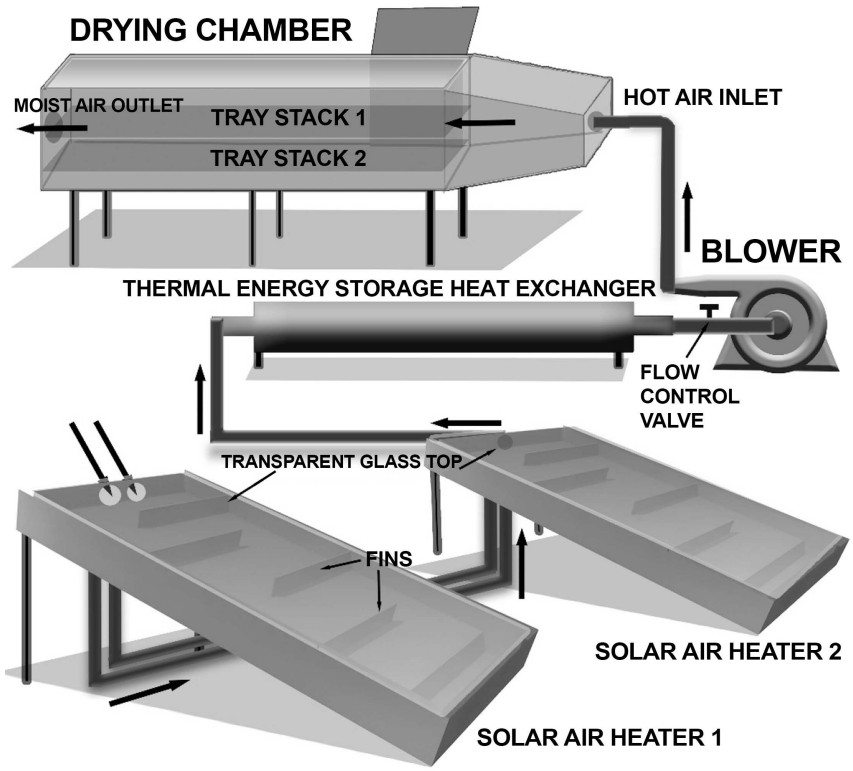

Fig. 3. Mixed-mode forced convection solar dryer with thermal energy storage system (Lakshmi et al., 2018).

Table 2. Recent research and its main findings

Reference	Approach	TES configuration	TES type and storage material	Main results
Álvarez-Sánchez, et al., 2021	Numerical and experimental	TES in a single reservoir	Sensible heat storage (water)	The direct-indirect hybrid solar air heating system showed an annual performance increase of 58% of the useful annual energy compared to the direct mode and 42% of the annual solar fraction compared to the indirect way.
Bhardwaj et al., 2021	Experimental	Storage medium located on the absorber plate and drying chamber	Sensible (thermal oil) and latent (paraffin) heat storage	The average efficiency values of the dryer without and with TES were 9.8 and 26.10% (energetic) and 0.14 and 0.81% (exergetic), while the drying rate was 0.028 and 0.051 kg h^{-1}, respectively.
Lakshmi et al., 2021	Experimental	TES in a single reservoir	Latent heat storage (paraffin)	The overall efficiency of the dryer in mixed mode is 20% higher than indirect solar. The energy efficiency of the TES varied between 56.40 and 60.2% on the evaluated days.
Madhankumar et al., 2021	Experimental	TES in a single reservoir. The insertion of fins in the TES was evaluated.	Latent heat storage (paraffin)	The total energy efficiencies of the dryer in the summer were 17.76, 18.97, and 19.41% for the case without TES, with TES, and with TES + fins, respectively. The CO_2 emission and mitigation of the dryer integrated with TES + fins were 23.88 kg $year^{-1}$ and 20.13 tons.
Andharia et al., 2022	Numerical and experimental	Storage medium located on the absorber plate	Sensitive (black pebbles) and latent (paraffin) heat storage	The integrated paraffin dryer reduced the raw material moisture from an initial value of 84.65% (wb) to 4.50% (wb) in 9 h. The integrated pebble-stone solar dryer and the solar dryer without storage took 11 and 12 hours to dry the raw material to a comparable state.

Chaatouf et al., 2022	Numerical	Packed-bed type TES located in the plenum chamber	Sensible heat storage (gravel, granite, and sandstones)	The thermal efficiency of the solar dryer increased by about 2.47% overnight compared to the case without storage. Among the different materials evaluated, the granite stones presented the best performance.
Gilago et al., 2022	Experimental	TES located in the plenum chamber (bottom of the drying chamber)	Latent heat storage (paraffin)	The mean collection and drying efficiencies of the system were 62.56% and 61.87% (without and with TES) and 6.62% and 13.13% (without and with TES), respectively. The specific energy consumptions were 1.54 and 0.25 kWh kg^{-1} for without and with TES, respectively.
Jahromi et al., 2022	Experimental	TES in a single reservoir with a PCM inside a spiral copper tube.	Armazen Latent heat storage (paraffin)	Thermal efficiency increased by about 1.51–7.81% compared to the system without PCM. Furthermore, PCM increased exergetic efficiency and ranged from 35.30 to 59.70%.

A summary of results from solar dryers involving PCM is presented in Table 3. Data on energy consumed per kilogram of dry product and efficiencies are presented. Numerous factors can influence the efficiency of the drying process and the efficiency of the system as a whole. Then, adopting a single configuration as the best is not feasible. These factors refer to where the system will be applied and for what purpose.

Table 3. Summary of results obtained in studies of solar dryers integrated with latent heat storage

Reference	PCM	Energy consumption	Drying Efficiency	System Efficiency
Lakshmi et al., 2018	Paraffin	18.76 MJ kg^{-1}	12.10%	-
Atalay, 2020	Paraffin	3.95 MJ kg^{-1}	-	68.55%
Bhardwaj et al., 2021	Paraffin	40.78 MJ kg^{-1}	30.28%	10.53%
Lakshmi et al., 2021	Paraffin	9.72 MJ kg^{-1}	-	47.80%
Madhankumar et al., 2021	Paraffin	-	-	18.57%
Andharia et al., 2022	Paraffin	13.10 MJ kg^{-1}	-	10.61%
Gilago et al., 2022	Paraffin	0.91 MJ kg^{-1}	-	13.13%
Jahromi et al., 2022	Paraffin	1.92 MJ kg^{-1}	47.50%	34.83%

5. COMPUTATIONAL MODELING

Numerical modeling is an effective alternative to experimental approaches to develop new procedures or optimize existing processes at a relatively low cost. Among several numerical models, computational fluid dynamics (CFD) is a highly versatile tool that can study various techniques (Prommuak et al., 2020). The CFD method solves the governing equations, including a series of nonlinear differential equations coupled to describe the conservation laws, discretizing them into a set of algebraic equations. According to Jubaer et al. (2019), this method has been used with the same frequency as traditional didactic methods of carrying out experiments and mathematical modeling, in solving problems involving the flow of fluids, both in the industrial and academic areas.

The adoption of numerical approaches has become increasingly common to investigate the characteristics of heat, mass, and momentum transfer in various complex processes. The CFD technique offers the advantage of saving cost and time during experimentation while simultaneously overcoming the limitations of analytical solutions (Jubaer et al., 2019).

Furthermore, its use allows for obtaining detailed information regarding flow patterns, temperature distribution, and concentration, which can hardly be achieved in experimental observations. This tool can also be necessary for simulating unusual operating conditions with high temperatures or hazardous environments, which would not be possible in real experiments (Malekjani and Jafari, 2018). Due to its advantages, this technique has been extensively investigated in numerous applications.

Over the years, several authors have developed numerical models that satisfactorily represent experimental data. Validation of numerical models allows conditions different from those obtained experimentally to be further evaluated by simulations. The difference between the approaches is associated with several factors, such as thermal losses not quantified in the experimental model, variation of boundary conditions during the experiments, quality of the computational mesh used, correct choice of applied numerical methods, and definition of control conditions, among others. Table 4 presents the deviation data between the experimental and numerical data found by several authors. The software used for modeling is also provided. It is observed that the percentage errors vary between 1.67 and 14.95% for the studies presented.

Table 4. Mean percentage error (PE) observed between numerical modeling and experimental data for several studies

Reference	**Software**	**PE**
Tzempelikos et al., 2015	ANSYS-FLUENT	14.89%
Aktaş et al., 2017	ANSYS-FLUENT	10.93%
Cârlescu et al., 2017	ANSYS-FLUENT	7.00%
ElGamal et al., 2017	COMSOL	6.59%
Sanghi et al., 2018	ANSYS-FLUENT	14.95%
Chilka e Ranade 2018	ANSYS-FLUENT	14.34%
Ostanek e Ileleji, 2019	ANSYS-FLUENT	5.28%
Iranmanesh et al., 2020	ANSYS-FLUENT	4.80%
Afshari, et al., 2021	ANSYS-FLUENT	6.50%
Al-Kayiem and Gitan, 2021	ANSYS-FLUENT	9.10%
Moghimi et al., 2021	ANSYS-FLUENT	1.67%
Salvatierra-Rojas et al., 2021	ANSYS-FLUENT and MATLAB	3.13%
Zhang et al., 2022	ANSYS -FLUENT	2.59%

5.1. Drying process modeling

Accurate drying modeling is challenging due to its complex and multi-scale nature, various processes, and inherent high biological variability. According to Defraeye (2014), the multi-cube nature (multi^3: multiphase, multiphysics, and multiscale) of the drying process is responsible for its complexity and challenges when modeling them for the reluctance to undertake such an effort. This process is multiphase because several phases are present in the materials: solid phase (dry material matrix), liquid phase (free and adsorbed water), and gas phase (water vapor, dry air, among others). It is considered a multiphysics process because heat, mass, and momentum transport are coupled inside the material and exchange processes with the environment at the air-material (or material-material) interfaces. It is also multi-scale as the transport and exchange processes occur at various spatial scales.

Depending on its purpose, different numerical approaches can be used to model the drying process. Despite advances in developing smaller-scale models (Li et al., 2019; Chen et al., 2020), most drying process modeling research has been carried out at the dryer scale and macroscale (Chilka and Ranade, 2018; Babu et al., 2019; Benavides-Morán et al., 2020; Prommuak et al., 2020). This is due to the high level of knowledge required to model this process at smaller scales and the complexity experienced when coupling such results at larger scales. Macroscopic models assume the material as a continuum. Transport within the material is modeled by the actual material properties, which can be obtained experimentally or by numerical simulation. In this way, complex transport processes at the microscale level are concentrated in the material properties and transport equations (Defraeye, 2014).

The models can be formulated differently according to the approach used to describe the heat and mass exchange of the porous material with the environment during drying. The unconjugated approach only solves the energy and moisture transport equations within the solid (porous) domain. In these models, boundary conditions are imposed on the surface of the material to be dried. Advective transfer coefficients are commonly used to predict the heat and mass exchange of porous materials with the environment at the air-material interface. Such coefficients are usually calculated using semi-empirical correlations. Using these coefficients facilitates an essential part of modeling complex drying processes but, on the other hand, can compromise the accuracy of airside heat and mass transfer predictions (Khan and Straatman, 2016a).

In the conjugate approach, the heat and mass transport equations in air and porous material are solved simultaneously transiently. These models introduce mathematical

conditions to enforce the continuity of heat and mass transfer at the fluid-porous interface. This eliminates the requirement to define transfer coefficients between domain regions (Castro et al., 2018). Instead, transfer coefficients can be determined later, demonstrating their spatial and temporal variability (Ostanek and Ileleji, 2019). this modeling approach is inherently more accurate as airside transport at the interface is explicitly resolved. Thus, it may be necessary for some complex problems. However, the accuracy obtained does not always overcome the additional modeling effort and the computational cost employed (Defraeye, 2014).

5.1.1. Influence of the water content of the product on the pressure drop

Understanding air flow behavior through grains is critical to designing and optimizing drying and aeration systems (Yue and Zhang, 2017). A pressure drop is observed every time air flows through a porous medium (e.g., grain layer). It is necessary to use fans to overcome the pressure drop, whose energy demand depends on the magnitude of this pressure drop. An erroneous analysis of air velocity, bed type, water content, and product layer height in drying processes can result in excessive water loss and product quality degradation and cause significant pressure drops. The prediction of airflow resistance in a selected bed of agricultural material has been extensively studied over the years. Comprehensive studies on the effects of different factors such as airflow, bed type, product water content, bed depth, filling method, amount and kind of foreign materials, and impurity have been carried out for grain and other agricultural products (Shedd, 1951; Shedd, 1953; Hukill and Ives, 1955; Giner and Denisienia, 1996; Agullo and Marenya, 2005; Kashaninejad and Tabil, 2009; Amanlou and Zomorodian, 2011).

Haque et al. (1982) developed a model based on the Ergun equation (Eq. 16) to evaluate the effects of airflow and product water content on the pressure drop in a grain layer. The third term of the equation is used to describe the linear dependence of pressure drop on the water content of the product. In the study, the authors found that the pressure drop in sorghum grains increases with decreasing water content and increasing airflow. The variation of the pressure drop with the water content of the product reached about 40% for the same airflow. These results were confirmed by Giner and Denisienia (1996), evaluating the effect of water content on the pressure drop of wheat grains. A reduction of up to 30% in pressure drop was observed. These results are related to the influence of water content on particle size (Mohsenin, 1986). Products with a higher water content are larger than relatively dry products. A high water content generally results in greater porosity; therefore, increasing water content results in a

smaller pressure drop at a given depth (Brooker et al., 1992). In numerical modeling, the pressure drop in the porous medium can be modeled by adding a source term to the moment equation. The origin term comprises viscous and inertial loss terms (Amanlou and Zomorodian, 2010).

$$\frac{\Delta P}{L} = \alpha V + \beta V^2 - \gamma U' V \tag{16}$$

5.1.2. Influence of the water content of the product on the heat exchange

The main thermal properties of grains that govern heat transfer during drying are thermal conductivity (k), specific heat (c_p), and thermal diffusivity (α). During the drying process, the reduction of the water content of the product results in the alteration of these properties. Consequently, the heat exchange with the drying air is altered. If the heat exchange by radiation is significant, the emissivity (ε) of the material surface must be included. In numerical modeling, the reduction in product water content can be modeled as source terms in the governing equations (ElGamal et al., 2017; Sanghi et al., 2018; Guler et al., 2020).

During the period of constant drying, there is a large amount of free water in the product, accelerating the heat and mass transfer processes. At this stage, the water in the product evaporates as free water since its vapor pressure is constant and equal to the vapor pressure of pure water at the temperature of the product. The product temperature, in turn, is also constant and equal to the wet-bulb temperature of the drying air. Proving that heat and mass transfers compensate for each other at this stage (Azhdari and Emami, 2019). In the decreasing rate period, the surface of the material is no longer saturated with water. At this stage, the drying rate is controlled by the diffusion of moisture from the interior of the solid to the surface. In this period, heat transfer is not compensated for by mass transfer because the internal resistance to water transport becomes more significant than the external resistance. Thus, there is a reduction in the migration of water from the interior of the product to its surface and an increase in the temperature of the product, reaching the temperature of the drying air (Brooker et al., 1992).

5.1.3. Influence of drying chamber design

One of the main difficulties in dryers is ensuring the uniformity of hot airflow and temperature distribution in the drying chamber, which can cause products to be unevenly dried (Prommuak et al., 2020). Therefore, the product located close to the air inlet may suffer over-drying. In contrast, the others may not receive a sufficient driving force for drying due to the increase in relative humidity and the decrease in air temperature (Babu et al., 2019).

Optimal drying process knowledge and heat and mass transfer principles are essential for dryer design and optimization. The geometry of the drying chamber (size of air inlet and outlet, outlet angle, air inlet, outlet location, number of trays, and the distance between trays) affects the flow pattern. Thus, the design of dryers is of fundamental importance in optimizing the drying process. Some suggestions that have been made to improve the efficiency of the drying chamber include the use of multiple air inlets; the introduction of guides to divert the air; reduction in the cross-sectional area of the drying chamber from the plenum to the opposite side of the fan; positioning of the air inlet and outlet; among others (Román et al., 2012).

Under actual operating conditions, fans installed at the ambient air inlet, recirculation air inlet, and air outlet (where applicable) can result in uneven and turbulent velocity profiles. However, in most studies that model dryers using CFD, only the drying chamber is discretized. That is, the dynamic operating condition of the fan is not considered (Tegenaw et al., 2019; Zoukit et al., 2019; Benavides- Morán et al., 2020; Guler et al., 2020). This approach is commonly used to simplify modeling and resolutions and reduce computational efforts. Therefore, it is assumed that the velocity profile at the entrance of the plenum chamber resembles a piston flow (Kjaer et al., 2018). In fluid dynamics, piston flow is a simple fluid flow velocity profile model in a tube. Thus, the fluid velocity is assumed to be constant in any cross-section of the tube perpendicular to its axis.

5.2. Turbulence modeling

5.2.1. Turbulence in the drying chamber

Although the direct solution of the Navier-Stokes equations is possible in the case of laminar flows, it is necessary to implement the so-called turbulence models for turbulent flows. This flow regime is generally encountered in drying due to the high Reynolds numbers and complex geometry. The choice of an appropriate turbulence model directly affects the results

obtained in the simulation. Model selection mainly depends on accuracy, time, and computational cost (Malekjani and Jafari, 2018). Turbulence models can be categorized based on the governing equations used. There are two distinct groups of turbulence models, namely: the models that use the calculation of fluctuating quantities, such as the Large Eddy Simulation (LES) and the Reynolds-Averaged Navier-Stokes (RANS) equation models (Brown et al., 2020).

Only the largest and most energetic turbulent structures are resolved in LES models, while the smallest ones are filtered. In this model, turbulent fluctuations are calculated directly, in space and time, but only above a specific length scale. The filtered smaller structures are time-integrated to provide detailed flow field information, accurately representing large-scale turbulent motions (Xiao and Cinnella, 2019). The LES approach is more accurate and has wider applicability than the RANS, even for predicting complex flows. However, this technique is still limited due to the high computational cost and difficulty in tuning (Brown et al., 2020). Although less accurate, RANS models can be considered a cost-effective alternative to investigating large systems or problems in which many parameters need to be varied.

The most common approach to turbulence modeling is the RANS model. This model uses the Reynolds averaging procedure to obtain the RANS equations. This operation eliminates the need to solve the turbulent structures of a flow field directly and instead tries to model the diffusive effect of these structures as a time average (Malekjani and Jafari, 2018). The well-known turbulence closure problem arises from introducing additional terms into the Navier-Stokes equations. In the case of RANS modeling, closure is usually obtained by solving one or more partial differential equations. These closure models are used to couple mean flow to turbulence (Kumar et al., 2020). A summary of the models commonly used in RANS modeling is presented in Table 5. Among these models, the standard k-ε model is one of the most used for modeling turbulence in the drying process due to its adequate convergence.

A summary of the modeling studies of the drying process for different products is presented in Table 6. It can be observed that most of the works presented consider the turbulent nature of this process and use conjugate models for heat and mass transfer. The most used convergence criterion is based on the root mean square (RMS). The RMS is one of the most critical measures of the convergence of an iterative solution, as it directly quantifies the error in the solution of the system of equations. In a CFD analysis, the residual measures the local imbalance of each equation being solved and should ideally be minimized as the solution progresses. Model validation is generally performed by comparing the values predicted by the

model and those obtained experimentally. Therefore, the most used variables for the validation of numerical models include the temperature and water content of the product, temperature, and relative humidity in the drying chamber.

Table 5. Comparison between some Reynolds-Averaged Navier-Stokes (RANS) turbulence models (Guardo et al., 2005; Malekjani and Jafari, 2018)

Model	**Description**	**Advantages**	**Disadvantages**
Standard k-ε	The basis of this model is the transport equations that represent the kinetic energy of turbulence, k, and the rate of dissipation of turbulent kinetic energy, ε.	Good convergence; robust and economical; reasonably accurate; suitable for flows around complex geometries.	Inadequate in some cases due to empirical assumptions on which the model is based (the most critical assumption of this model is to assume an equilibrium condition for turbulence); it is not very accurate in complex flow regimes and severe pressure gradients.
RNG k-ε	The model is derived from the instantaneous Navier-Stokes equations, using the "renormalization group" (RNG) methods. This results in a model with different constants than the Standard k-ε e and additional terms in the transport equations.	Independence from empiricism and consideration of the anisotropy of complex flows; Better results for flows with recirculation.	Convergence difficulties; May Require High Power Computers.
Realizable k-ε	This model satisfies certain mathematical restrictions on normal stresses, consistent with turbulent flow physics. A new model for the dissipation rate (ε) is also used.	Same benefits as RNG k-ε; Better performance in more complex flows.	Some limitations for assuming the "eddy viscosity" as isotropic.
Standard k-ω	The basics of this model are the transport equations representing the kinetic energy of turbulence, k, and the specific dissipation rate ω.	Better performance for flows with adverse pressure gradients.	Convergence is more complicated than Standard k-ε.

Table 6. Modeling studies of the drying process for different products

Reference	**Product**	**Modeling type**	**Flow regime**	**Software**	**Convergence criteria**
Tzempelikos et al., 2015	Quince slices	Not conjugated	Turbulent (Standard k-ω)	ANSYS -FLUENT	RMS < 10^{-6}
Aktaş et al., 2017	Damascus	Conjugated	Turbulent (Standard k-ε)	ANSYS -FLUENT	RMS < 10^{-3}
Cârlescu et al., 2017	Damascus	Conjugated	Laminar	ANSYS -FLUENT	RMS < 10^{-4}
ElGamal et al., 2017	Rice	Conjugated	Laminar	COMSOL	RMS < 10^{-4}
Sanghi et al., 2018	Corn grains	Not conjugated	Turbulent (RNG k-ε)	ANSYS -FLUENT	RMS < 10^{-4}
Chilka e Ranade 2018	Almonds	Conjugated	Turbulent (Standard k-ε)	ANSYS -FLUENT	RMS < 10^{-4}
Ostanek e Ileleji, 2019	Corn grains	Conjugated	Laminar	ANSYS -FLUENT	RMS < 10^{-6}
Iranmanesh et al., 2020	Apple slices	Not conjugated	Turbulent (Standard k-ε)	ANSYS -FLUENT	RMS < 10^{-4}
Afshari, et al., 2021	–	Not conjugated	Turbulent (Standard k-ε)	ANSYS -FLUENT	–
Al-Kayiem and Gitan, 2021	–	Not conjugated	Turbulent (Standard k-ε)	ANSYS -FLUENT	RMS < 10^{-3}
Moghimi et al., 2021	Tomato slices	Not conjugated	Turbulent (Standard k-ε)	ANSYS -FLUENT	RMS < 10^{-6}
Salvatierra-Rojas et al., 2021	Paddy Rice	Not conjugated	Turbulent (Realizable k-ε)	ANSYS -FLUENT	–
Shamsuddeen et al., 2021	Wed sponge	Not conjugated	Turbulent (Standard k-ε)	ANSYS CFX	–
Akari et al., 2022	Fish	Not conjugated	Turbulent (Standard k-ε)	ANSYS CFX	RMS < 10^{-4}
Zhang et al., 2022	Betel nut	Conjugated	Turbulent (Realizable k-ε)	ANSYS -FLUENT	–

5.2.2. Turbulence in porous media

Turbulence modeling for flows in porous media is a very challenging field. This complex flow problem is due to the geometry and multi-scale physics involved. According to Lage (1998), turbulence depends on the geometric structure of the solid matrix of the porous medium but is also affected by porosity. When the particles are far apart (a medium with high porosity), the vortices generated by each particle will have space to develop and thus sustain the energy cascade process, characteristic of turbulent flow. However, when bodies are brought together (lower porosity), vortices generated by one body can be obstructed by neighboring bodies. The energy cascade process will be less effective when reduced porosity, reducing turbulence intensity. Thus, the macroscopic effects of turbulence are more pronounced in porous media with high porosity (Chan et al., 2007; Dong and Xie, 2015).

When considering turbulence in porous media, a recurring discussion concerns which flow characteristics should be considered to define when the flow becomes turbulent. Although controversial, the Reynolds number based on the mean particle diameter (Re_p) is commonly used to characterize the different flow regimes in porous media (Pop and Ingham, 2002). The most accepted classification in the literature is the one proposed by Dybbs and Edwards (1984). From experimental observations at the pore level, the authors concluded that a highly unstable flow regime, qualitatively similar to turbulent flow, is formed for Rep > 300. Numerous studies have used this value over the years to classify turbulent flows in porous media (Pedras and Lemos, 2001; Guardo et al., 2005; Khan and Straatman, 2016b; Jouybari et al., 2020).

Flow problems in porous media can be modeled using two main approaches: microscopic scale and macroscopic scale. In the first one, the modeling is performed at the pore scale, and the transport equations are used in their usual forms. However, high costs and computational efforts are required to model the problem. In the second approach, the porous medium is scaled to the macroscopic level, and the domain is composed of solid and fluid phases. The advantage of this approach is the significant reduction in the computational effort required. However, a mathematical formulation must be expanded to employ the volume average of the mass, momentum, energy, and turbulence transport equations (Khan and Straatman, 2016b). This formulation is based on the assumption that although the velocity and pressure of the fluid may be irregular at the pore scale, locally, the spatial mean values of these quantities show slight variation (Teruel and Uddin, 2009).

Due to the complexity of the internal geometries and the computational effort required, it is impractical to solve the microscopic conservation equations in any porous medium. A

preferable approach is to average the microscopic equations over a representative elementary volume (REV) (Yang et al., 2018). Based on the results obtained at the microscopic scale, macroscopic equations can be modeled using the volume averaging method (Takatsu, 2017). Over the years, different macroscopic turbulent models have been developed for porous media (Nakayma and Kuwahara, 1999; Pedras and Lemos, 2001; Nakayama and Kuwahara, 2008; Teruel and Uddin, 2009; Drouin et al., 2013). Most of these researches try to model turbulent flow in porous media following the traditional approach of modeling turbulence in free flows. Therefore, it is unsurprising that almost all macroscopic models available in the literature are based on the k-ε model, modified to include the solid matrix effect (Jouybari et al., 2015).

Despite the numerous models developed, there is no universal macroscopic form of the k-ε model for porous media. The turbulence models developed differ not only by the average order (time and space) used but also because they are based on different definitions of macroscopic turbulence quantities, such as turbulent kinetic energy and dissipation rate (Teruel and Uddin, 2009). Furthermore, due to the interactions between the fluid and the porous structure, additional terms appear in the transport equations that quantify the influence of the morphology of the medium on the turbulent kinetic energy and the dissipation rate (Khan and Straatman, 2016b). The main difficulty of this modeling is to propose a closure for these additional terms since there is no well-developed general closure expression valid for any morphology. For accurate macroscopic modeling, obtaining the closure of additional terms is necessary by simulating the problem at the microscopic scale or experimental data (Jouybari et al., 2015).

The validation process is another significant difficulty observed in the macroscopic modeling of turbulence in porous media. According to Teruel and Uddin (2009), validating these models is as challenging as, if not more challenging, than their development. The results are expected to be compared with experimental data or obtained using microscopic numerical simulations to validate a model. Getting local point experimental data in a porous medium is difficult, so they are scarce (Karthik et al., 2020). Generally, model validation depends on comparing the results with the corresponding variables obtained by averaging the microscopic results of numerical simulations.

There has been no practical procedure to validate macroscopic turbulence models in porous media. One of the difficulties encountered is that the microscopic results need to be calculated at intermediate scales to compare them to the results of the macroscopic model. This requires that the microscopic simulation be performed in relatively large spaces. Furthermore, when the flow in a relatively large porous region with uniform properties is simulated, the

approximation of the porous medium tends to “homogenize” the variables. This makes it challenging to identify a macroscopic variable that shows a reasonable spatial variation to allow meaningful comparison (Teruel and Uddin 2009). Therefore, rigorous validation is not reported for most macroscopic turbulence models in porous media. These obstacles make this type of modeling in porous media a challenging and little-studied field.

6. CONCLUSION

As discussed in this article, the drying process is essential for conserving agricultural products; currently, different technologies are used for this purpose. The search for more efficient dryers has attracted more and more attention due to the high energy and time consumption. As reported, dryers based on solar energy are gaining more and more space, as energy efficiency can exceed that of conventional sources (biomass, LPG, natural gas). However, the main limitation has been the low reliability due to the temporal intermittence of the source. This has led several researchers to dedicate efforts to studies on thermal energy storage systems. The review on solar dryers showed that in most current studies, thermal storage is still integrated into the drying chamber or energy collection system. This can significantly limit the amount of energy stored and, consequently, the efficiency of the system. The complexity of drying and TES systems has made computer simulations increasingly relevant. Advanced computational tools allow the replication of experimental studies and make it possible to change several variables for optimization purposes. Numerical validation based on experimental data depends on several factors during modeling. The studies presented in this article for drying modeling showed a difference ranging between 1.67 and 14.95% compared to the experimental data. As reported, this tool has been increasingly common in evaluating these systems. However, few researchers have investigated the integration of TES in highly efficient drying systems. Among the studies found, an overall efficiency of the system between 10.53 and 68.55% was observed. The observed specific energy consumption varied between 0.91 and 40.78 MJ kg^{-1}. Although the efficiency of the system is an important factor, it is worth mentioning that drying is a complex operation and several other factors must be observed. Among these, we can mention, the availability of materials, cost, environmental conditions, and complexity of construction and operation. Advanced analyses, including modeling turbulence in porous media, are challenging. The correct use of these tools requires the user to deeply understand the fundamentals of fluid mechanics and heat and mass transfer. This document showed that many advances have been achieved in developing solar drying systems. However,

much remains to be done. It is expected that this work will significantly contribute to the understanding of the current state of these systems and that it will provide the necessary foundation for developing solar dryers integrated with high-efficiency TES systems.

7. REFERENCES

Aboul-Enein, S., El-Sebaii, A.A., Ramadan, M.R.I., El-Gohary, H.G. Parametric study of a solar air heater with and without thermal storage for solar drying applications. **Renewable Energy**, v.21, p.505-522, 2000.

Abubakar, S., Umaru, S., Kaisan, M.U., Umar, U.A., Ashok, B., Nanthagopal, K. Development and performance comparison of mixed-mode solar crop dryers with and without thermal storage. **Renewable Energy**, v.128, p.285-298, 2018.

Achkari, O., El Fadar, A. Latest developments on TES and CSP technologies – Energy and environmental issues, applications and research trends. **Applied Thermal Engineering**, v.167, 114806, 2020.

Afshari, F., Tuncer, A.D., Sözen, A., Çiftçi, E., Khanlari, A. Experimental and numerical analysis of a compact indirect solar dehumidification system. **Solar Energy**, v.226, p.72-84, 2021.

Agullo, J.O., Marenya, M.O. Airflow resistance of parchment arabica coffee. **Biosystems engineering**, v.91, p.149-156, 2005.

Akari, E. O., Fetuga, I. A., Olakoyejo, O. T., Shitta, M. B., Oluwatusin, O., Gbegudu, J. K., Siqueira, A. M. de O. Numerical simulation of optimal inlet air temperature of a forced convective fish cabinet rotary dryer. **The Journal of Engineering and Exact Sciences**, v.8, p.14157–01e, 2022.

Aktaş, M., Sözen, A., Amini, A., Khanlari, A. Experimental analysis and CFD simulation of infrared apricot dryer with heat recovery. **Drying Technology**, v.35, p.766-783, 2017.

Al-Kayiem, H.H., Gitan, A.A. Flow uniformity assessment in a multi-chamber cabinet of a hybrid solar dryer. **Solar Energy**, v.224, p.823-832, 2021.

Alam, T., Balam, N.B., Kulkarni, K.S., Siddiqui, M.I.H., Kapoor, N.R., Meena, C.S., Kumar, A., Cozzolino, R. (2021). Performance Augmentation of the Flat Plate Solar Thermal Collector: A Review. **Energies** v.14, 6203.

Altobelli, F., Condorí, M., Duran, G., Martinez, C. Solar dryer efficiency considering the total drying potential. Application of this potential as a resource indicator in north-western Argentina. **Solar Energy**, v.105, p.742-759, 2014.

Álvarez-Sánchez, F., Flores-Prieto, J., García-Valladares, O. Annual Thermal Performance of an Industrial Hybrid Direct–Indirect Solar Air Heating System for Drying Applications in Morelos-México. **Energies**, v.14, 5417, 2021.

Amanlou, Y., Zomorodian, A. Applying CFD for designing a new fruit cabinet dryer. **Journal of Food Engineering**, v.101, p.8-15, 2010.

Amanlou, Y., Zomorodian, A. Evaluation of air flow resistance across a green fig bed for selecting an appropriate pressure drop prediction equation. **Food and Bioproducts Processing**, v.89, p.157-162, 2011.

Amar, B.M.A., Hossain, M.A., Gottschalk, K. Design and performance evaluation of a new hybrid solar dryer for banana. **Energy Conversion and Management**, v.51, 2010, p.813-820, 2010.

Ananno, A.A., Masud, M.H., Dabnichki, P., Ahmed, A. Design and numerical analysis of a hybrid geothermal PCM flat plate solar collector dryer for developing countries. **Solar Energy**, v.196, p.270-286, 2020.

Andharia, J.K., Markam, B., Dzhonova, D., Maiti, S. A comparative performance analysis of sensible and latent heat based storage in a small-scale solar thermal dryer. **Journal of Energy Storage**, v.45, 103764, 2022.

ANSYS, CFX. **ANSYS CFX-Solver Modeling Guide**. Release 2019 R1.

Araujo, M.E.V., Barbosa, E.G., Lopes, R.P., Corrêa, P.C., Barbosa, E.G. Infrared drying of pear slices: Drying kinetics, energy, and exergy analysis. **Journal of Food Process Engineering**, v.44, e13915, 2021.

Araujo, M.E.V., Barbosa, E.G., Oliveira, A.C.L., Milagres, R.S., Pinto, F.A.C., Corrêa, P.C. Physical properties of yellow passion fruit seeds (*Passiflora edulis*) during the drying process. **Scientia Horticuturae**, v. 261, 109032, 2020.

Arun, K.R., Kunal, G., Srinivas, M., Kumar, C.S.S., Mohanraj, M., Jayaraj, S. Drying of untreated Musa nendra and Momordica charantia in a forced convection solar cabinet dryer with thermal storage. **Energy**, v.192, 116697, 2020.

Atalay, H. Assessment of energy and cost analysis of packed bed and phase change material thermal energy storage systems for the solar energy-assisted drying process. **Solar Energy**, v.198, p.124-138, 2020.

Atalay, H. Performance analysis of a solar dryer integrated with the packed bed thermal energy storage (TES) system. **Energy**, v.172, p.1037-1052, 2019.

Ayensu, A. Dehydration of food crops using a solar dryer with convective heat flow. **Solar Energy**, v.59, p.121-126, 1997.

Azaizia, Z., Kooli, S., Hamdi, I., Elkhal, W., Guizani, A.A. Experimental study of a new mixed mode solar greenhouse drying system with and without thermal energy storage for pepper. **Renewable Energy**, v.145, p.1972-1984, 2020.

Azhdari, E., Emami, A. Analytical and numerical study of drying of tomato in non-shrinkage and shrinkage model. **Mathematics and Computers in Simulation,** v.166, p.253-265, 2019.

Baba, Y.F., Al Mers, A., Ajdad, H. Dimensionless model based on dual phase approach for predicting thermal performance of thermocline energy storage system: Towards a new approach for thermocline thermal optimization. **Renewable Energy**, v.153, p.440-455, 2020.

Babu, A.K., Kumaresan, G., Antony Aroul Raj, V., Velraj, R. CFD studies on different configurations of drying chamber for thin-layer drying of leaves. **Energy Sources, Part A: Recovery, Utilization, and Environmental Effects**, p.1-13, 2019.

Bal, L.M., Satya, S., Naik, S.N. Solar dryer with thermal energy storage systems for drying agricultural food products: A review. **Renewable and Sustainable Energy Reviews**, v.14, p.2298-2314, 2010.

Barbosa, E.G., Araujo, M.E.V., Lopes, R.P., Martins, M.A., Moraes, M.J., Barbosa, E.G., Falconí, J.H.H. Exergetic, economic and environmental (3E) analysis of a low cost solar heater in different configurations. **Renewable Energy** v.160, p.1096–1104, 2020a.

Barbosa, E.G., Araújo, M.E.V.D., Moraes, M.J.D., Martins, M.A., Alves, B.G.X., Barbosa, E.G., 2019. Influence of the absorber tubes configuration on the performance of low cost solar water heating systems. **Journal of Cleaner Production**, v.222, p.22–28, 2019.

Barbosa, E.G., Martins, M.A., Araujo, M.E.V., Renato, N.S., Zolnier, S., Pereira, E.G., Resende, M.O. Experimental evaluation of a stationary parabolic trough solar collector: Influence of the concentrator and heat transfer fluid. **Journal of Cleaner Production**, v.276, 124174, 2020b.

Bekkioui, N., El Hakiki, S., Rachadi, A., Ez-Zahraouy, H. One-year simulation of a solar wood dryer with glazed walls in a Moroccan climate. **Renewable Energy**, v.155, p.770-782, 2020.

Bellos, E., Daniil, I., Tzivanidis, C. Multiple cylindrical inserts for parabolic trough solar collector. **Applied Thermal Engineering**, v.143, p.80-89, 2018.

Benavides-Morán, A., Cubillos, A., Gómez, A. Spray drying experiments and CFD simulation of guava juice formulation. **Drying Technology**, p.1-16, 2020.

Berrocal, A., Moya, R., Bond, B., Rodriguez-Solis, M., Muñoz, F., Pérez, D. Chedule modification of drying rate to decrease the drying time of juvenile tectona grandisl. Wood. **Wood and Fiber Science**, v.49, p.373-385, 2017.

Bhardwaj, A.K., Humar, R., Kumar, R., Kumar, S., Goel, B., Chauhan, R. Energy and exergy analyses of drying medicinal herb in a novel forced convection solar dryer integrated with SHSM and PCM. **Sustainable Energy Technologies and Assessments**, v.45, 101119, 2021.

Bhardwaj, A.K., Kumar, R., Chauhan, R. Experimental investigation of the performance of a novel solar dryer for drying medicinal plants in Western Himalayan region. **Solar Energy**, v.177, p.395-407, 2019.

Biencinto, M., González, L., Valenzuela, L., Zarza, E. A new concept of solar thermal power plants with large-aperture parabolic-trough collectors and CO_2 as working fluid. **Energy Conversion and Management**, v.199, 1120301, 2019.

Bozorg, M.V., Hossein Doranehgard, M., Hong, K., Xiong, Q. CFD study of heat transfer and fluid flow in a parabolic trough solar receiver with internal annular porous structure and synthetic oil – Al_2O_3 nanofluid. **Renewable Energy**, v.145, p.2598-2614, 2020.

Brooker, D.B., Bakker-Arkema, F.W., and Hall, C.W. **Drying and storage of grains and oilseeds**. The AVI Publishing Company, Westport, Connecticut, USA, 1992.

Brown, G.J., Fletcher, D.F., Leggoe, J.W., Whyte, D.S. Application of hybrid RANS-LES models to the prediction of flow behaviour in an industrial crystalliser. **Applied Mathematical Modelling**, v.77, p.1797-1819, 2020.

Cabeza, L.F., Solé, A., Fontanet, X., Barreneche, C., Jové, A., Gallas, M., Prieto, C., Férnandez, A. I. Thermochemical energy storage by consecutive reactions for higher efficient concentrated solar power plants (CSP): Proof of concept. **Applied Energy**, v.185, 2017.

Cârlescu, P.-M., Arsenoaia, V., Roşca, R., Ţenu, I. CFD simulation of heat and mass transfer during apricots drying. **LWT - Food Science and Technology**, v.85, p.479-486, 2017.

Carvalho, R.L., Vicente, E.D., Tarelho, L.A.C., Jensen, O.M. Wood stove combustion air retrofits: A low-cost way to increase energy savings in dwellings. **Energy and Buildings**, v.164, p.140-152, 2018.

Castro, A.M., Mayorga, E.Y., Moreno, F.L. Mathematical modelling of convective drying of fruits: A review. **Journal of Food Engineering**, v.223, p.152-167, 2018.

Chaatouf, D., Salhi, M., Raillani, B., Amraqui, S., Mezrhab, A., Naji, H. Parametric analysis of a sensible heat storage unit in an indirect solar dryer using computational fluid dynamics. **Journal of Energy Storage**, v.49, 104075, 2022.

Chan, H.C. Leu, J.M., Lai, C.J. Velocity and turbulence field around permeable structure: Comparisons between laboratory and numerical experiments. **Journal of Hydraulic Research**, v.45, p.216-226, 2007.

Chaouch, W.B., Khellaf, A., Mediani, A., Slimani, M.E.A., Loumani, A., Hamid, A. Experimental investigation of an active direct and indirect solar dryer with sensible heat storage for camel meat drying in Saharan environment. **Solar Energy**, v.174, p.328-241, 2018.

Chauhan, P.M., Choudhury, C., Garg, H.P. Comparative performance of coriander dryer coupled to solar air heater and solar air-heater-cum-rockbed storage. **Applied Thermal Engineering**, v.16, p.475-486, 1996.

Chavan, B.R., Yakupitiyage, A., Kumar, S. Mathematical Modeling of Drying Characteristics of Indian Mackerel (Rastrilliger kangurta) in Solar-Biomass Hybrid Cabinet Dryer. **Drying Technology**, v.26, p.1552-1562, 2008.

Chen, H., Chen, K., Yang, M., Xu, P. A fractal capillary model for multiphase flow in porous media with hysteresis effect. **International Journal of Multiphase Flow**, v.125, 103208, 2020.

Chilka, A.G., Ranade, V.V. CFD modelling of almond drying in a tray dryer. **The Canadian Journal of Chemical Engineering**, v.97, p.560-572, 2018.

Condorí, M., Duran, G., Echazú, R, Altobelli, F. Semi-industrial drying of vegetables using an array of large solar air collectors. **Energy for Sustainable Development**, v.37, p.1-9, 2017.

Daghigh, R., Shahidian, R., Oramipoor, H. A multistate investigation of a solar dryer coupled with photovoltaic thermal collector and evacuated tube collector. **Solar Energy**, v.199, p.694-703, 2020.

Defraeye, T. Advanced computational modelling for drying processes – A review. **Applied Energy**, v.131, p.323-344, 2014.

Devahastin, S. Pitaksuriyarat, S. Use of latent heat storage to conserve energy during drying and its effect on drying kinetics of a food product. **Applied Thermal Engineering**, v.26, p.1705-1713, 2006.

Dong, M. Xie, M.Z. Numerical Investigation on Mass Dispersion in Turbulent Flows through Porous Media with High Porosity. **Numerical Heat Transfer, Part A: Applications**, v.67, p.293-312, 2015.

Drouin, M., Grégoire, O., Simonin, O. A consistent methodology for the derivation and calibration of a macroscopic turbulence model for flows in porous media. **International Journal of Heat and Mass Transfer**, v.63, p.401-413, 2013.

Dybbs, A., Edwards, R.V. A new look at porous media fluid mechanics – Darcy to turbulent. In: Bear, J., Corapcioglu, M.Y., **Fundamentals of Transport Phenomena in Porous Media**, p.199-256, Martinus Nijhoff Publishers, 1984.

El Khadraoui, A., Bouadila, S., Kooli, S., Farhat, A., Guizani, A. Thermal behavior of indirect solar dryer: Nocturnal usage of solar air collector with PCM. **Journal of Cleaner Production**, v.148, p.37-48, 2017.

ElGamal, R.A., Kishk, S.S., ElMasry, G.M. Validation of CFD models for the deep-bed drying of rice using thermal imaging. **Biosystems Engineering**, v.161, p.135-144, 2017.

Faraj, K., Khaled, M., Faraj, J., Hachem, F., Castelain, C. Phase change material thermal energy storage systems for cooling applications in buildings: A review. **Renewable and Sustainable Energy Reviews**, v.119, 109579, 2020.

Feng, P.H., Zhao, B.C., Wang, R.Z. Thermophysical heat storage for cooling, heating, and power generation: A review. **Applied Thermal Engineering**, v.166, 114728, 2020.

Fernández-Seara, J., Uhía, F.J., Sieres, J. Experimental analysis of a domestic electric hot water storage tank. Part II: dynamic mode of operation. **Applied Thermal Engineering**, v.27, p.137-144, 2007.

Fudholi, A., Sopian, K., Othman, M.Y., Ruslan, M.H. Energy and exergy analyses of solar drying system of red seaweed. **Energy and Buildings**, v.68, p.121-129, 2014.

Garg, H.P., Sharma, V.K., Mahajan, R.B., Bhargave, A.K. Experimental study of an inexpensive solar collector cum storage system for agricultural uses. **Solar Energy**, v.35, p.321-331, 1985.

Gilago, M.C., Mugi, V.R., Chandramohan, V.P. Energy-exergy and environ-economic (4E) analysis while drying ivy gourd in a passive indirect solar dryer without and with energy storage system and results comparison. **Solar Energy**, v.240, 2022.

Giner, S.A., Denisienia, E. P. **Journal of Agricultural Engineering Research**, v.63, p.73-85, 1996.

Goud, M., Reddy, M.V.V., Chandramohan, V.P., Suresh, S. A novel indirect solar dryer with inlet fans powered by solar PV panels: Drying kinetics of Capsicum Annum and Abelmoschus esculentus with dryer performance. **Solar Energy**, v.194, p.871-885, 2019.

Guardo, A., Coussirat, M., Larrayoz, M.A., Recasens, F., Egusquiza, E. Influence of the turbulence model in CFD modeling of wall-to-fluid heat transfer in packed beds. **Chemical Engineering Science**, v.60, p.1733-1742, 2005.

Guler, H.O., Sozen, A., Tuncer, A.D., Afshari, F., Khanlari, A., Sirin C., Gungor, A. Experimental and CFD survey of indirect solar dryer modified with low-cost iron mesh. **Solar Energy**, v.197, p.371-384, 2020.

Hadibi, T., Boubekri, A., Mennouche, D., Benhamza, A., Abdenouri, N. 3E analysis and mathematical modelling of garlic drying process in a hybrid solar-electric dryer. **Renewable Energy**, v.170, p.1052-1069, 2021.

Haque, E., Ahmed, Y.K., Deyoe, C.W. Static pressure drop in a fixed bed of grain as affected by grain moisture content. **Transactions of the ASAE**, v. 25, p.1095-1098, 1982.

He, Z., Wang, X., Du, X., Amjad, M., Yang, L., Xu, C. Experiments on comparative performance of water thermocline storage tank with and without encapsulated paraffin wax packed bed. **Applied Thermal Engineering**, v.147, p.188-197, 2019.

Hérnandez-Callejo, L., Gallardo-Saavedra, S., Alonso-Gómez, V. A review of photovoltaic systems: Design, operation and maintenance. **Solar Energy**, v.188, p.426-440, 2019.

Hukill, W.V., Ives, N.C. Radial airflow resistance of grain. **Agricultural Engineering**, v.36, p.332-335, 1955.

IEA – International Energy Agency. **Technology Roadmap: Concentrating Solar Power**. OECD/IEA, France, 2010. 52p.

Iranmanesh, M., Akhijahani, H.S., Jahromi, M.S.B. CFD modeling and evaluation the performance of a solar cabinet dryer equipped with evacuated tube solar collector and thermal storage system. **Renewable Energy**, v.145, p.1192-1213, 2020.

Jahromi, M.S.B. Iranmanesh, M. Akhijahani, H.S. Thermo-economic analysis of solar drying of Jerusalem artichoke (Helianthus tuberosus L.) integrated with evacuated tube solar collector and phase change material. **Journal of Energy Storage**, v.52, Part A, 104688, 2022.

Jain, D. Modeling the system performance of multi-tray crop drying using an inclined multi-pass solar air heater with in-built thermal storage. **Journal of Food Engineering**, v.71, p.44-54, 2005.

Jain, D., Tewari, P. Performance of indirect through pass natural convective solar crop dryer with phase change thermal energy storage. **Renewable Energy**, v.80, p.244-250, 2015.

Jain, R., Paul, A.S., Sharma, D., Panwar, N.L. Enhancement in thermal performance of solar dryer through conduction mode for drying of agricultural produces. **Energy Nexus**, v.9, 100182, 2023.

Jouybari, N.F., Lundström, T.S., Hellström, J.G.I. Investigation of thermal dispersion and intra-pore turbulent heat flux in porous media. **International Journal of Heat and Fluid Flow**, v.81, 108523, 2020.

Jouybari, N.F., Maerefat, M., Nimvari, M.E. A Macroscopic Turbulence Model for Reacting Flow in Porous Media. **Transport in Porous Media**, v.106, p.355-381, 2015.

Jubaer, H., Afshar, S., Xiao, J. Chen, X.D., Selomulya, C., Woo, M.W. On the effect of turbulence models on CFD simulations of a counter-current spray drying process. **Chemical Engineering Research and Design**, v.141, p.592-607, 2019.

Kalaiarasi, G., Velraj, R., Vanjeswaran, M.N., Ganesh Pandian, N. Experimental analysis and comparison of flat plate solar air heater with and without integrated sensible heat storage. **Renewable Energy**, v.150, p.255-265, 2020.

Kant, K., Shukla, A., Sharma, A., Kumar, A., Jain, A. Thermal energy storage based solar drying systems: A review. **Innovative Food Science & Emerging Technologies**, v.34, p.86-99, 2016.

Kareem, M.W., Habib, K., Ruslan, M.H., Saha, B.B. Thermal performance study of a multi-pass solar air heating collector system for drying of Roselle (Hibiscus sabdariffa). **Renewable Energy**, v.113, p.281-292, 2017.

Karki, S., Haapala, K.R., Fronk, B.M. Investigation of the combined efficiency of a solar/gas hybrid water heating system. **Applied Thermal Engineering**, v.149, p.1035-1043, 2019.

Karthik, G.M., Thaker, A.H., Buwa, V.V. Particle-resolved simulations of catalytic fixed bed reactors: Comparison of turbulence models, LES and PIV measurements. **Powder Technology**, v. 361, p.189-200, 2020.

Kashaninejad, M., Tabil, L.G. Resistance of bulk pistachio nuts (Ohadi variety) to airflow. **Journal of Food Engineering**, v.90, p.104-109, 2009.

Khan, F.A., Straatman, A.G. A conjugate fluid-porous approach to convective heat and mass transfer with application to produce drying. **Journal of Food Engineering**, v.179, p.55-67, 2016a.

Khan, F.A., Straatman, A.G. Closure of a macroscopic turbulence and non-equilibrium turbulent heat and mass transfer model for a porous media comprised of randomly packed spheres. **International Journal of Heat and Mass Transfer**, v.101, p.1003-1015, 2016b.

Khouya, A. Effect of regeneration heat and energy storage on thermal drying performance in a hardwood solar kiln. **Renewable Energy**, v.155, p.783-799, 2020.

Khouya, A., Draoui, A. Computational drying model for solar kiln with latent heat energy storage: Case studies of thermal application. **Renewable Energy**, v.130, p.796-831, 2019.

Kjaer, L.S., Poulsen, M., Sorensen, K., Condra, T. Modelling of hot air chamber designs of a continuous flow grain dryer. **Engineering Science and Technology, an International Journal**, v.21, p.1047-1055, 2018.

Kouhila, M., Moussaoui, H., Lamsyehe, H., Tagnamas, Z., Bahammou, Y., Idliman, A., Lambarrar, A. Drying characteristics and kinetics solar drying of Mediterranean mussel (*Mytilus galloprovincilis*) type under forced convection. **Renewable Energy**, v.147, p.833-844, 2020.

Kreith, F. **Principles of Heat Transfer**. Harper and Row, New York, 1976.

Kumar, G.S., Nagarajan, D., Chidambaram, L.A., Kumaresan, V., Ding, Y., Velraj, R. Role of PCM addition on stratification behaviour in a thermal storage tank – An experimental study. **Energy**, V.115, p.1168-1178, 2016.

Kumar, L., Hasanuzzaman, M., Rahim, N.A. Global advancement of solar thermal energy technologies for industrial process heat and its future prospects: A review. **Energy Conversion and Management**, v.195, p.885-908, 2019.

Kumar, P., Schmelzer, M., Dwight, R.P. Stochastic turbulence modeling in RANS simulations via multilevel Monte Carlo**. Computers and Fluids**, v.201, 104420, 2020.

Kuntikana, P., Prabhu, S.V. Thermal investigations on self-aspirating type radial flow burners with induced swirl. **Applied Thermal Engineering**, v.161, 114118, 2019.

Lage, J.L. The fundamental theory of flow through permeable media from darcy to turbulence. In: Pop, I., Ingham, D.B. **Transport phenomena in porous media**. Elsevier, p.1-30, 1998.

Lakshmi, D.V.N. Muthukumar, P., Layek, A., Nayak, P.K. Drying kinetics and quality analysis of black turmeric (Curcuma caesia) drying in a mixed mode forced convection solar dryer integrated with thermal energy storage. **Renewable Energy**, v.120, p.23-34, 2018.

Lakshmi, D.V.N., Muthukumar, P., Nayak, P.K. Experimental investigations on active solar dryers integrated with thermal storage for drying of black pepper. **Renewable Energy**, v.167, p.728-739, 2021.

Lee, S.Y., Oh, K.C., Lee, C.G., Cho, L.H., Park, S.Y., Jeong, I.S., Kim, D.H. Improvement of thermal efficiency of wood pellet boilers through the refractory insulation in a combustion chamber and fire tube and baffle modification. **Energy**, v.161, p.1115-1121, 2018.

Li, H., Zheng, C., Lu, J., Tian, L., Lu, Y., Ye, Q., Luo, W., Zhu, X. Drying kinetics of coal under microwave irradiation based on a coupled electromagnetic, heat transfer and multiphase porous media model. **Fuel**, v.256, 115966, 2019.

Lingayat, A.B., Chandramohan, V.P., Raju, V.R.K., Meda, V. A review on indirect type solar dryers for agricultural crops – Dryer setup, its performance, energy storage and important highlights. **Applied Energy**, v.258, 114005, 2020.

Lopéz-Vidaña, E.C., Méndez-Lagunas, L.L., Rodríguez-Ramírez, J. Efficiency of a hybrid solar–gas dryer. **Solar Energy**, v.93, p.23-31, 2013.

Madhankumar, S., Viswanathan, K., Wu, W. Energy, exergy and environmental impact analysis on the novel indirect solar dryer with fins inserted phase change material. **Renewable Energy**, v.176, p.280-294, 2021.

Madhlopa, A., Ngwalo, G. Solar dryer with thermal storage and biomass-backup heater. **Solar Energy**, v.81, p.449-462, 207.

Malekjani, N., Jafari, S.M. Simulation of food drying processes by Computational Fluid Dynamics (CFD); recent advances and approaches. **Trends in Food Science & Technology**, v.78, p.206-223, 2018.

Maroulis, Z.B., Saravacos, G.D. Solar heating of air for drying agricultural products. **Solar & Wind Technology**, v.3, p.127-134, 1986.

Mehari, A., Xu, Z.Y., Wang, R.Z. Thermal energy storage using absorption cycle and system: A comprehensive review. **Energy Conversion and Management**, v.206, 112482, 2020.

Mehos, M., Turchi, C., Vidal, J., Wagner, M., Ma, Z., Ho, C., Kolb, W., Andraka, C., Kruizenga, A. **Concentrating solar power Gen3 demonstration roadmap**. National Renewable Energy Lab.(NREL), Golden, CO (United States), 2017

Menon, A., Stokceska, V., Tassou, S. A systematic review on the recent advances of the energy efficiency improvements in non-conventional food drying technologies. **Trends in Food Science & Technology**, 2020. No prelo. https://doi.org/10.1016/j.tifs.2020.03.014

Moghimi, P., Rahimzadeh, H., Ahmadpour, A. Experimental and numerical optimal design of a household solar fruit and vegetable dryer. **Solar Energy**, v.214, p.575-587, 2021.

Mohsenin, N.N. **Physical properties of plant and animal materials**. New York: Gordon and Breach Publishers, 1986. 841p.

Motahayyer, M., Arabhosseini, A., Samimi-Akhijahani, H. Numerical analysis of thermal performance of a solar dryer and validated with experimental and thermo-graphical data. **Solar Energy**, v.193, p.692-705, 2019.

Murali, S., Amulya, P.R., Alfiya, P.V., Delfiya, D.S.A., Samuel, M.P. Design and performance evaluation of solar - LPG hybrid dryer for drying of shrimps. **Renewable Energy**, v.147, p.2417-2428, 2020.

Nakayama, A., Kuwahara, F. A general macroscopic turbulence model for flows in packed beds, channels, pipes, and rod bundles. **Journal of Fluids Engineering**, v.130, 101205, 2008.

Ndukwu, M.C., Simo-Tagne, M., Abam, F.I., Onwuka, O.S., Príncipe, S., Bennamoun, L. Exergetic sustainability and economic analysis of hybrid solar-biomass dryer integrated with copper tubing as heat exchanger. **Heliyonn**, v.6, e03401, 2020.

Norouzi, A.M., Siavashi, M., Khaliji Oskouei, M. Efficiency enhancement of the parabolic trough solar collector using the rotating absorber tube and nanoparticles. **Renewable Energy**, v.145, p.569-584, 2020.

Okoroigwe, E.C., Ndu, E.C., Okoroigwe, F.C. Comparative evaluation of the performance of an improved solar-biomass hybrid dryer. **Journal of Energy in Southern Africa**, v.26, p.38-51, 2015.

Oró, E., Chiu, J., Martin, V., Cabeza, L.F. Comparative study of different numerical models of packed bed thermal energy storage systems. **Applied Thermal Engineering**, v.50, p.384-392, 2013.

Ostanek, J. Ileleji, K. Conjugate heat and mass transfer model for predicting thin-layer drying uniformity in a compact, crossflow dehydrator. **Drying Technology**, v.38, p.1-18, 2019.

Pedras, M.H.J. Lemos, M.J.S. Macroscopic turbulence modeling for incompressible flow through undeformable porous media. **International Journal of Heat and Mass Transfer**. v.44, p.1081-1093, 2001.

Pelay, U., Luo, L., Fan, Y., Stitou, D., Rood, M. Thermal energy storage systems for concentrated solar power plants. **Renewable and Sustainable Energy Reviews**, v.79, p.82-100, 2017.

Phometop, K., Ozarska, B., Belleville, B., Brodie, G.I. Comparing two intermittent drying schedules for timber drying quality. **Drying Technology**, v.37, p.186-197, 2018.

Pop, I., Ingham, D.B. **Transport phenomena in porous media II**. Elsevier, 449p. 2002.

Prasad, J., Vijay, V.K. Experimental studies on drying of Zingiber officinale, Curcuma longa l. and Tinospora cordifolia in solar-biomass hybrid drier. **Renewable Energy**, v.30, p.2097-2109, 2005.

Prommuak, C., Tharangkool, N., Pasavant, P., Ponpesh, P., Jarunglumlert, T. Computational fluid dynamic design of spent coffee ground cabinet dryer using recycled heat from air compressor. **Chemical Engineering Research and Design**, v.153, p.75-84, 2020.

Ramana, A.S., Venkatesh, R., Antony Aroul Raj, V., Velraj, R. Experimental investigation of the LHS system and comparison of the stratification performance with the SHS system using CFD simulation. **Solar Energy**, v.103, p.378-389, 2014.

REN21 – Renewable Energy Policy Network For The 21st Century. **Renewable Energy global status report**, 2018. Available in: <https://www.globalwomennet.org/wp-content/uploads/2019/06/gsr_2019_full_report_en.pdf>. Acesso em: 18, fev., 2020.

Rendall, J., Abu-Heiba, A., Gluesenkamp, K., Nawaz, K., Worek, W., Elatar, A. Nondimensional convection numbers modeling thermally stratified storage tanks: Richardson's number and hot-water tanks. **Renewable and Sustainable Energy Reviews**, v.150, 111471, 2021.

Riahi, A., Ben Haj Ali, A., Fadhel, A., Guizani, A., Balghouthi, M. Performance investigation of a concentrating photovoltaic thermal hybrid solar system combined with thermoelectric generators. **Energy Conversion and Management**, v.205, 112377, 2020.

Román, F., Strahl-Schafer, V., Hensel, O. Improvement of air distribution in a fixed-bed dryer using computational fluid dynamics. **Biosystems Engineering**, v.112, p.359-369, 2012.

Romaní, J., Gasia, J., Solé, A., Takasu, H., Kato, Y., Cabeza, L.F. Evaluation of energy density as performance indicator for thermal energy storage at material and system levels. **Applied Energy**, v.235, p.954-962, 2019.

Salvatierra-Rojas, A., Ramaj, I., Romuli, S., Müller., J. CFD-Simulink Modeling of the Inflatable Solar Dryer for Drying Paddy Rice. **Applied Sciences,** v.11, 3118, 2021.

Sanghi, A., Ambrose, R.P.K., Maier, D. CFD simulation of corn drying in a natural convection solar dryer. **Drying Technology**, v.36, p.859-870, 2018.

Shamsuddeen, M.M., Cha, DA., Kim, SC., Kanemoto, T., Kim, J. Performance Study of a Hybrid Heat Pump Dryer based on Numerical Analysis and Experimental Set-up. **Journal of Thermal Science**, v.30, p.111–122, 2021.

Shedd, C.K. Resistance of grains and seeds to air flow. **Agricultural Engineering**, v.34, p.616-619, 1953.

Shedd, C.K. Some new data on resistance of grains to air flow. **Agricultural Engineering**, v.32, p.493-495, 1951.

Simo-Tagne, M., Etala, H.D.T., Tagne, A.T., Ndukwu, M.C., Marouani, M.E. Energy, environmental and economic analyses of an indirect cocoa bean solar dryer: A comparison between natural and forced convections. **Renewable Energy**, v.187, p.1154-1172, 2022.

Simo-Tagne, M., Ndukwu, M.C., Zoulalian, A., Bennamoun, L., Kifani-Sahban, F., Rogaume, Y. Numerical analysis and validation of a natural convection mix-mode solar dryer for drying red chilli under variable conditions. **Renewable Energy**, v.151, p.659-673, 2020.

Singh, S., Gill, R.S., Hans, V.S., Singh. A novel active-mode indirect solar dryer for agricultural products: Experimental evaluation and economic feasibility. **Energy**, v.222, 119956, 2021.

Sözen, A., Kazancıoğlu, F.Ş., Tuncer, A.D., Khanlari, A., Bilge, Y.C., Gungor, A. Thermal performance improvement of an indirect solar dryer with tube-type absorber packed with aluminum wool. **Solar Energy**, v.217, p.328-341, 2021.

SunShot. SunShot Vision Study, **Energy Efficiency and Renewable Energy**. U.S. Department of Energy (2012). NREL Report No. BK5200-47927; DOE/GO-102012-3037.

Takatsu, Y. Modification of the fundamental theorem for transport phenomena in porous media. **International Journal of Heat and Mass Transfer**, v.115, p.1109-1120, 2017.

Tegenaw, P.D., Gebrehiwot, M.G., Vanierschot, M. On the comparison between computational fluid dynamics (CFD) and lumped capacitance modeling for the simulation of transient heat transfer in solar dryers. **Solar Energy**, v.184, p.417-425, 2019.

Teruel, F.E., Uddin, R. A new turbulence model for porous media flows. Part I: Constitutive equations and model closure. **International Journal of Heat and Mass Transfer**, v.52, p.4264-4272, 2009.

Tippayawong, N., Tantakitti, C., Thavornun, S. Energy efficiency improvements in longan drying practice. **Energy**, v.33, p.1137-1143, 2008.

Tiwari, G.N., Singh, A.K., Bhatia, P.S. Experimental simulation of a grain drying system. **Energy Conversion and Management**, v.35, p.453-458, 1994.

Tzempelikos, D.A., Mitrakos, D., Vouros, A.P., Bardakas, A.V., Filios, A.E., Margaris, D.P. Numerical modeling of heat and mass transfer during convective drying of cylindrical quince slices. **Journal of Food Engineering**, v.156, p.10-21, 2015.

Vallespir, F., Rodríguez, O., Cárcel, J.A., Rosselló, C., Simal, S. Ultrasound assisted low-temperature drying of kiwifruit: Effects on drying kinetics, bioactive compounds and antioxidant activity. **Journal of the Science of Food and Agriculture**, v.99, p.2901-2909.

Vásquez, J., Reyes, A., Pailahueque, N. Modeling, simulation and experimental validation of a solar dryer for agro-products with thermal energy storage system. **Renewable Energy**, v.139, p.1375-1390, 2019.

Wan, Z., Wei, J., Qaisrani, M.A., Fang, J., Tu, N. Evaluation on thermal and mechanical performance of the hot tank in the two-tank molten salt heat storage system. **Applied Thermal Engineering**, v.167, 114775, 2020.

Wang, W., Li, M., Hassanien, R.H.E., Wang, Y., Yang, L. Thermal performance of indirect forced convection solar dryer and kinetics analysis of mango. **Applied Thermal Engineering**, v.134, p.310-321, 2018.

Winkelmann, U., Kämper, C., Höffer, R., Forman, P., Ahrens, M.A., Mark, P. Wind actions on large-aperture parabolic trough solar collectors: Wind tunnel tests and structural analysis. **Renewable Energy**, v.146, p.2390-2407, 2020.

Wu, S., Zhou, C., Doroodchi, E., Nelore, R., Moghtaderi, B. A review on high-temperature thermochemical energy storage based on metal oxides redox cycle. **Energy Conversion and Management**, v.168, p.421-453, 2018.

Xiao, H., Cinnella, P. Quantification of model uncertainty in RANS simulations: A review. **Progress in Aerospace Sciences**, v.108, p.1-31, 2019.

Yadav, S., Chandramohan, V.P. Performance comparison of thermal energy storage system for indirect solar dryer with and without finned copper tube. **Sustainable Energy Technologies and Assessments**, v.37, 100609, 2020.

Yahya, M., Fahmi, H., Fudholi, A., Sopian, K. Performance and economic analyses on solar-assisted heat pump fluidised bed dryer integrated with biomass furnace for rice drying. **Solar Energy**, v.174, p.1058-1067, 2018.

Yan, Y., Wang, K., Clough, P.T., Anthony, E.J. Developments in calcium/chemical looping and metal oxide redox cycles for high-temperature thermochemical energy storage: A review. **Fuel Processing Technology**, v.199, 106280, 2020.

Yang, G., Weigand, B., Terzis, A., Weishaupt, K., Helmig, R. Numerical Simulation of Turbulent Flow and Heat Transfer in a Three-Dimensional Channel Coupled with Flow Through Porous Structures. **Transport in Porous Media**, v.122, p.145-167, 2018.

Yang, X. Cai, Z. An analysis of a packed bed thermal energy storage system using sensible heat and phase change materials. **International Journal of Heat and Mass Transfer**, 118651, 2019.

Yogendrasasidhar, D., Setty, Y.P. Drying kinetics, exergy and energy analyses of Kodo millet grains and Fenugreek seeds using wall heated fluidized bed dryer. **Energy**, v.151, p.799-811, 2018.

Yu, X.L., Zielinska, M., Ju, H.Y., Mujumdar, A.S., Duan, X., Gao, Z.J., Xiao, H.W. Multistage relative humidity control strategy enhances energy and exergy efficiency of convective drying of carrot cubes. **International Journal of Heat and Mass Transfer**, v.149, 119231, 2020.

Yue, R., Zhang, Q. A pore-scale model for predicting resistance to airflow in bulk grain. **Biosystems Engineering**, v.155, p.142-151, 2017.

Zhang, H., Pang, B., Kang, S., Fu, J., Tang, P., Chang, J., Li, J., Deng, S. The influence of feedstock stacking shape on the drying performance of conveyor belt dryer. **Heat Mass Transfer**, 58, p.157–170, 2022.

Zoukit, A., Ferouali, H.E., Salhi, I., Soubabi, S., Doubabi, S., Abdenouri. Simulation, design and experimental performance evaluation of an innovative hybrid solar-gas dryer. **Energy**, v.189, 116279, 2019.

CHAPTER 2

HEAT TRANSFER IMPROVEMENT FOR A FILLED-TYPE COMPOUND PARABOLIC SOLAR COLLECTOR WITH U-TUBE: ENERGETIC AND ECONOMIC ANALYSIS

Abstract: The concentrated evacuated U-tube solar collector has enormous potential to meet the thermal energy demand of various processes. The use of filling materials in the evacuated tube is a simple, viable, and economical technique to improve the performance of this collector. However, for concentrated collectors, the use of this technique has been poorly investigated. In this study, the thermal and economic performance of a compound parabolic collector (CPC) with a U-tube was evaluated. Different filling fluids of the evacuated tube (water, air, and thermal oil) and different mass flowrates (0.007 kg s^{-1}, 0.009 kg s^{-1}, 0.014 kg s^{-1} and 0.021 kg s^{-1}) were evaluated. The optical analysis was performed using the ray tracing method (RTM) and the mean number of reflections method (ANR method). A detailed energy analysis for the different collector components was carried out. The overall thermal efficiency, thermal absorption efficiency and heat transfer efficiency of the collector were calculated. In addition, an economic analysis was also presented. The evaluated collector presented an optical efficiency of about 63.6%. The greatest gains in working fluid temperature (HTF) were observed for higher incidence of solar radiation. Among the filling fluids (FF) used, air reached the highest temperature inside the evacuated tube (160.6 ºC), followed by oil (84.6 ºC) and water (61.3 ºC). The increase in HTF mass flowrate resulted in a decrease in temperature gain. The use of thermal oil resulted in a higher average thermal efficiency (41.2%) compared to water (31.7%) and air (31.1%), achieved at the lowest flowrate. The collector configuration with the lowest mass flowrate of thermal oil as FF presented the best values of the economic indicators like leveled cost of heat (0.034 $ kWh^{-1}) and simple payback period (2.8 years).

Keywords: Evacuated U-tube solar collector. Experimental evaluation. Non-tracking CPC. Optical efficiency. Thermal efficiency.

Greek letters

γ	–	Diffuse solar radiation factor;
ρ	–	Reflectivity;
α	–	Absorbance of the receiver;
ε	–	Emittance of the receiver;
η	–	Efficiency, %;
φ	–	Polar angle, °;
θ	–	Half-angle, °;
τ	–	Transmittance of the receiver;

Symbols list

$\bar{T}$	–	Average temperature in the evaluated interval, ºC;
$\dot{m}$	–	Mass flow rate of the HTF, kg s^{-1};
A	–	Aperture, m / Area m^2;
c	–	Cost, \$ / \$ kWh^{-1};
C	–	Concentration ratio;
Cp	–	Specific heat, kJ kg^{-1} K^{-1};
CRF	–	Capital recovery factor;
D	–	Diameter, m;
E_{r-m}	–	Radiation exchange factor;
ET	–	Receiver type;
G	–	Incident global solar radiation, W m^{-2};
H	–	Height, m;
i	–	Interest rate, %;
I	–	Solar radiation intensity, W m^{-2};
L	–	CPC Length, m;
LCOH	–	Leveled cost of heat, \$ kWh^{-1};
m	–	Total mass inside the evacuated tube, kg;
N	–	Average number of reflections;
n	–	Useful life, years;
Q	–	Energy absorbed by the filling fluid, W;
r	–	Radius of the tubular absorber, m;
R	–	Uncertainty function;
SPP	–	Simple payback period, years;
t	–	Time, s;

T – Temperature, ºC;

U – Useful thermal energy, kWh m^{-2} $year^{-1}$;

W – Total uncertainty, %;

w – Uncertainties in the independent variables;

x – Independent variables;

Subscripts

a – Acceptance / aperture;

a,t – Acceptance (truncated);

as – Absorber surface;

c – Capital;

cp – Copper tube;

d – Diffuse;

EA – Annual;

elec – Electricity;

FF – Filling fluid;

FF,f – Filling fluid at the final time;

FF,i – Filling fluid at the initial time;

HT – Heat transfer;

HTF – Heat transfer fluid;

in – Inner / inlet;

max – Maximum;

n – Number of points;

o – Optical;

OEM – Leveled annual cost of operation and maintenance;

out – Outer / outlet;

r – Ratio;

r–m – between the absorber and the reflector ($\rho_r \rightarrow 1$);

rs – Reflective surface;

r,t – Ratio (truncated);

s – Incident solar;

t – Truncated;

T – Total;

TA – Thermal absorption;

u – Useful energy absorbed by the HTF;

0 – Width;

1. INTRODUCTION

Due to the energy-environmental scenario, the energy dependence of several sectors on conventional (fossil) fuels is gradually being replaced by renewable and sustainable energies. Among renewable sources, solar thermal energy is the most abundant, affordable and promising source to decarbonize residential and industrial heat demand (Chen and Yang, 2021). According to the Renewables Global Status Report (2022), the industrial sector and agriculture are responsible for about 31% of the world energy demand, in which, 83.9% is still supplied by non-renewable energy sources (REN21, 2022). A large part (about 60%) of the thermal energy consumed in the industrial sector is used to meet process heat applications at low and medium temperatures up to 250 °C (Sharma et al., 2017; Barbosa et al., 2020a). Solar collectors with high concentration rates can easily reach such temperatures. However, its use is related to limitations such as the high cost and complexity of the accurate solar tracking system.

The compound parabolic collector (CPC) is a low concentration solar collector. This collector consists of a non-tracking, non-image concentrator. Because it operates stationary, CPC is more attractive, affordable and popular for low to medium-temperature applications. In addition, the cost of heat generation per unit for this type of collector is considerably lower than observed for collectors with a tracking system (Kurhe et al., 2020). The evacuated glass tube (ET) generally used in these collectors is considered a key component in the use of solar thermal energy. The vacuum insulation and selective coating in these tubes reduce heat loss to the environment and contribute to better absorption of solar radiation (Olfian et al., 2021). Different techniques can be used to transfer the heat energy absorbed in the ET to the heat transfer fluid (HTF). The U-type tube is one of the most used due to its simple geometry, lower manufacturing cost, practical applicability and good efficiency. In this technique, a U-shaped tube is placed inside the ET, usually made of copper or other high-conductive metal, through which the HTF circulates (Naik et al., 2019).

Numerous theoretical and experimental approaches have been used to evaluate the performance of evacuated U-tube solar collectors over the years. Kim et al. (2017) evaluated the performance of an evacuated U-tube solar collector as a function of the size of the nanoparticles and the concentration of the nanofluid. The results indicated a 24.1% of increase in maximum efficiency with the use of nanofluid when compared to water. A numerical and experimental investigation of the performance of an array of evacuated U-tube solar collectors was carried out by Naik et al. (2019). The authors observed that series-connected tubes increase the fluid temperature at higher solar intensities. In some studies, the integration of CPC was

also evaluated. Li et al. (2013) compared two intermediate temperature CPC solar collectors with the U-shaped evacuated tubular absorber. The authors used theoretical models and experiments to evaluate the thermal performance and proved the feasibility of the collectors for medium-temperature applications. Korres and Tzivanidis (2019) numerically and experimentally investigated a CPC with an evacuated U-tube. The collector was tested at different angles of transverse and longitudinal incidence. The design proposed by the authors achieved an optical efficiency increase of 2.4%, considering a daily operation. A new seasonal dual-function asymmetric reflector for a CPC with an evacuated U-type tube was proposed by Chen and Yang (2021). The authors aimed to increase energy capture in winter and reduce overheating in summer. The average optical efficiencies achieved were 70% and 39% for winter and summer, respectively.

A key factor for improving the performance of these collectors is the heat transfer between the absorber evacuated tube and the U-tube, since the contact surface between these tubes is very small. In recent decades, many researchers have sought to improve this transfer using different approaches. Liang et al. (2011) used a high conductivity component (compressed graphite) as a filling material to eliminate the influence of thermal resistance between the evacuated tube and the U-tube. The authors achieved a thermal performance of up to 12% higher than the case without the filling material. Subsequently, the authors sought to increase the heat transfer area using an evacuated tube filled type with double U-tubes (Liang et al., 2013). The collector was evaluated theoretically and experimentally. The thermal efficiency of the proposed collector was about 4% higher when compared to the single U-tube collector in the same experimental condition. The use of phase change materials (PCM) was also investigated. Abokersh et al. (2017) evaluated an evacuated tube solar collector filled with PCM. The effectiveness of adding fins to the inner U-tube was also investigated. The non-finned collector obtained an efficiency 14% higher than the finned collector. However, the results showed that the addition of the fin helps to overcome the low thermal conductivity of the PCM during the discharge phase. Olfian et al. (2021) simulated the melting and solidification processes of PCM in an evacuated-tube solar collector with a U-shaped corrugated tube. It was observed that the corrugated tube increases the collector efficiency by 21.55% in relation to the smooth tube. In another approach, the increase in the contact area between the U-tube and the evacuated tube was experimentally evaluated by Essa et al. (2021). The authors used a unilateral helical U-tube in the collector, and its performance was compared with the traditional U-tube. For a flow rate of 10 L h^{-1}, using the helical U-tube provided a maximum increase in energy and exergy efficiency of 6.1% and 3.8%, respectively. On the

other hand, Chen and Yang (2022) simulated the improvement of heat transfer in the U-tube evacuated solar tube absorber by high-emissivity coating on the metal fin. CPC integration was also analyzed. It was found that the thermal efficiency was improved by 2.7% for the conventional U-tube case and by 8.4% for the CPC 6X case using the high-emissivity coating.

The concentrated evacuated U-tube solar collector has enormous potential to meet the thermal energy demand of various processes. The performance of this collector strongly depends on the heat transfer between the evacuated absorber tube and the U-tube. Over the years, different techniques have been used to improve this transfer. The use of filling materials in the evacuated tube is a simple, viable and economical technique as it does not require modification in the structure of the collector. However, there are still many gaps to be filled regarding the use of this technique. As evidenced in the literature review, this scenario is even more scarce in the case of experimental work and with the use of concentrated collectors. In this work, the influence of the use of different fluids to fill the evacuated tube on the thermal performance of a CPC with a U-tube was investigated. The collector was designed, built and evaluated experimentally. A detailed energy analysis for the different collector components is presented. In addition, the collector was also evaluated for four mass flowrates to determine the best operating condition. The results of this study will clarify how the use of filling fluids with different thermal properties affects the heat transfer rate in the absorber and the thermal and economic performance of the collector.

2. MATERIAL AND METHODS

2.1. Geometric modeling of the CPC

The CPC geometry has a parabolic section and an involute section around the receiver tube. The involute section is defined by the surface where the normal is tangent to the outer circumference of the receiver tube. The parabolic section is formed by two symmetrical parabolas that extend until their surfaces are parallel to the vertical axis. A schematic of the geometric profile of the CPC, showing its main parameters, is presented in Fig.1.

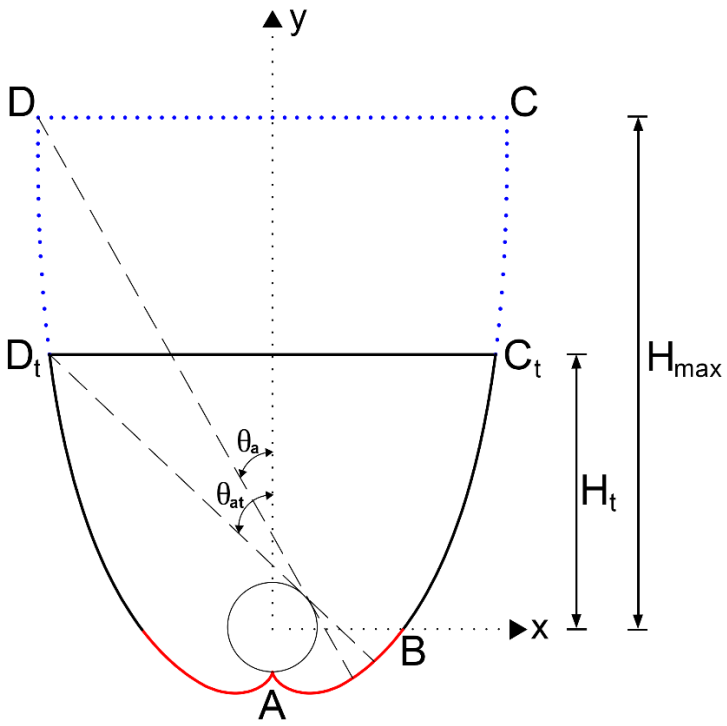

Fig. 1. Schematic diagram of a CPC collector.

A set of first-order differential equations, dependent on the angular coordinate, determines the design of the reflector sections. Cartesian coordinates in the xy-plane are defined by Eqs. 1 and 2 for the AB segment (involute section) and by Eqs. 3 and 4 for the BC segment (parabolic section, Ralb et al., 1979). The variable 'M' depends on the acceptance angle (θ) and can be calculated by Eq. 5. Equations 1 and 2 are used at the limit where $0 \leq \varphi \leq \frac{\pi}{2} + \theta_a$ (involute section), while Eqs. 3 and 4 are used for $\frac{\pi}{2} + \theta_a \leq \varphi \leq \frac{3\pi}{2} - \theta_a$ (parabolic section).

$$x = r(\sin\varphi - \varphi\cos\varphi) \tag{1}$$

$$y = -r(\varphi\sin\varphi + \cos\varphi) \tag{2}$$

$$x = r(\sin\varphi - M\cos\varphi) \tag{3}$$

$$y = -r(M\sin\varphi + \cos\varphi) \tag{4}$$

$$M = \frac{\left(\frac{\pi}{2} + \theta_a + \varphi - \cos(\varphi - \theta_a)\right)}{(1 + \sin(\varphi - \theta_a))} \tag{5}$$

The geometric concentration ratio (C_r) is an important parameter in solar thermal systems and is related to the concentration degree of the solar collector. This parameter can be expressed as a function of the acceptance angle for a CPC, as shown in Eq. 6 (Ralb, 1985). In practice, C_r is commonly approximated as the ratio of the aperture area to the surface area of the absorber (Eq. 7).

$$C_r = \frac{1}{sin\,\theta} \tag{6}$$

$$C_r = \frac{A_a}{A_{as}} = \frac{A_0}{2\,\pi\,r} \tag{7}$$

The upper ends of the reflectors near the aperture have a smaller curvature, being almost parallel to the vertical axis of the collector, which results in a very limited concentration of radiation. In practice, these ends are usually truncated as they do not have much influence on the concentration ratio. Ustaoglu et al. (2016) showed that for a truncation ratio of 47%, a reduction of only 2% was observed for the average CPC thermal efficiency. Thus, to achieve a more economical design, the original geometry of the CPC was truncated in this study. The geometric parameters and specifications of the CPC are presented in Table 1.

Table 1. CPC geometric parameters and technical specifications

Parameter	**Symbol**	**Value**	**Unit**
CPC Length	L	1.700	m
Aperture width	A_0	0.281	m
Maximum height	H_{max}	0.320	m
Truncated height	H_t	0.180	m
Acceptance half-angle	θ_a	30	º
Acceptance half-angle (truncated)	$\theta_{a,t}$	31.7	º
Concentration ratio	C_r	2.0	-
Concentration ratio (truncated)	$C_{r,t}$	1.9	-
Receiver Characteristics			
Receiver type	ET	Evacuated glass tube	-
Copper tube diameter	D_{cp}	0.009	m
Outer diameter	D_{out}	0.058	m
Inner diameter	D_{in}	0.047	m
Length	L_r	1.800	m
Absorbance	α	0.930 - 0.960	-
Emittance	ε	0.050	-
Transmittance	τ	0.950	-
Vacuum rate	-	0.005	Pa

2.2. CPC and TES construction

The CPC structure was built from a wooden frame following the geometric format shown in Fig.1 and calculated according to Eqs. 1 to 5. The constructed CPC is composed of four sets of parabolic reflectors (Figure 2). The reflective surface consisted of a high-reflectance stainless steel plate (ρ> 86%) that was fixed to the wooden parabolic structure. An evacuated glass tube was placed in the central focus of each reflector assembly, totaling four tubes. The evacuated tube consists of two layers of glass with a vacuum in its annular space and a selective coating of high absorbance and low emittance on the inner surface of the glass tube. Inside each evacuated glass tube, a U-shaped copper tube was inserted for the HTF flow. The dimensions of the copper tube were 3/8” in diameter, 3.4 meters in unit length and 2 millimeters thick. The

U-shaped copper tubes were connected in series using brass fittings. Sealing rubbers were used on each evacuated tube to prevent leakage.

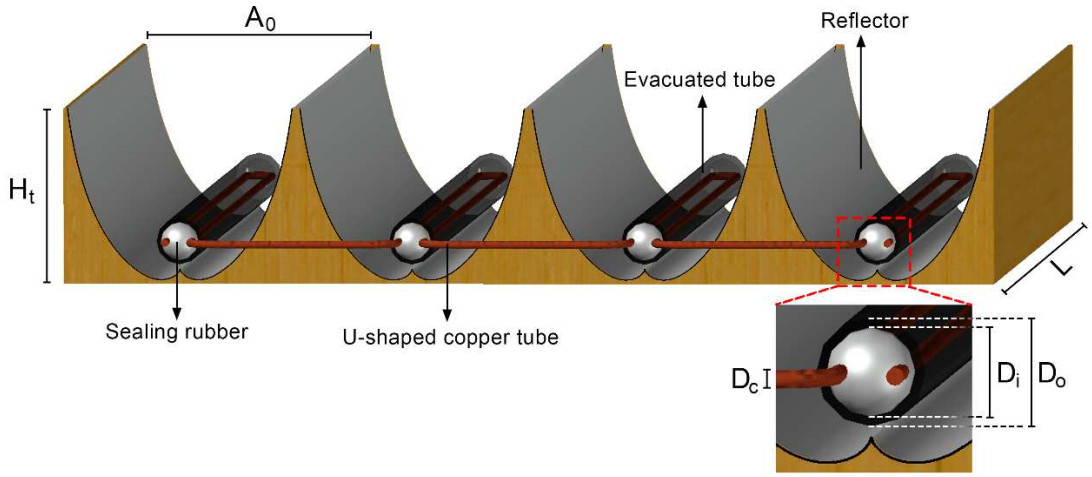

Fig. 2. Detailed schematic of CPC components.

Two storage reservoirs were used: one for the hot fluid and one for the cold fluid. The hot and cold metallic reservoirs had a volume of 80 and 200 liters, respectively. The hot reservoir was insulated by a 40 mm thick layer of glass wool to minimize thermal exchange with the environment. A 3.0 mm thick aluminum blanket was used as the last layer of enveloping to protect the reservoirs from the weather. Brass connections were welded to the top and bottom of the reservoirs to allow the coupling to the copper tube.

2.3. Experimental setup and procedure

The CPC was evaluated under Brazilian environmental conditions, specifically located at coordinates 20°45′00″S, 42°56′15″W and at an altitude of 643 m. The collector was installed facing north with an inclination angle of 20.75º (local latitude). The CPC was evaluated by operating stationary and in a closed circuit with forced convection regime for the HTF. As depicted in Fig. 3, the experimental setup consists of the following main components: CPC, HTF circulation pump, frequency inverter for flow control, hot and cold storage reservoirs, and data acquisition system. During its operation, the reflectors concentrate the solar radiation received in their aperture area in the evacuated glass tube placed in the center of the parabola. The evacuated glass tube absorbs this energy and transfers it to the inside U-shaped copper tube. An HTF is pumped into the U-shaped copper tube, absorbing the thermal energy of the CPC. This energy is then stored in the hot reservoir.

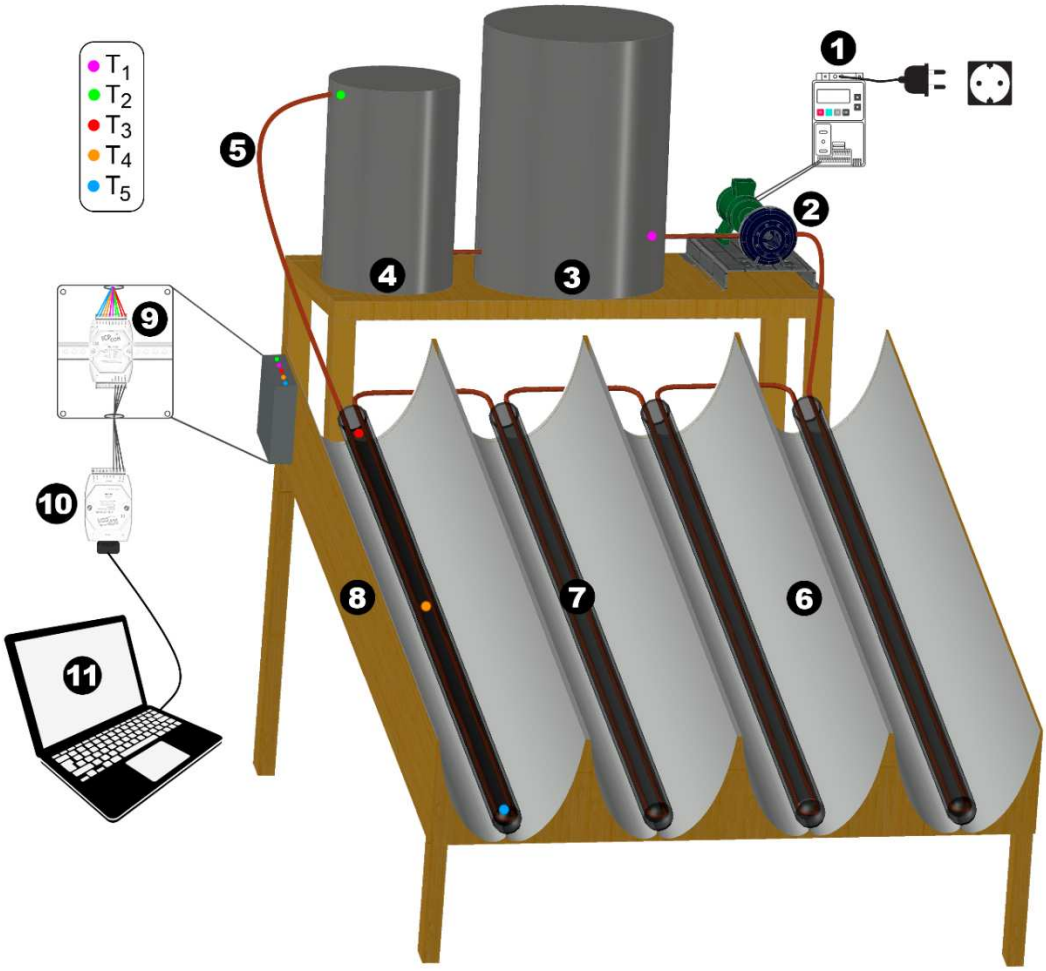

Fig. 3. Detailed schematic of the experimental setup: (1) frequency inverter; (2) pump; (3) cold reservoir; (4) hot reservoir; (5) copper tube; (6) CPC; (7) evacuated glass tube; (8) wooden support structure; (9) data acquisition module; (10) data conversion module; (11) computer and thermocouples (T_1, T_2, T_3, T_4 e T_5).

The experiments were carried out from January to March, which corresponds to the summer season in Brazil. Temperature data were collected at different CPC positions and thermal reservoirs using type K thermocouples (Omega, Accuracy: ± 0.1°C). The thermocouples were positioned in the lower part of the cold reservoir (inlet temperature) and the upper part of the hot reservoir (outlet temperature). In addition, to collect the filling fluid temperature (FF) data, three thermocouples were used at the top, middle and bottom of a manifold evacuated tube. Temperature data were collected and stored every 30 seconds by data acquisition and conversion modules connected to a computer (Fig. 3). The global solar radiation, ambient temperature and wind speed data were provided by the meteorological

station of the National Institute of Meteorology (INMET), located on the campus of the Federal University of Viçosa.

In this study, water was used as HTF pumped into U-shaped copper tubes. The experiments were carried out in two stages. In the first step, it was investigated the influence of different filling fluids in the evacuated tube on the heat transfer from the collector. At this step, the experimental trials were performed at a fixed mass flowrate of 0.007 kg s^{-1} ($\dot{m}1$). The filling fluids evaluated were water (W-$FF_{\dot{m}1}$), air (A-$FF_{\dot{m}1}$), and thermal oil (O-$FF_{\dot{m}1}$). In the second step, the effect of using different mass flowrates on CPC performance was studied. Thermal oil was used as a filling fluid in all evaluations performed at this step. The mass flowrates used were 0.007 kg s^{-1}, 0.009 kg s^{-1}, 0.014 kg s^{-1} and 0.021 kg s^{-1}, named as O-$FF_{\dot{m}1}$, O-$FF_{\dot{m}2}$, O-$FF_{\dot{m}3}$ and O-$FF_{\dot{m}4}$, respectively. Figure 4 shows a summary of the experimental steps and their characteristics.

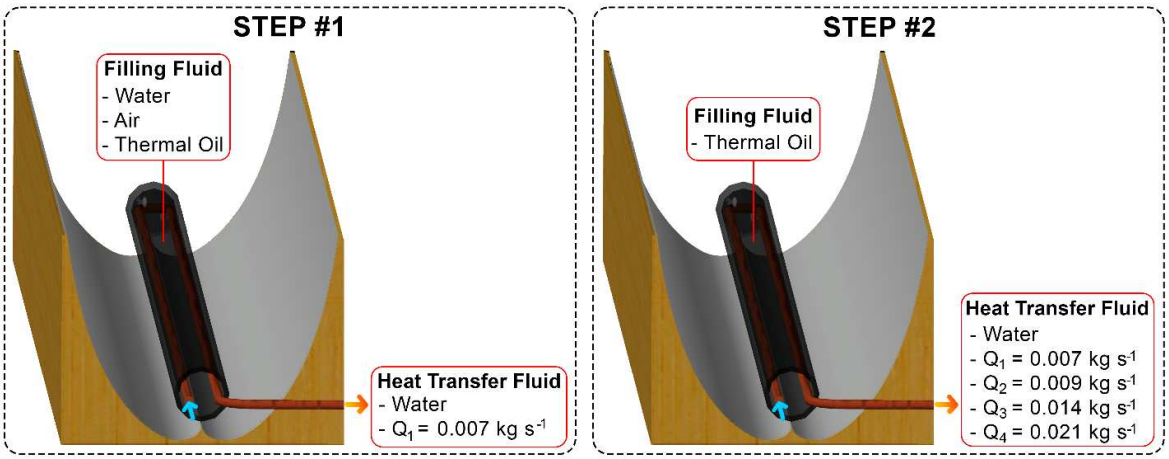

Fig. 4. Scheme of evaluated experimental steps.

2.4. Analytical procedures

2.4.1. Uncertainty analysis

Uncertainty analysis was performed to assess the reliability and validity of the calculated experimental results. In this study, the uncertainty analysis (Eq. 8) was performed as described by Moffat, (1985).

$$W_R = \left[\left(\frac{\partial R}{\partial x_1} w_1\right)^2 + \left(\frac{\partial R}{\partial x_2} w_2\right)^2 + \cdots\cdots + \left(\frac{\partial R}{\partial x_n} w_n\right)^2\right]^{1/2} \quad (8)$$

2.4.2. Optical efficiency

Optical efficiency represents the maximum theoretical fraction that can be converted to heat. The higher its value, the greater the amount of sunlight reaching the aperture area is effectively being reflected to the absorber tube. In this study, optical analysis was performed using both the ray tracing method (RTM) and the mean number of reflections method (ANR method). The analyzes were carried out considering different angles of incidence of solar radiation, aiming to determine the daily optical performance of the system. For the RTM, the analyzes were performed using ray tracing software (TracePro). To simulate solar radiation from the semi-space above the collector plane, 100,000 light sources were randomly distributed along the collector aperture. Incident rays interact on surfaces and are divided into reflected, transmitted, and absorbed parts. From the data on the fraction of rays that strike the absorber, an optical efficiency value can be calculated for a given angle of incidence (Li et al., 2013). The properties (reflectivity, absorptivity, and transmissivity) of the reflector and the absorber were defined according to the values described in the previous sections.

For theoretical optical analysis, the average number of reflections method (ANR method) was used, which is an approximation method proposed by Rabl (1977). The ANR method provides an approximation of the radiation that is transmitted through a specular passage. This is a simple and efficient method for obtaining optical efficiency in low concentration systems. Optical efficiency was calculated using Eq. 9.

$$\eta_o = \tau\, \alpha \rho_{rs}^{\langle N \rangle} \gamma \tag{9}$$

The average number of reflections N can be determined by Eq. 10. For the specific CPC experimental model, N was calculated by Eqs. 11 to 13, as presented by Carvalho et al. (1985). The diffuse solar radiation factor (γ), defined in Eq. 14, was calculated using an approximate relationship by Rabl et al. (1980) for the case of collectors with a small concentration ratio (C). For an average clarity index, the diffuse and total solar radiation intensity (I_d) can be considered as $I_d = 0.2\ I_t$ (Collares-Pereira and Rabl, 1979).

$$\langle N \rangle = \frac{A_{rs}}{A_{as}} E_{r-m} \tag{10}$$

$$\langle N \rangle = \frac{\left(\theta_a + \frac{\pi}{2}\right)^2}{4\pi} + \frac{\sqrt{2}}{2\pi}\int_{\theta_a+\frac{\pi}{2}}^{\frac{3\pi}{2}-\theta_a} \frac{a\ b}{[1\ +\ \sin(\theta\ -\theta_a)]^{\frac{3}{2}}} d\theta \quad (11)$$

$$a = \theta_a + \frac{\pi}{2} + \theta\ -\ \cos(\theta\ -\theta_a\ ) \quad (12)$$

$$b = 1\ -\ \sin\left(\frac{\theta\ -\theta_a - \frac{\pi}{2}}{2}\right) \quad (13)$$

$$\gamma = 1 - \left(1 - \frac{1}{C}\right)\left(\frac{I_d}{I_t}\right) \quad (14)$$

2.4.3. Thermal performance

2.4.3.1. Overall CPC efficiency

The instantaneous thermal efficiency (η) is one of the most important parameters of the energy performance of a solar collector. This parameter is defined as the ratio between the useful energy absorbed (Q_u) by the HTF and the incident solar energy (Q_s) in the collector aperture area (Eqs. 15 and 16).

$$\eta\ = \frac{Q_u}{Q_s} \quad (15)$$

$$\eta\ = \frac{\dot{m}\ Cp_{HTF}\ (T_{out} - T_{in})}{A_{ap}\ G} \quad (16)$$

2.4.3.2. Thermal absorption efficiency

In this study, the thermal absorption efficiency (η_{TA}) was calculated as described in Eqs. 17 to 19. This efficiency is defined as the ratio between the total energy absorbed by the CPC, in other words, the energy absorbed by the FF and the HTF, and the incident solar energy (Qs) in the collector aperture area.

$$\eta_{TA}\ = \frac{Q_{HTF}\ + Q_{FF}}{Q_s} \quad (17)$$

$$Q_{HTF}\ = \left(\dot{m}\ Cp_{HTF}\ (T_{out} - T_{in})\right) \quad (18)$$

$$Q_{FF} = \frac{m_{FF}}{t} Cp_{FF}\left(T_{FF,f} - T_{FF,i}\right) \quad (19)$$

2.4.3.3. Heat transfer efficiency

Heat transfer efficiency (η_{HT}) is defined as the ratio between the total energy absorbed by the HTF and the total energy available in the FF (Eqs. 20 and 21). This parameter measures how efficient the heat transfer is between the FF and the HTF pumped through the U-shaped copper tube, that is, how much of the energy absorbed by the FF was effectively converted into useful energy by the HTF.

$$\eta_{HT} = \frac{Q_{HTF}}{\bar{Q}_{FF}} \quad (20)$$

$$\bar{Q}_{FF} = \left(\frac{m_{FF}}{t} Cp_{FF}\, \bar{T}_{FF}\right) \quad (21)$$

2.4.4. Economic analysis

The leveled cost of heat (LCOH) indicator is an economic valuation model widely used in the heating and solar thermal industries (Huang et al., 2019). This parameter indicates the average amount paid for each heating unit produced by the collector over its lifetime. The LCOH of the proposed system was calculated as described in Eqs. 22 and 23. The cost of capital (c_c) was calculated considering the total cost required to manufacture the CPC. The leveled annual cost of operation and maintenance (c_{OEM}) is estimated to be \$5 m^{-2} (Bhusal et al., 2020). The number of years of operation over the useful life (n) and the interest rate (i) were assumed to be 25 years and 6%, respectively (Zare and Moalemian, 2017). The average annual solar irradiance (I_S) in the region is 1846 kWh m^{-2} $year^{-1}$ (Pereira et al., 2017). Simple payback period (SPP) is a metric used to assess the viability of the investment. The SPP can be defined as the time required for the savings generated by the CPC to equal the total initial investment, which is the payback period. Equation 24 was used to calculate the SPP (Barbosa et al., 2020b). The cost of electricity (c_{elec}) is 0.1248 \$ kWh^{-1} (CEMIG, 2022).

$$LCOH = \frac{(CRF\, c_C) + c_{OEM}}{U_{EA}} \quad (22)$$

$$CRF = \frac{i\,(1+\,i)^n}{(1+\,i)^n\,-1} \tag{23}$$

$$SPP\, = \frac{c_C\, +\, c_{OEM}}{U_{EA}\, c_{elec}} \tag{24}$$

3. RESULTS AND DISCUSSION

The experimental data obtained and the results of the energy and economic evaluation of the CPC for the different filling fluids and mass flowrates evaluated are presented and discussed in detail in this section.

3.1. Summary data

3.1.1. Meteorological data

Figure 5 shows solar radiation, wind speed and ambient temperature data for the evaluated cases. It can be observed that, for all evaluated days, the solar radiation showed typical behavior of a clear day, with a continuous increase until 12:00-13:00 h and decreasing in the subsequent hours. The maximum values of solar radiation observed were 978.6 W m^{-2}, 969.7 W m^{-2}, 995.9 W m^{-2}, 962.9 W m^{-2}, 989.4 W m^{-2} and 979.5 W m^{-2} for the cases W-$FF_{\dot{m}1}$, A-$FF_{\dot{m}1}$, O-$FF_{\dot{m}1}$, O-$FF_{\dot{m}2}$, O-$FF_{\dot{m}3}$ and O-$FF_{\dot{m}4}$, respectively. The ambient temperature increases continuously throughout the day, until reaching its maximum value at 17:00 hours, while the wind speed showed a random behavior over the evaluated days. The average values of ambient temperature and wind speed on the evaluated days were 26.3 ºC and 1.7 m s^{-1} for the W-$FF_{\dot{m}1}$, 25.6 ºC and 2.0 m s^{-1} for the A-$FF_{\dot{m}1}$, 25.4 ºC and 2.2 m s^{-1} for the O-$FF_{\dot{m}1}$, 25.8 ºC and 1.9 m s^{-1} for the O-$FF_{\dot{m}2}$, 25.7 ºC and 1.8 m s^{-1} for the O-$FF_{\dot{m}3}$, and 25.6 ºC and 1.8 m s^{-1} for the O-$FF_{\dot{m}4}$. These data are representative of meteorological conditions typically observed in Brazil.

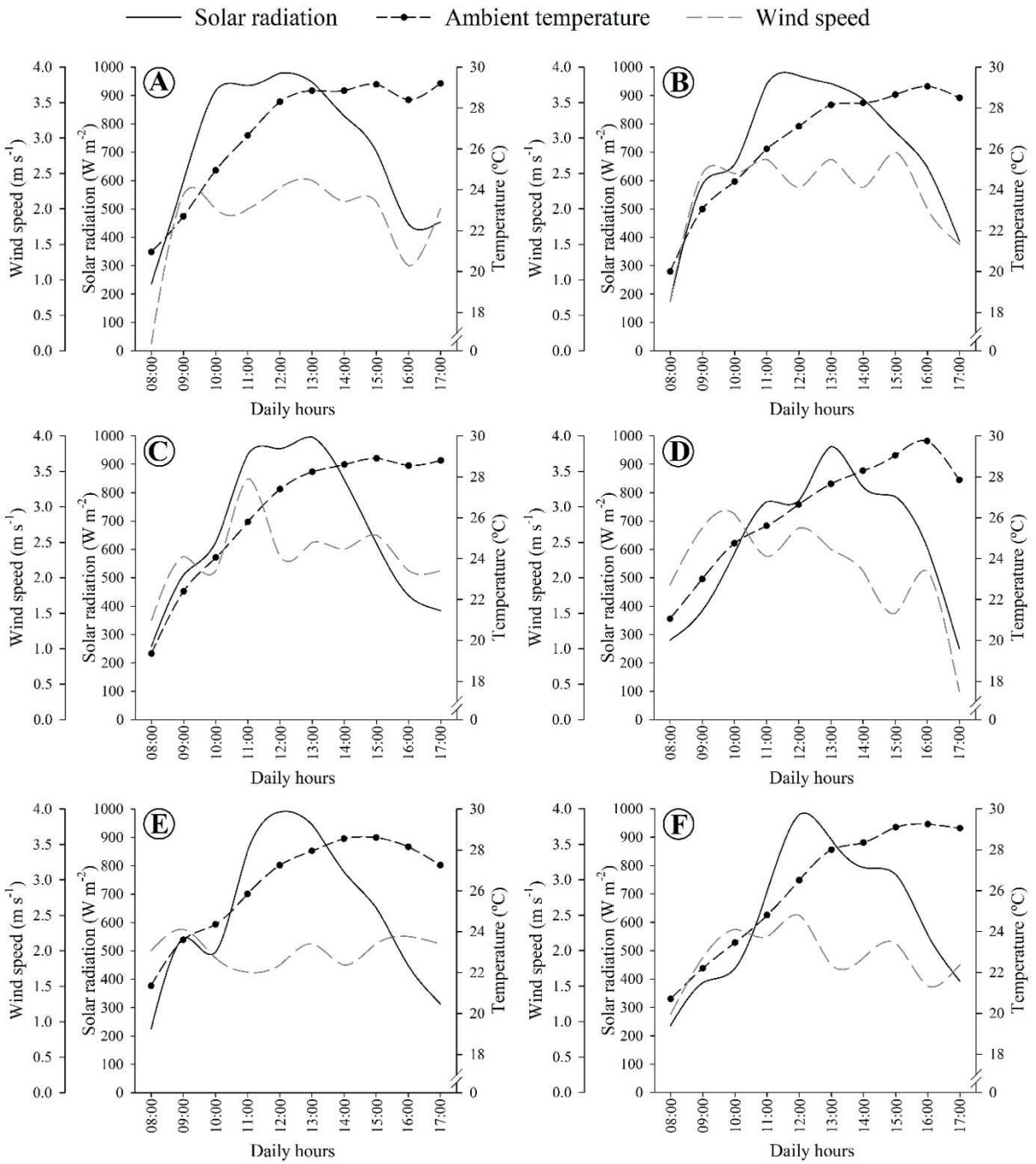

Fig. 5. Variation of solar radiation, ambient temperature, and wind speed for (A) W-$FF_{\dot{m}1}$; (B) A-$FF_{\dot{m}1}$; (C) O-$FF_{\dot{m}1}$; (D) O-$FF_{\dot{m}2}$; (E) O-$FF_{\dot{m}3}$ and (F) O-$FF_{\dot{m}4}$.

3.1.2. Experimental data

The water inlet and outlet temperature (HTF) data and the average temperature of the different filling fluids for the first stage of experiments are shown in Fig. 6. Both temperatures for all evaluated FF follow the same behavior of solar radiation over the hours, since these parameters are directly related. For all cases evaluated, the highest temperature gains ($\Delta T=T_{out}$

-T_{in}) were obtained between 12:00 and 13:00 h: 28.1 ºC for the W-$FF_{\dot{m}1}$, 30.2 ºC and for the A-$FF_{\dot{m}1}$ and 33.1 ºC for the O-$FF_{\dot{m}1}$. At these time intervals, the highest values of incident solar radiation are observed in the collector aperture area. Thus, a greater amount of energy is concentrated in the evacuated tube, favoring the condition of thermal absorption by the HTF. Similarly, at these times the highest values of average temperatures of the FF are also observed as 61.3 ºC, 160.6 ºC and 84.6 ºC for the cases W-$FF_{\dot{m}1}$, A-$FF_{\dot{m}1}$ and O-$FF_{\dot{m}1}$, respectively. In fact, the increase in the average temperature of the FF over the hours is more pronounced for the air, followed by the thermal oil. This may be related to the lower volumetric heat capacity of these fluids when compared to water.

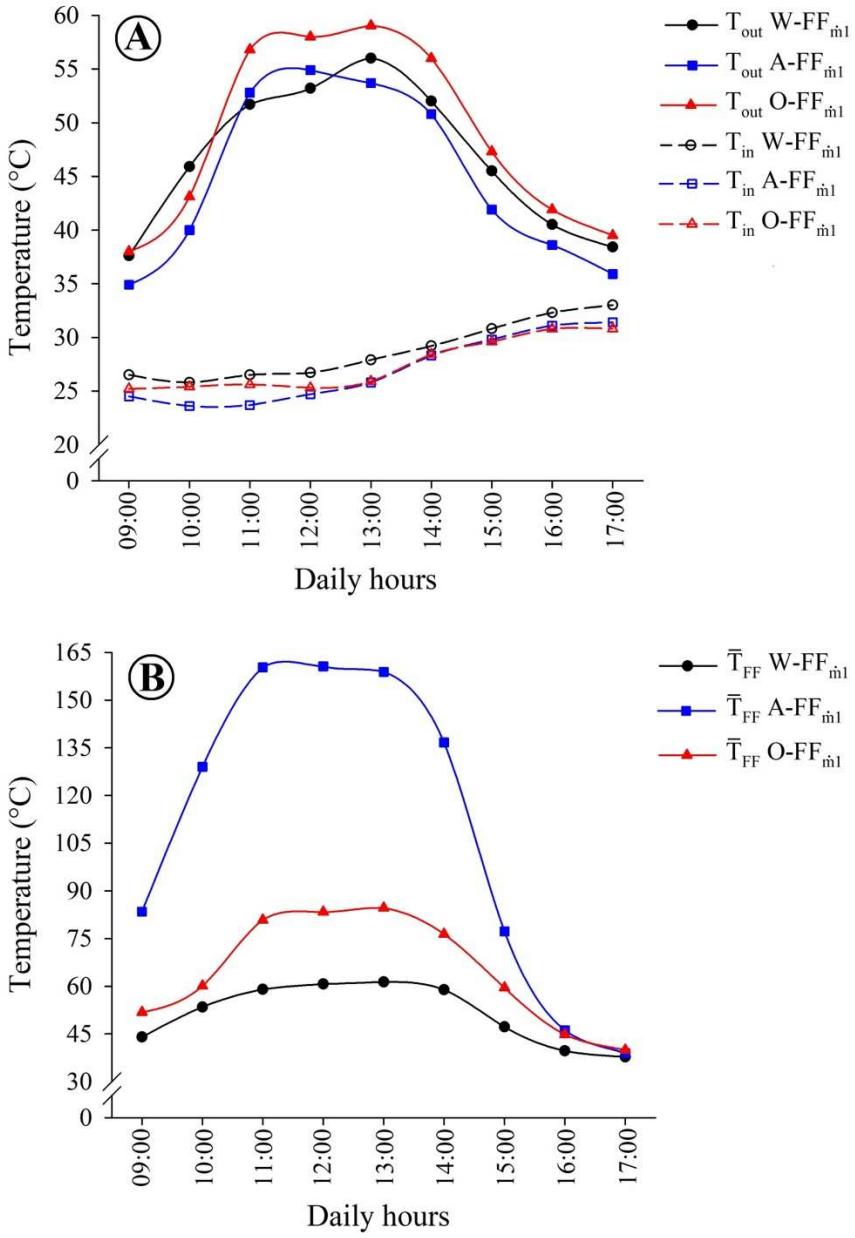

Fig. 6. Temperature variation over the hours for the cases W-$FF_{\dot{m}1}$, A-$FF_{\dot{m}1}$ and O-$FF_{\dot{m}1}$: (A) inlet and outlet temperature and (B) average temperature of the filling fluid.

Figure 7 shows the water inlet and outlet temperature data (HTF) and the average temperatures of the filling fluid (thermal oil) for the different mass flowrates evaluated. As observed, the temperature gains increase continuously until reaching their maximum value between 12:00 and 13:00 h and decrease in the hours of lower solar incidence. The highest values of temperature gain observed were 33.1 ºC for the O-$FF_{\dot{m}1}$, 17.1 ºC for the O-$FF_{\dot{m}2}$, 12.2 ºC for the O-$FF_{\dot{m}3}$ and 9.2 ºC for the O-$FF_{\dot{m}4}$. There is also a greater increase in the inlet temperatures for the cases O-$FF_{\dot{m}2}$, O-$FF_{\dot{m}3}$ and O-$FF_{\dot{m}4}$ from 13:00 hours. Indeed, the greater the mass flowrate, the greater the total amount of heated HTF that flows to the cold reservoir, since the CPC operates in a closed circulation system. The average temperatures of the FF reach closer values at times of lower solar incidence and higher mass flowrates. A significant temperature rise is observed between 11:00 and 14:00 h for the case O-$FF_{\dot{m}1}$. The highest values observed were 84.6 ºC, 76.5 ºC, 74.3 ºC and 74.5ºC for O-$FF_{\dot{m}1}$, O-$FF_{\dot{m}2}$, O-$FF_{\dot{m}3}$ and O-$FF_{\dot{m}4}$, respectively.

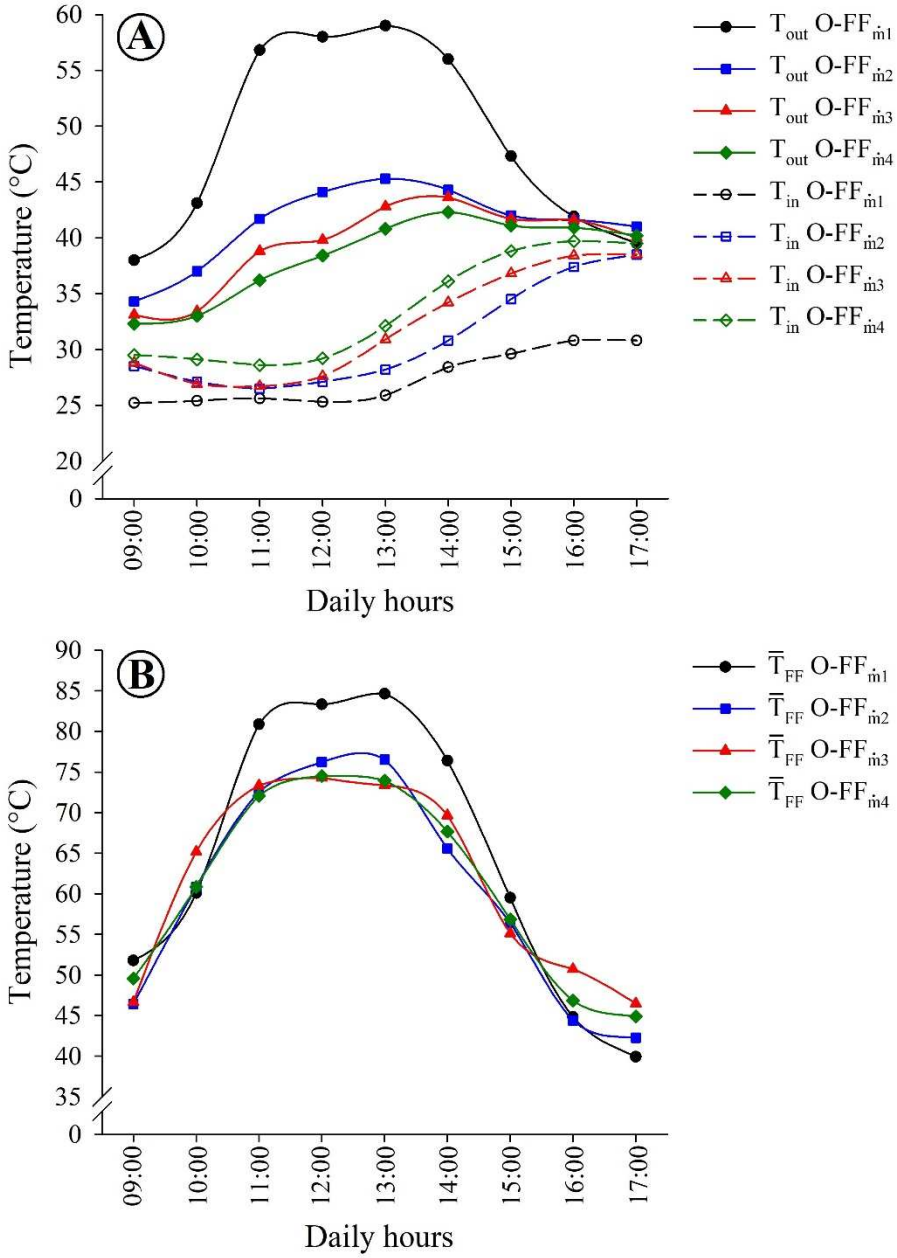

Fig. 7. Temperature variation over the hours for the cases O-FF$_{\dot{m}1}$, O-FF$_{\dot{m}2}$, O-FF$_{\dot{m}3}$ and O-FF$_{\dot{m}4}$: (A) inlet and outlet temperature and (B) average temperature of the filling fluid.

3.2. Optical efficiency

Figure 8 shows the variation in the optical efficiency of the collector as a function of the angle of incidence by the RTM and ANR methods. The optical efficiencies remain almost constant within the half-acceptance angle of the CPC (-30º to +30º) and decrease rapidly for angles outside this range. It should be noted that outside the acceptance angle the optical efficiency is not zero, as the collector continues to collect the radiation incident directly on the absorber and some rays focuses on the near side of the concentrator. It is observed that the

efficiencies obtained by both methods were very close. The average values of optical efficiencies obtained within the collector acceptance limits were 63.8 and 63.6% by the RTM and ANR method, respectively. These efficiencies are close to the optical efficiencies generally found for this type of collector (Osório et al., 2019; Bhusal et al., 2020; Kurhe et al., 2020).

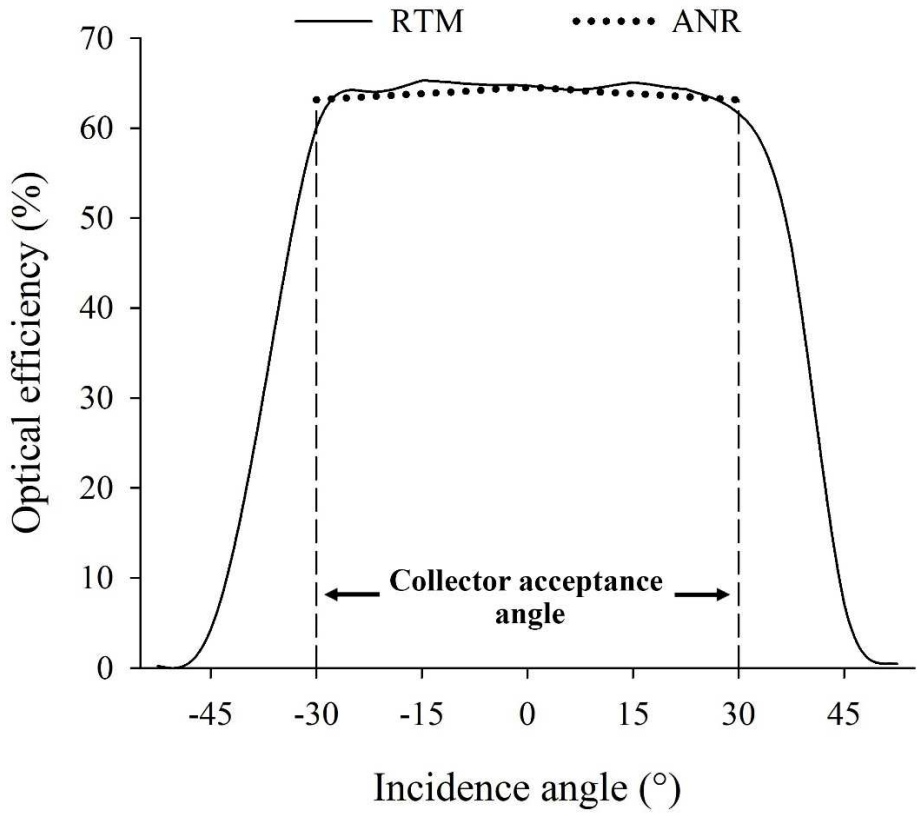

Fig. 8. Optical efficiencies of the CPC as a function of the angle of solar incidence for the RTM and ANR methods.

3.3. Thermal analysis

3.3.1. Overall CPC efficiency

The hourly thermal efficiencies of the CPC for the different FF evaluated in this study are shown in Fig. 9. The highest thermal efficiency values are observed between 11:00 and 13:00 h for all cases. Thermal oil (O-$FF_{\dot{m}1}$) provided a better thermal performance of the CPC, presenting higher values of efficiency in all the hours evaluated. The efficiencies of A-$FF_{\dot{m}1}$ exceed those of W-$FF_{\dot{m}1}$ until 13:00 h, an opposite behavior is observed in the subsequent hours. The average and maximum values of thermal efficiency obtained were 31.7% and 41.8% for the W-$FF_{\dot{m}1}$, 31.1% and 43.8% for the A-$FF_{\dot{m}1}$ and 41.2% and 48.2% for the O-$FF_{\dot{m}1}$,

respectively. It is also verified that the difference between the efficiencies obtained for the evaluated cases, reduces at times of higher solar incidence and increases at times when the incidence is lower. At 17:00 hours, while the thermal efficiency of the O-FF$_{\dot{m}1}$ is about 31.9%, the efficiencies of W-FF$_{\dot{m}1}$ and A-FF$_{\dot{m}1}$ do not exceed 16.7% and 16.4%, respectively. These findings unequivocally establish that the choice of FF in the evacuated tube exerts a substantial influence on the performance of the CPC.

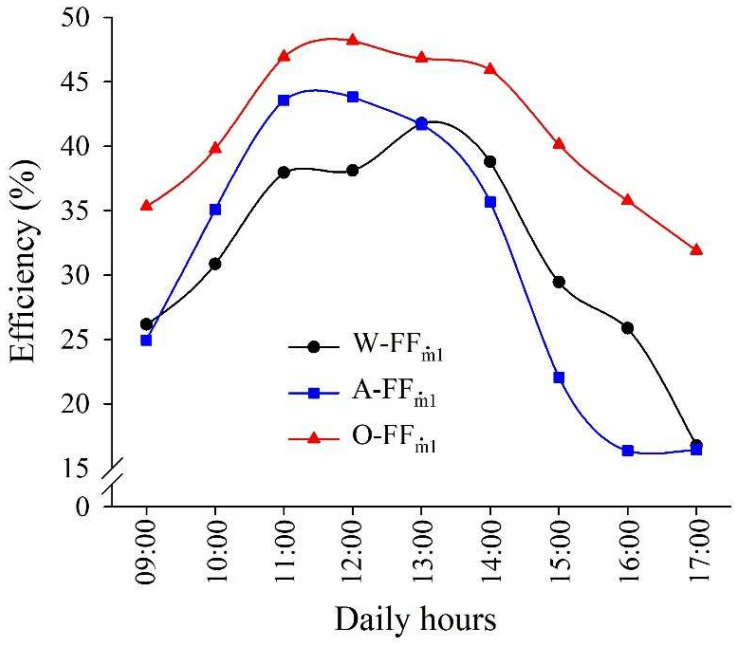

Fig. 9. Thermal efficiencies of the CPC over the hours for the different filling fluids evaluated.

The increase in flow causes a reduction in the efficiency values in almost all hours evaluated (Figure 10). The best thermal performance is verified for the lowest mass flowrate (O-FF$_{\dot{m}1}$). The average values of thermal efficiency found were 41.2% for the O-FF$_{\dot{m}1}$, 27.0% for the O-FF$_{\dot{m}2}$, 27.7% for O-FF$_{\dot{m}3}$, and 26.3% for the O-FF$_{\dot{m}4}$. It is also verified that from 14:00 onwards, there is a successive reduction in the efficiency values for all cases. This behavior is related to the considerable temperature increase experienced by the fluid into the evacuated tube during the hours of highest solar incidence (11:00 to 13:00 h). This increases the temperature difference between the FF and the environment, resulting in higher thermal losses. Furthermore, after 13:00 h, there is a decline in solar radiation, leading to a decrease in the energy accessible within the collector aperture area.

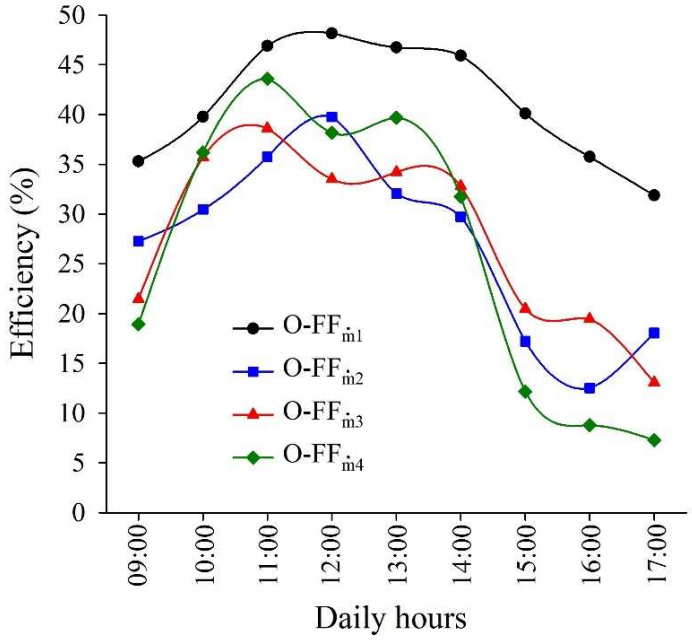

Fig. 10. Thermal efficiencies of the CPC over the hours for the different mass flowrates evaluated.

3.3.2. Thermal absorption and heat transfer efficiencies

The available solar energy (Q_S), the useful energy absorbed by the HTF (Q_{HTF}) and the energy absorbed by the FF (Q_{FF}) for cases W-FF$_{\dot{m}1}$, A-FF$_{\dot{m}1}$ and O-FF$_{\dot{m}1}$ achieve maximum values near 12:00 h, as expected. The Q_{HTF} and Q_{FF} values varied between 161.46 – 840.19 W and 548.07 – 890.86 W for the W-FF$_{\dot{m}1}$, 134.55 – 902.98 W and 0.32 – 1.32 W for the A-FF$_{\dot{m}1}$ and 260.13 – 989.69 W and 247.40 – 524.33 W for the O-FF$_{\dot{m}1}$, respectively. For W-FF$_{\dot{m}1}$, Q_{FF} surpasses Q_{HTF} in all hours evaluated, the opposite is observed for A-FF$_{\dot{m}1}$ and O-FF$_{\dot{m}1}$. The lowest Q_{FF} values observed for the A-FF$_{\dot{m}1}$ are related to lower air density than the others FF, since the volume of the evacuated tube is the same. It is observed that, in the hours of lower solar incidence, the O-FF$_{\dot{m}1}$ presents a smaller difference between the Q_{HTF} and Q_{FF} values than the other cases. This same behavior is observed for the W-FF$_{\dot{m}1}$ in the times of greatest radiation.

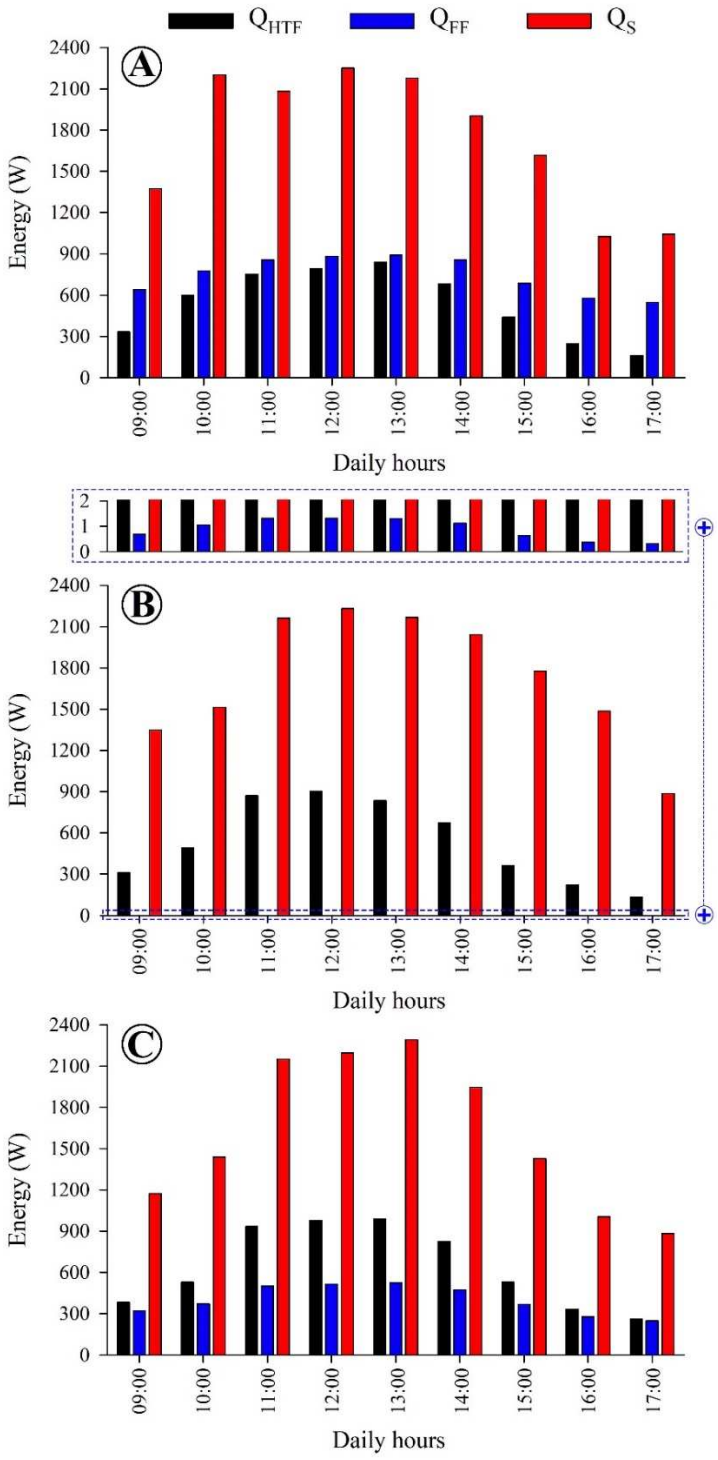

Fig. 11. Hourly variation of available solar energy (Q_S), useful energy absorbed by HTF (Q_{HTF}) and energy absorbed by FF (Q_{FF}) for (A) W-$FF_{\dot{m}1}$; (B) A-$FF_{\dot{m}1}$ and (C) O-$FF_{\dot{m}1}$.

Figure 12 shows the hourly variation of thermal absorption efficiency (η_{TA}) and heat transfer efficiency (η_{HT}) for W-$FF_{\dot{m}1}$, A-$FF_{\dot{m}1}$ and O-$FF_{\dot{m}1}$. The heat transfer efficiency exceeds the thermal absorption efficiency in all the hours evaluated. In addition, η_{TA} presents a greater hourly variation than η_{HT}, because it is directly related to solar radiation. Therefore, the thermal

oil as FF engenders a more efficient state for the absorption of solar radiation. The average values of η_{TA} found for W-$FF_{\dot{m}1}$, A-$FF_{\dot{m}1}$ e O-$FF_{\dot{m}1}$ were 28.6%, 28.7% and 37.6%, respectively. Considering η_{HT}, the case that presented the highest efficiency values was A-$FF_{\dot{m}1}$ with an average of 99.8%, followed by O-$FF_{\dot{m}1}$ with 59.7% and the W-$FF_{\dot{m}1}$ with 39.6%. Among the evaluated FF, the air has the lowest volumetric heat capacity, and thus reaches the highest temperature (Fig. 6B). The HTF flows into the U-tube at a low temperature and exchanges heat with the high-temperature air within the evacuated tube.

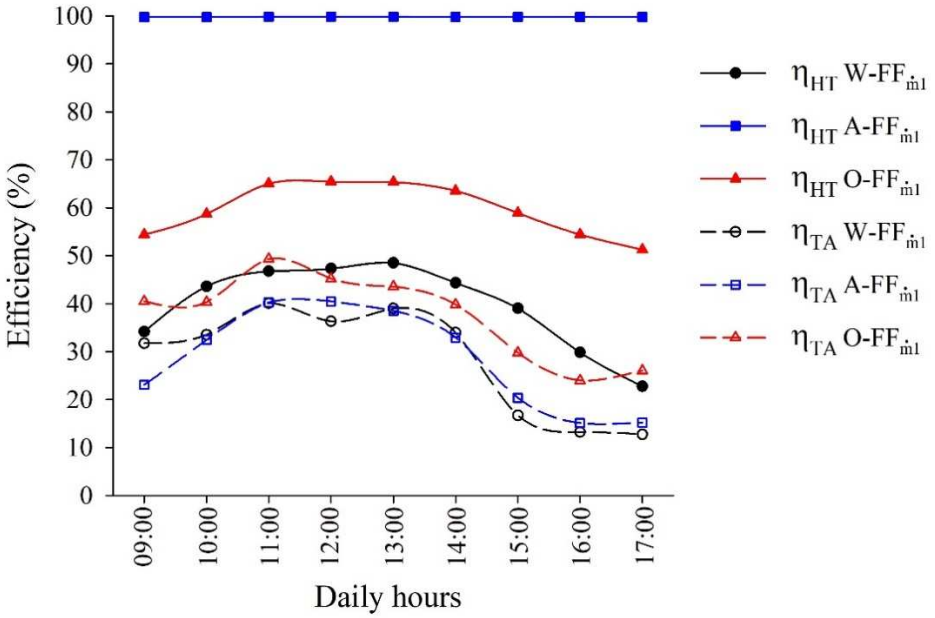

Fig. 12. Hourly variation of thermal absorption efficiency (η_{TA}) and heat transfer efficiency (η_{HT}) for W-$FF_{\dot{m}1}$, A-$FF_{\dot{m}1}$ and O-$FF_{\dot{m}1}$.

The available solar energy (Q_S), the useful energy absorbed by the HTF (Q_{HTF}) and the energy absorbed by the FF (Q_{FF}) over the hours for the cases O-$FF_{\dot{m}1}$, O-$FF_{\dot{m}2}$, O-$FF_{\dot{m}3}$ and (D) O-$FF_{\dot{m}4}$ are shown in Fig. 13. As expected, in the hours of highest solar incidence, the parameters Q_S, Q_{HTF}, Q_{FF} also present the highest values. The values of Q_{HTF} and Q_{FF} varied between 260.13 – 989.69 W and 247.40 – 524.33 W for O-$FF_{\dot{m}1}$, 95.93 – 656.16 W and 261.86 – 474.15 W for O-$FF_{\dot{m}2}$, 86.65 – 704.75 W and 288.08 – 460.31 W for O-$FF_{\dot{m}3}$ and 60.46 – 794.68 W and 278.17 – 461.55 W for O-$FF_{\dot{m}4}$, respectively. After 15:00 there is a smaller variation between the values of Q_{HTF} and Q_{FF}, in the case of lower mass flowrate (O-$FF_{\dot{m}1}$), when compared to the other cases. In addition, after that time the Q_{FF} exceeds the Q_{HTF} for the cases O-$FF_{\dot{m}2}$, O-$FF_{\dot{m}3}$ and O-$FF_{\dot{m}4}$, which indicates that the energy available in the FF is not effectively absorbed by the HTF.

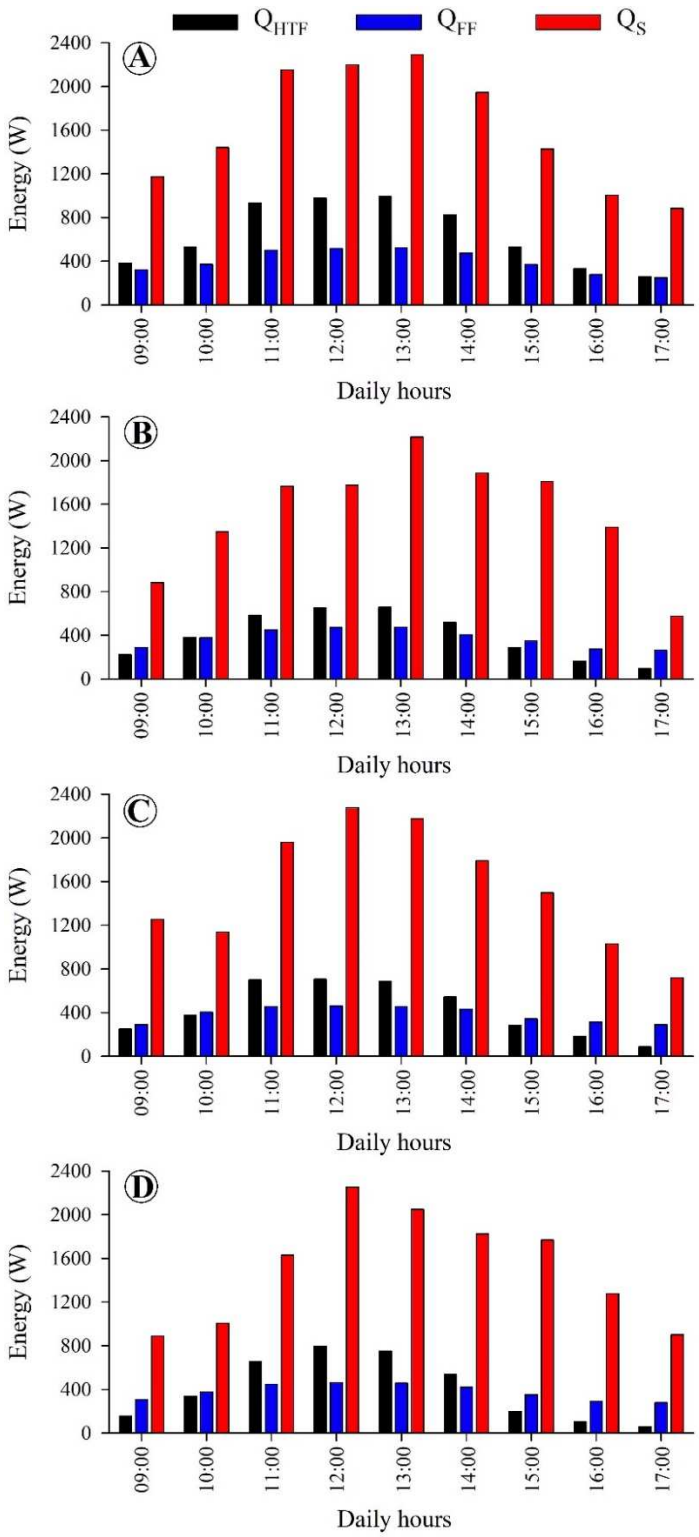

Fig. 13. Hourly variation of available solar energy (Q_S), useful energy absorbed by HTF (Q_{HTF}) and energy absorbed by FF (Q_{FF}) for (A) O-$FF_{\dot{m}1}$; (B) O-$FF_{\dot{m}2}$; (C) O-$FF_{\dot{m}3}$ and (D) O-$FF_{\dot{m}4}$.

Figure 14 shows the hourly variation of the thermal absorption efficiency (η_{TA}) and heat transfer efficiency (η_{HT}) for O-$FF_{\dot{m}1}$, O-$FF_{\dot{m}2}$, O-$FF_{\dot{m}3}$ and (D) O-$FF_{\dot{m}4}$. The maximum values of η_{HT} were obtained at times of higher solar incidence, while a greater hourly variation was observed for η_{TA}. For both cases, the thermal absorption efficiency is lower than the heat transfer efficiency along the day. It is also observed that the lowest efficiencies are obtained after 15:00 hours. The mean values of η_{TA} and η_{HT} were 36.6% and 59.7% for O-$FF_{\dot{m}1}$, 25.2% and 47.9% for O-$FF_{\dot{m}2}$, 25.7% and 48.5% for O-$FF_{\dot{m}3}$, and 24.9% and 44.7% for O-$FF_{\dot{m}4}$, respectively. Thus, the lower mass flowrate provided a more effective thermal absorption of the available solar energy and a better condition for the heat transfer between the FF and the HTF.

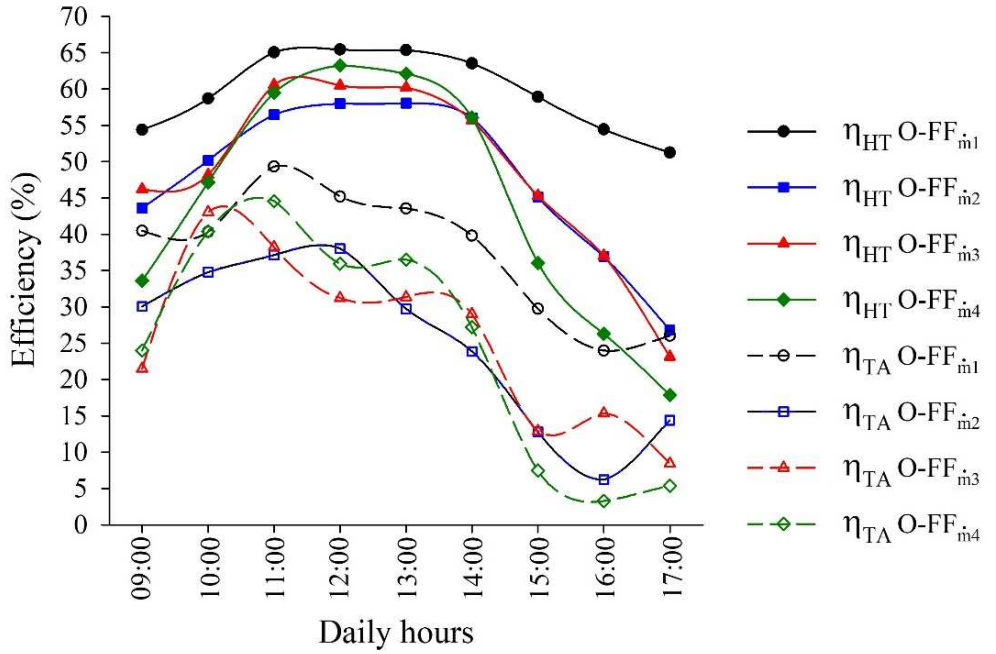

Fig. 14. Hourly variation of thermal absorption efficiency (η_{TA}) and heat transfer efficiency (η_{HT}) for O-$FF_{\dot{m}1}$, O-$FF_{\dot{m}2}$, O-$FF_{\dot{m}3}$ and O-$FF_{\dot{m}4}$.

3.4. Economic analysis

Prior to calculating the levelized cost of heat (LCOH) for the collector, it is first necessary to ascertain the capital cost of its components. This parameter was calculated considering the total cost required to manufacture the CPC. The c_c obtained was 250.4 \$ m^{-2} for the cases W-$FF_{\dot{m}1}$, A-$FF_{\dot{m}1}$ and 263.9 \$ m^{-2} for the other cases (Table 2). This difference is explained by the additional value of the thermal oil used as FF in the cases that presented higher C_c.

Table 2. Compound parabolic collector components cost

Material	Cost ($ m^{-2})
Evacuated tube 58 mm×1800 mm	49.91
Copper tube 3/8"×1000 mm	33.09
Stainless steel sheets 2000×1200×0.6 mm	72.73
Wooden board 20×150×1700 mm	27.15
Wood varnish 900 mL	3.37
Brass Fittings 3/8" and 1/2"	23.26
80L reservoir	5.35
200L reservoir	8.91
Glass wool 25×500×1000 mm	4.01
Aluminized self-adhesive blanket	13.22
Thermal oil (kg)	13.48
Screws, sandpaper, adhesive sealant, sealing rubbers and others	9.38
Total Cost (W-$FF_{\dot{m}1}$ and A-$FF_{\dot{m}1}$)	250.38
Total Cost (O-$FF_{\dot{m}1}$, O-$FF_{\dot{m}2}$, O-$FF_{\dot{m}3}$ and O-$FF_{\dot{m}4}$)	263.86

***** Dollar quoted on October 19th, 2022 (US$ 1.00 = R$ 5.28)

The LCOH and SPP of the proposed CPC were calculated as described in Eqs. 18 to 20 and are presented in Table 3, as well as the parameters used for their calculation. The LCOH values ranged from 0.034 to 0.053 $ kWh^{-1}. These values are close to those found for other CPCs available in the literature, such as 0.029 $ kWh^{-1} (Bhusal et al., 2020) and 0.028 – 0.039 $ kWh^{-1} (Widyolar et al., 2021). Among the cases under investigation, O-$FF_{\dot{m}1}$ had the lowest LCOH, while O-$FF_{\dot{m}4}$ presented the highest. This is related to the higher annual production of useful thermal energy obtained by O-$FF_{\dot{m}1}$. The SPP is used to analyze the duration of the CPC capital recovery, but this metric does not consider the time value of money. The highest and the lowest SPP values were 4.4 and 2.8 years for O-$FF_{\dot{m}1}$ and O-$FF_{\dot{m}4}$, respectively. Interestingly, the SPP found in this study were considerably lower than their useful life, which favors the viability of the investment.

Table 3. Leveled heat cost (LCOH) and simple payback period (SPP) for the proposed CPC

Cases	c_c ($ m^{-2})	c_{OEM} ($ m^{-2})	CRF	I_S (kWh m^{-2} year^{-1})	U_{EA} (kWh m^{-2})	LCOH ($ kWh^{-1})	SPP (years)
W-$FF_{\dot{m}1}$	250.38	5.00	0.078	1846.00	585.79	0.042	3.493
A-$FF_{\dot{m}1}$	250.38				573.53	0.043	3.568
O-$FF_{\dot{m}1}$	263.86				760.32	0.034	2.833
O-$FF_{\dot{m}2}$	263.86				498.07	0.051	4.325
O-$FF_{\dot{m}3}$	263.86				511.24	0.050	4.214
O-$FF_{\dot{m}4}$	263.86				485.22	0.053	4.440

4. CONCLUSION

This study investigated the influence of using different evacuated tube filling fluids (FF) on the thermal performance of a U-tube compound parabolic collector (CPC). The collector was designed, built and evaluated by a set of experimental trials. Three FF of the evacuated tube (water, air and thermal oil) and four mass flowrates (0.007, 0.009, 0.014, and 0.021 kg s^{-1}) were evaluated. A detailed energy analysis was performed for the evaluated cases, as well as an economic analysis. The main conclusions about the obtained results are summarized below:

- The highest temperature gains occurred at noon, correlated with maximum solar radiation. Air as the FF led to the highest temperature, followed by oil and water. Elevated HTF mass flowrate notably reduced temperature gain.
- The type of FF significantly impacts the thermal performance of the CPC, with thermal oil resulting in about 30.0% and 32.5% higher thermal efficiency than water and air, respectively. Higher flow rates, however, decrease the thermal efficiency of the CPC by up to 36.2%.
- For all evaluated hours, thermal oil proved optimal for solar energy absorption, particularly during periods of lower solar incidence, efficiently transferring energy to the HTF.
- Although air showed the highest values of heat transfer efficiency, its useful energy absorption for this configuration remained low. Additionally, there was a reduction in the amount of energy absorbed by the HTF with increasing mass flowrate.
- The lowest values of Levelized Cost of Heat (LCOH) and Simple Payback Period (SPP) were observed in the collector configuration using thermal oil as the filling fluid and with the lowest HTF mass flowrate, indicating that this was the best configuration in economic terms.

5. REFERENCES

Abokersh, M.H., El-Morsi, M., Sharaf, O., Abdelrahman, W. An experimental evaluation of direct flow evacuated tube solar collector integrated with phase change material. **Energy**, v.139, p.1111-1125, 2017. https://doi.org/10.1016/j.energy.2017.08.034

Barbosa, E.G., Martins, M.A., Araujo, M.E.V., Renato, N.S., Zolnier, S., Pereira, E.M., Resende, M.O. Experimental evaluation of a stationary parabolic trough solar collector: Influence of the concentrator and heat transfer fluid. **Journal of Cleaner Production**, v.276, 124174, 2020a. https://doi.org/10.1016/j.jclepro.2020.124174

Barbosa, E.G., Araujo, M.E.V., Lopes, R.P., Martins, M.A., Moraes, M.J., Barbosa, E.G., Falconí, J.H.H. Exergetic, economic and environmental (3E) analysis of a low cost solar heater in different configurations. **Renewable Energy,** v.160, p.1096-1104, 2020b. https://doi.org/10.1016/j.renene.2020.07.060

Bhusal, Y., Hassanzadeh, A., Jiang, L., Winston, R. Technical and economic analysis of a novel low-cost concentrated medium-temperature solar collector. **Renewable Energy**, v.146, p.968-985, 2020. https://doi.org/10.1016/j.renene.2019.07.032

Carvalho, M.J., Collares-Pererira, M., Gordon, J.M., Rabl, A. Truncation of CPC solar collectors and its effect on energy collection. **Solar Energy**, v.35, p.393-399, 1985. https://doi.org/10.1016/0038-092X(85)90127-6

CEMIG, 2022. Companhia Energética de Minas Gerais – **Valores de tarifas e serviços**. Available in: https://www.cemig.com.br/atendimento/valores-de-tarifas-e-servicos/ Accessed in: 20 October, 2022.

Chen, X., Yang, X. Solar collector with asymmetric compound parabolic concentrator for winter energy harvesting and summer overheating reduction: Concept and prototype device. **Renewable Energy**, v.173, p.92-104, 2021. https://doi.org/10.1016/j.renene.2021.03.119

Chen, X., Yang, X. Heat transfer enhancement for U-pipe evacuated tube solar absorber by high-emissivity coating on metal fin. **Journal of Building Engineering**, v.50, 104213, 2022. https://doi.org/10.1016/j.jobe.2022.104213

Collares-Pereira, M., Rabl, A. The average distribution of solar radiation-correlations between diffuse and hemispherical and between daily and hourly insolation values. **Solar Energy**, v.22, p.155-164, 1979. https://doi.org/10.1016/0038-092X(79)90100-2

Essa, M.A., Asal, M., Saleh, M.A., Shaltout, R.E. A comparative study of the performance of a novel helical direct flow U-Tube evacuated tube collector. **Renewable Energy**, v.163, p.2068-2080, 2021. https://doi.org/10.1016/j.renene.2020.10.109

Huang, J., Fan, J., Furbo, S., Chen, D., Dai, Y., Kong, W. Economic analysis and optimization of household solar heating technologies and systems. **Sustainable Energy Technologies and Assessments**, v.36, 100532, 2019. https://doi.org/10.1016/j.seta.2019.100532

Kim, H., Kim, J., Cho, H. Experimental study on performance improvement of U-tube solar collector depending on nanoparticle size and concentration of Al_2O_3 nanofluid. **Energy**, v.118, p.1304-1312, 2017. https://doi.org/10.1016/j.energy.2016.11.009

Korres, D.N., Tzivanidis, C. Numerical investigation and optimization of an experimentally analyzed solar CPC. **Energy**, v.172, p.57-67, 2019. https://doi.org/10.1016/j.energy.2019.01.119

Kurhe, N., Pathak, A., Deshpande, K., Jadkar, S. Compound parabolic solar collector – Performance evaluation as per standard test method and actual field conditions for industrial process heat application in Indian context. **Energy for Sustainable Development**, v.57, p.98-108, 2020. https://doi.org/10.1016/j.esd.2020.06.001

Li., X., Dai, Y.J., Li, Y., Wang, R.Z. Comparative study on two novel intermediate temperature CPC solar collectors with the U-shape evacuated tubular absorber. **Solar Energy**, v.93, p.220-234, 2013. https://doi.org/10.1016/j.solener.2013.04.002

Liang, R., Ma, L., Zhang, J., Zhao, D. Theoretical and experimental investigation of the filled-type evacuated tube solar collector with U tube. **Solar Energy**, v.85, p.1735-1744, 2011. https://doi.org/10.1016/j.solener.2011.04.012

Liang, R., Ma, L., Zhang, J., Zhao, L. Performance analysis of a new-design filled-type solar collector with double U-tubes. **Energy and Buildings**, v.57, p.220-226, 2013. https://doi.org/10.1016/j.enbuild.2012.11.004

Moffat, R.J. Using uncertainty analysis in the planning of an experiment. **Journal of Fluids Engineering**, v.107, p.173-178, 1985. https://doi.org/10.1115/1.3242452

Naik, B.K., Bhowmik, M., Muthukumar, P. Experimental investigation and numerical modelling on the performance assessments of evacuated U – Tube solar collector systems. **Renewable Energy**, v.134, p.1344-1361, 2019. https://doi.org/10.1016/j.renene.2018.09.066

Olfian, H., Ajarostaghi, S.S.M., Farhadi, M., Ramiar, A. Melting and solidification processes of phase change material in evacuated tube solar collector with U-shaped spirally corrugated tube. **Applied Thermal Engineering**, v.182, 116149, 2021. https://doi.org/10.1016/j.applthermaleng.2020.116149

Ósorio, T., Horta, P., Marchã, M., Collares-Pereira, M. One-Sun CPC-type solar collectors with evacuated tubular receivers. **Renewable Energy**, v.134, p.247-257, 2019. https://doi.org/10.1016/j.renene.2018.11.017

Pereira, E.B., Martins, F.R., Gonçalves, A.R., Costa, R.S., Lima, F.J.L., Rüther, R., Abreu, S.L., Tiepolo, G.M., Pereira, S.V., Souza, J.G. **Atlas brasileiro de energia solar** (2 ed), Swera, São José dos Campos, 80p. 2017.

Rabl, A. Radiation transfer through specular passages – a simple approximation. International **Journal of Heat and Mass Transfer**, v.20, p.323-330, 1977. https://doi.org/10.1016/0017-9310(77)90153-3

Rabl, A., O'Gallagher, J., Winston, R. Design and test of non-evacuated solar collectors with compound parabolic concentrators. **Solar Energy**, v.25, p.335-351, 1980. https://doi.org/10.1016/0038-092X(80)90346-1

Ralb, A. **Active Solar Collectors and Their Applications**. Oxford University Press, New York. 1985.

Ralb, A., Goodman, N.B., Winston, R. Practical design considerations for CPC solar collectors. **Solar Energy**, v.22, p.373-381, 1979. https://doi.org/10.1016/0038-092X(79)90192-0

REN21. **Renewables 2022 Global Status Report** (Paris: REN21 Secretariat). In Tech. Rep. p.1-311, 2022.

Sharma, A.K., Sharma, C., Mullick, S.C., Kandpal, T.C. Solar industrial process heating: A review. **Renewable and Sustainable Energy Reviews**, v.78, p.124-137, 2017. https://doi.org/10.1016/j.rser.2017.04.079

Ustaoglu, A., Alptekin, M., Okajima, J., Maruyama, S. Evaluation of uniformity of solar illumination on the receiver of compound parabolic concentrator (CPC). **Solar Energy**, v.132, p.150-164, 2016. https://doi.org/10.1016/j.solener.2016.03.014

Widyolar, B., Jiang, L., Bhusal, Y., Brinkley, J., Winston, R. Solar thermal process heating with the external compound parabolic concentrator (XCPC) – 45 m^2 experimental array performance, annual generation (kWh/m^2-year), and economics. **Solar Energy**, v.230, p.131-150, 2021. https://doi.org/10.1016/j.solener.2021.10.027

Zare, V., Moalemian, A. Parabolic trough solar collectors integrated with a Kalina cycle for high temperature applications: Energy, exergy and economic analyses. **Energy Conversion and Management**, v.151, p.681-692, 2017. https://doi.org/10.1016/j.enconman.2017.09.028

CHAPTER 3

OPTIMIZING PERFORMANCE OF A MULTILAYERED SENSIBLE HEAT PACKED BED THERMAL STORAGE SYSTEM WITH VARIABLE PARTICLE DIAMETER

Abstract: Packed bed thermal energy storage (PBTES) is crucial for increasing the reliability of solar thermal systems. The use of multilayered PBTES with variable particle diameter has been investigated to improve the performance of these systems. However, the impact of employing these combined techniques in sensible heat storage has not been reported yet. This study aimed to numerically explore the impact of employing variable diameter on the thermal performance of a multilayer sensible heat PBTES. Furthermore, a sensitivity analysis of different correlations for the heat transfer coefficient and effective thermal conductivity of the bed was conducted to obtain a more accurate model. Energy and exergy efficiency of the system, thermocline thickness, and MIX number were used as parameters for this evaluation. The use of materials with lower thermal conductivity resulted in an increase in the temperature difference between the heat transfer fluid and the solid material. The effective charge and discharge times varied between 2.07 and 2.2 hours. The multilayer configuration had a greater influence on the charge and discharge times, as well as on the stored (Q_C) and released (Q_D) heat, compared to the particle diameter. Generally, case 6 for charging and case 9 for discharging showed the best performances in terms of thermal stratification. These cases have the same configuration regarding the HTF inlet, where the multilayers were arranged in ascending order, considering both the thermal properties of the materials and the particle diameters. Case 9 presented the highest values for Q_C (27.2 MJ), charge efficiency (87.5%), discharge efficiency (80.5%), and exergy efficiency (70.5%). These values are 7.7%, 9.5%, 4.0%, and 13.9% higher than those observed for the reference treatment (case 1), respectively. Cases 6 for charging and 9 for discharging provided lower temperature gradients in the PBTES and generally had the lowest values for thermocline thickness. It was also observed that for these cases, the MIX number remains below 0.5 for approximately 43% of the total charge and discharge time. The combined results indicate that these cases provide better thermal stratification and, therefore, improve heat transfer in the PBTES.

Keywords: Energy and exergy efficiencies. Multilayer PBTES. Sensibility analysis. Thermal stratification. Thermocline.

Greek letters

ρ	–	Density, kg m^{-3};
δ	–	Thermocline, m;
ε	–	Bed porosity;
η	–	Efficiency, %;
μ	–	Dynamic viscosity, kg m^{-1} s^{-1};

Symbols list

$\vec{g}$	–	Gravitational acceleration vector, m s^{-2};
$\vec{u}$	–	Superficial velocity vector, m s^{-1};
$\dot{m}$	–	Mass flow rate, kg s^{-1};
A	–	Area (specific surface), m^{-1};
Cp	–	Specific heat, kJ kg^{-1} K^{-1};
D	–	Diameter of the PBTES, m;
d	–	Diameter, m;
EM	–	Energy moment, J m;
H	–	Total height of the PBTES, m;
h	–	Heat transfer coefficient, W m^{-2} K^{-1};
k	–	Thermal conductivity, W m^{-1} K^{-1};
M	–	Storage materials;
P	–	Static pressure, Pa;
Pr	–	Prandtl number;
Q	–	Thermal energy stored or released during the process, J;
Re	–	Reynolds number;
T	–	Temperature, ºC;
t	–	Effective time, s;
V	–	Volume, m^3;
x	–	Height of the considered point, m;
y	–	Axial position in the PBTES, m;

Subscripts

$_{\delta}$	–	From the center of the thermocline to the bottom of the reservoir;
$_{amb}$	–	Ambient;
$_{C}$	–	Charging;
$_{C,cut}$	–	Charging cut-off;

$_{cold}$ – Lowest observed in the layer / cold layer;

$_{D}$ – Discharging;

$_{D,cut}$ – Discharging cut-off;

$_{eff,f}$ – Effective of fluid;

$_{eff,s}$ – Effective of solid;

$_{ex}$ – Exergy;

$_{exp}$ – Experimental reservoir;

$_{f}$ – Fluid;

$_{f,in}$ – Fluid inlet;

$_{f,out}$ – Fluid outlet;

$_{fs}$ – Interstitial;

$_{hot}$ – Highest observed in the layer / hot layer;

$_{i}$ – Of each layer;

$_{ib}$ – From the center of the layer to the bottom of the reservoir

$_{L}$ – Layer;

$_{lo}$ – Lower critical limit of the thermocline region (T_D + 5 ºC);

$_{mix}$ – Completely mixed reservoir;

$_{p}$ – Particle;

$_{s,c}$ – Concrete;

$_{s,i}$ – Cast iron;

$_{s,q}$ – Quartzite rock;

$_{sf}$ – Specific surface;

$_{str}$ – Fully stratified reservoir;

$_{T}$ – Thickness;

$_{up}$ – Upper critical limit of the thermocline region (T_C – 5 ºC);

1. INTRODUCTION

The global energy scenario is transitioning towards energy production independent of the use of fossil fuels. Using renewable and sustainable energy sources (such as solar energy) is critical to achieving this goal. The unstable nature and temporal intermittency associated with this source type cause an imbalance between energy availability and demand. This fact is the main obstacle to its consolidation (Chen et al., 2023). The primary efforts to improve the reliability of solar systems must focus on improving their ability to supply energy demand for considerable periods. This fact is emphasized by the major reports addressing renewable energies published over the years (IEA, 2010; SunShot, 2012; Mehos et al., 2017). Consequently, thermal energy storage (TES) systems have become crucial in bridging the gap between energy generation and consumption.

The packed bed thermal energy storage (PBTES) consists of an insulated reservoir filled with a solid material, in which heat transfer occurs directly between the heat transfer fluid (HTF) and the thermal storage medium (Palomba and Frazzica, 2022). Sensible heat storage in PBTES is a mature and mechanically stable technique that is widely accessible. It is also more economically viable compared to latent heat storage. Furthermore, this system can be used over a wide temperature range and integrated into different thermal operations. In these systems, thermal energy is stored by increasing the temperature of the material (Alptekin and Ezan, 2020). Consequently, the thermo-physical properties of the materials directly affect their thermal performance. These properties relate to the stored and extracted energy density and the heat transfer efficiency (Seyitini et al., 2023). In addition to the thermophysical parameters, there are geometric parameters that affect the available heat exchange area and flow resistance. Furthermore, operational parameters such as operating temperature, fluid mass flow rate, and bed porosity should also be emphasized (Gautam and Saini, 2020). Understanding and optimizing these parameters and their interactions are vital to achieving increasingly efficient and viable PBTES systems.

Over the years, several researchers have evaluated the influence of different parameters and control strategies on the performance of PBTES, mainly related to its stratification, storage capacity, and effective heat transfer. Lugolole et al. (2018) assessed the effect of two particle diameters (10.5 mm and 31.9 mm) on the thermal performance of PBTES during charging cycles. The results showed that the bed with a smaller diameter exhibited higher energy and exergy rates. Elsihy et al. (2021) conducted a study using modeling and simulation to investigate the thermocline characteristics and discharge performance of a molten

salt PBTES. Three different materials, namely quartzite rock, slag pebbles, and alumina ceramic, were compared, and the effects of HTF inlet flow rate and particle diameter were evaluated. The authors found that the particle size and material properties primarily affect the temperature stability during discharge. Other materials have also been studied as storage media in PBTES, such as demolition waste (Kocak and Paksoy, 2020), recycled ceramics (Al-Azawii et al., 2021), sintered ore, alumina oxide, and crushed rock (Zhou et al., 2022).

The use of PBTES in a multilayer or cascade arrangement has proven to be an effective strategy for optimizing these systems. This approach involves using different materials in alternating layers within a single reservoir. Li et al. (2018a) compared the thermal performance of a single-layer packed bed tank (SLPBTT) with a multilayer packed bed tank (MLPBTT). Three layers filled with different materials were used. The authors concluded that using MLPBTT enabled an improvement of approximately 10.5% in the stored useful energy with a slight decrease in thermal efficiency (2.1%) compared to SLPBTT. Türkakar (2021) analyzed the performance of a PBTES composed of three layers of different materials. The materials were arranged according to their heat capacity. The multilayer configuration improved the thermal energy storage and stratification level by approximately 85% and 135%, respectively. The effect of using layers with different particle diameters of a single material was also studied. Li et al. (2018b) evaluated the performance of a high-temperature PBTES with two layers and variable diameter. The maximum charging rate was improved by up to 12.4%, and the density increased by 13% using a two-layer PBTES. Additionally, the combined effect of multilayer PBTES with different materials containing particles with varying diameters has recently been reported for latent heat storage with phase change materials (Zhu et al., 2021; Liu et al., 2023; Mao and Cao, 2023). Overall, the results indicate that using multilayer PBTES with variable diameter particles improves the performance of these systems, and an ideal combination can be achieved through optimization studies.

Due to the complexity of the mechanisms involved in the operation of PBTES and the high cost and time associated with experimental evaluation, a significant portion of the studies available in the literature uses numerical modeling as an effective analysis tool. The computational fluid dynamics (CFD) method has been employed to design and assess various types of systems. This method provides opportunities to investigate various phenomena and their combined implications from a comprehensive and detailed perspective, enabling efficient optimization (Chekifi and Boukraa, 2023). In PBTES, heat transfer can occur simultaneously through different mechanisms (conduction, convection, and radiation), which makes precise modeling challenging. The main parameters used to represent these complex heat exchange

phenomena are the interstitial heat transfer coefficient between the fluid and the solid (h_{fs}) and the effective thermal conductivities of the fluid ($k_{eff,f}$) and the solid ($k_{eff,s}$) (Palomba and Frazzica, 2022). Over the years, numerous correlations have been proposed for calculating these parameters based on experimental results (Días-Heras et al., 2020; Calderón-Vásquez et al., 2021). However, there is limited information regarding the effect of using different correlations on the predicted performance. Understanding and properly utilizing these predicted parameters are essential to ensure the accuracy and reliability of the results.

The sensible heat PBTES is a highly researched alternative to overcome the challenges imposed by the instability of solar energy caused by its temporal intermittency. Numerous parameters and strategies have been investigated to enhance the efficiency of these systems. The utilization of multilayered PBTES with particles of different diameters has shown promising results. These techniques enable the optimization of effective thermal properties, available surface area for heat exchange, and bed storage capacity. As demonstrated in the literature review, the beneficial effect of multilayered PBTES combined with particles of varying diameters has already been substantiated for latent heat storage. However, despite its benefits, studies evaluating the effect of using these combined techniques in sensible heat storage are still scarce. In our perspective, this study is the first in the literature to investigate the effect of varying diameters on the thermal performance of a multilayered sensible heat PBTES. First and second law efficiencies, thermocline thickness, and MIX number were utilized to assess the performance of the studied cases during the charging and discharging processes. Additionally, a sensitivity analysis of different correlations for the heat transfer coefficient and effective thermal conductivity of the bed is also reported. It is important to remark that, this analysis is commonly overlooked in most studies.

2. MODEL DESCRIPTION

2.1. Physical model

The physical model and operation of a typical PBTES are presented in Fig. 1. The studied PBTES consists of an isolated and vertically positioned cylindrical reservoir. This reservoir is filled with sensible heat storage materials that form the packed bed. Distributors are placed adjacent to the inlet and outlet of the reservoir to ensure uniform HTF flow. During the charging process, the heated HTF flows from the top of the reservoir to the bottom, transferring heat to the storage material. Conversely, during the discharging process, the flow direction is

reversed. Thus, the cold HTF flows from the bottom of the reservoir to the top and is heated by the thermal energy stored in the solid material.

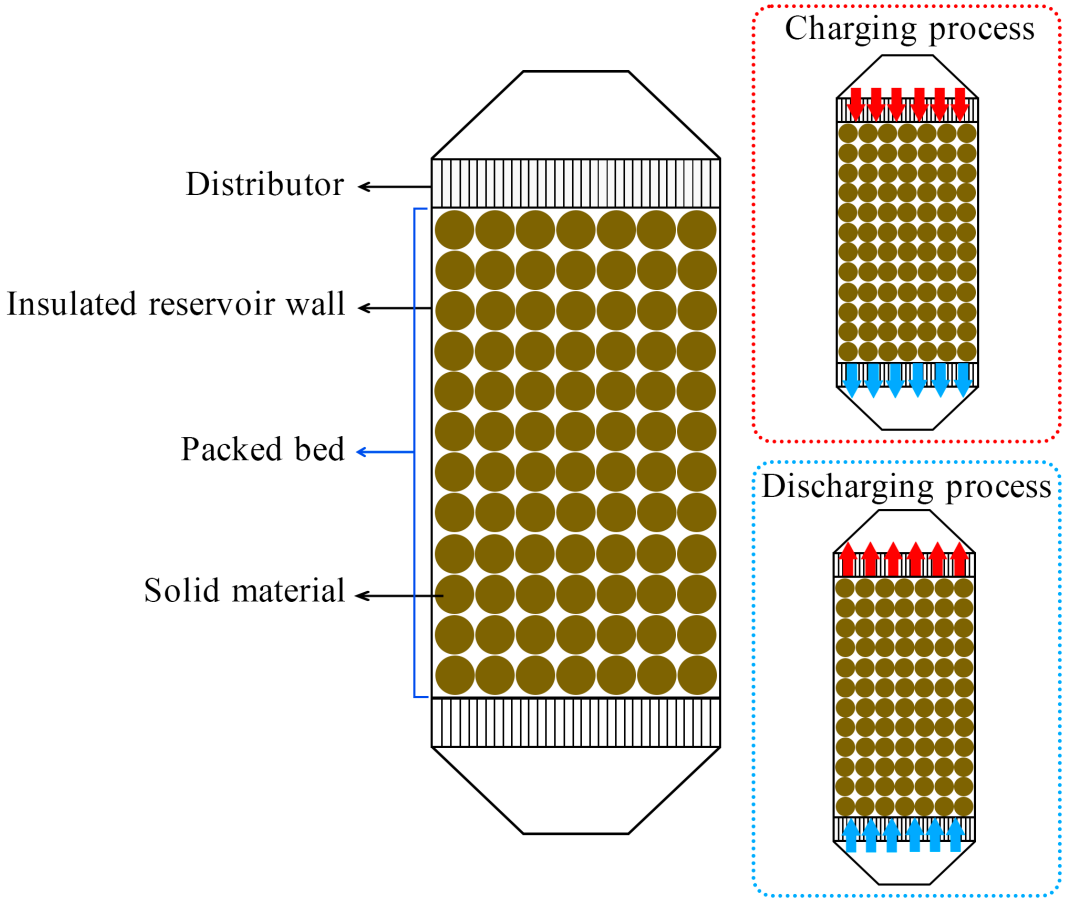

Fig. 1. Schematic diagram of a typical packed bed thermal energy storage (PBTES) system.

In this study, a comprehensive investigation was conducted on the performance of a sensible heat PBTES. The effect of using different materials in multilayers was evaluated. The variation in particle diameter and the interaction between these factors were also considered. In total, 9 cases were investigated, namely: single-layer PBTES with a fixed particle diameter (case 1), single storage material PBTES with variable particle diameter layers (cases 2 and 3), multilayer PBTES with a fixed material and particle diameter (cases 4 and 5), and multilayer PBTES with variable materials and particle diameters (cases 6 to 9). Fig. 2 provides a detailed overview of the different cases and their configurations. The storage materials were arranged in the multilayer cases based on their volumetric heat capacity, either in ascending or descending order. The particle diameters were also similarly ordered. It is worth noting that the diameters were the same within each layer, although they could vary among different layers.

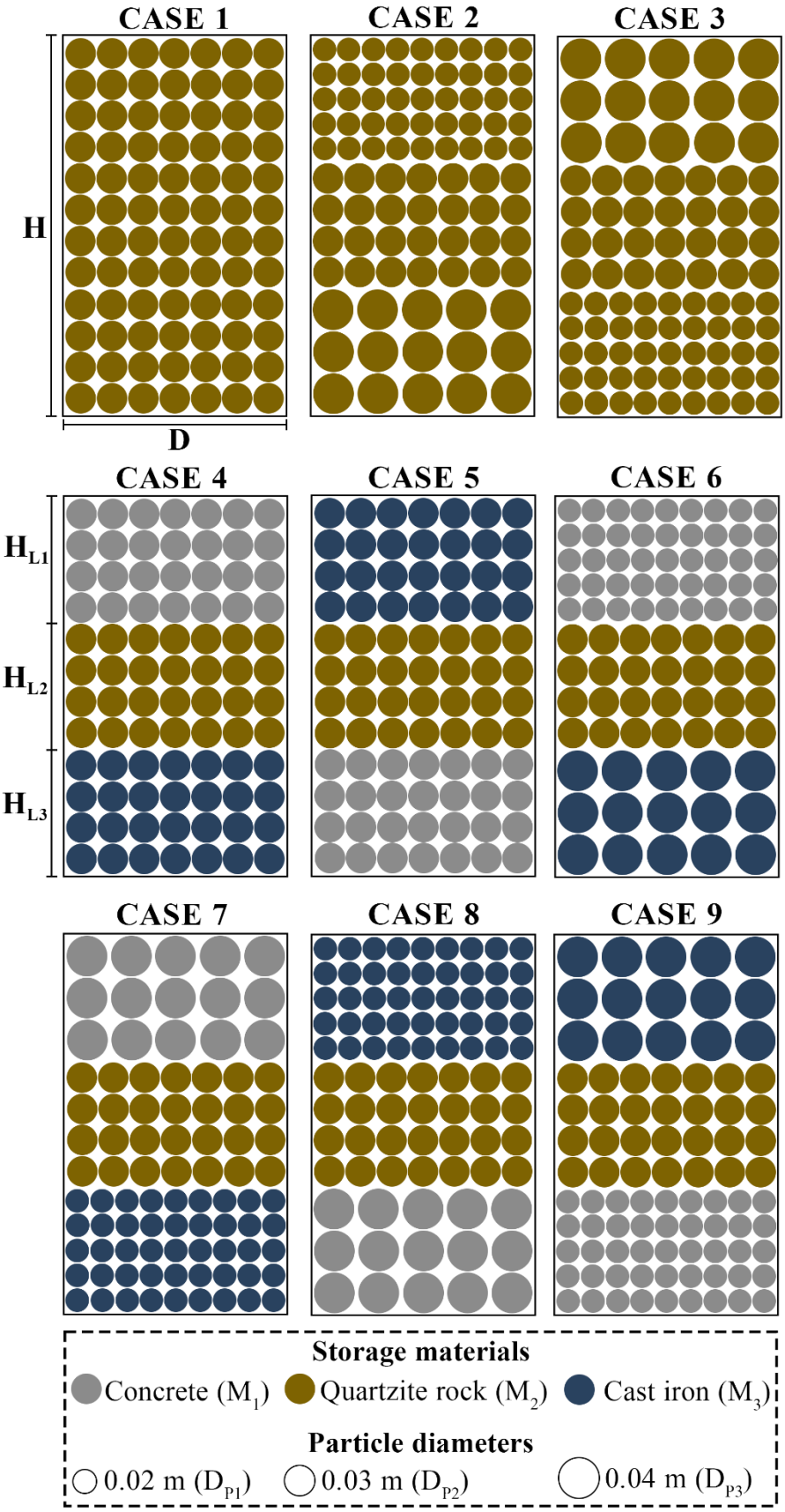

Fig. 2. Detailed diagram of parameters and configurations evaluated.

The PBTES had a fixed height (H) and diameter (D) for all the evaluated cases. In the multilayer cases, each layer had the same height (H_L). Three particle diameters (d_{p1}, d_{p2}, and d_{p3}) and three storage materials (M_1, M_2, and M_3) were investigated in the packed bed. According to Martí et al. (2018), the chosen diameter values are within the range that provides the highest efficiency for PBTES. Concrete, quartzite rock, and cast iron were evaluated as sensible heat storage materials. These materials were selected due to their properties, availability, and cost. Table 1 presents the main geometric and operational parameters and the thermophysical properties of the sensible heat storage materials (Calderón-Vásquez et al., 2021). In this study, the temperature difference for the charging and discharging processes is defined as 30% of (T_C - T_D) (Ma et al., 2021). This value sets the limit for the cut-off temperature for charging ($T_{C,cut}$) and discharging($T_{D,cut}$).

Table 1. Geometric, operational, and thermophysical parameters of sensible heat storage materials

Especifications	Symbol	Value	Unit
Geometric parameters			
Packed bed height	H	1.2	m
PBTES diameter	D	0.3	m
Layer height in the bed	H_{L1}, H_{L2} e H_{L3}	0.4	m
Particle diameters	d_{p1}	0.02	m
	d_{p2}	0.03	
	d_{p3}	0.04	
Operational parameters			
Charging temperature	T_C	130	°C
Discharging temperature	T_D	25	°C
Ambient temperature	T_{amb}	25	°C
Cut-off temperature for charging	$T_{C,cut}$	98.5	°C
Cut-off temperature for discharging	$T_{D,cut}$	56.5	°C
HTF mass flowrate	$\dot{m}$	0.02	kg s^{-1}
Thermophysical properties			
Concrete (M_1)			
Density	$\rho_{s,c}$	2750	kg m^{-3}
Specific heat	$Cp_{s,c}$	916	J kg^{-1} K^{-1}
Thermal conductivity	$k_{s,c}$	1.0	W m^{-1} K^{-1}
Volumetric heat capacity	$\rho Cp_{s,c}$	2516	kJ m^{-3} K^{-1}
Quartzite rock (M_2)			
Density	$\rho_{s,q}$	2570	kg m^{-3}
Specific heat	$Cp_{s,q}$	1185	J kg^{-1} K^{-1}
Thermal conductivity	$k_{s,q}$	3.5	W m^{-1} K^{-1}
Volumetric heat capacity	$\rho Cp_{s,q}$	3046	kJ m^{-3} K^{-1}
Cast iron (M_3)			
Density	$\rho_{s,i}$	7200	kg m^{-3}
Specific heat	$Cp_{s,i}$	560	J kg^{-1} K^{-1}
Thermal conductivity	$k_{s,i}$	37	W m^{-1} K^{-1}
Volumetric heat capacity	$\rho Cp_{s,i}$	4032	kJ m^{-3} K^{-1}

The synthetic thermal oil Therminol 66 was used as the HTF in all evaluations. The density (ρ_f), specific heat (Cp_f), and thermal conductivity (k_f) of Therminol 66 vary with temperature, as shown in Eqs. 1 to 3, respectively (Kocak et al., 2020).

$$\rho_f = -0.614254T - 0.000321T^2 + 1020.62 \quad (1)$$

$$Cp_f = 0.003313T - 0.00000008970785T^2 + 1.496005 \quad (2)$$

$$k_f = -0.000033T - 0.00000015T^2 + 0.118294 \quad (3)$$

2.2. Mathematical model

In this study, a transient, continuous solid phase, and local thermal non-equilibrium model (LTNE) was implemented to analyze the performance of the proposed PBTES. This model considers the packed bed as a continuous porous medium rather than a medium composed of individual particles. The model was developed considering real operating conditions, and several appropriate assumptions were addressed:

(1) The flow is laminar, incompressible, and uniform at the inlet and outlet of the PBTES.
(2) The packed bed is considered a homogeneous and continuous porous medium.
(3) There is no heat exchange between the PBTES and the surroundings.
(4) Heat transfer occurs only in the axial direction.
(5) The properties of the HTF vary with temperature, while the properties of the solid materials are constant.
(6) Radiative heat transfer is neglected.

Considering the assumptions (1) to (6), the governing equations of the continuous solid phase model are described as follows. The continuity and momentum equations can be expressed as Eqs. 4 and 5, respectively. The permeability (σ) and inertial coefficient (C_F) are used to calculate the pressure drop across the porous bed, according to Eqs. 6 and 7 (Ergun, 1952).

$$\frac{\partial(\varepsilon\,\rho_f)}{\partial t} + \nabla \cdot (\rho_f \vec{u}) = 0 \tag{4}$$

$$\frac{\partial}{\partial t}(\rho_f \vec{u}) + \nabla(\rho_f \vec{u}\vec{u}) = -\nabla P + \mu_f \nabla^2 \vec{u} + \rho_f \vec{g} - \left(\frac{\mu_f}{\sigma} + C_F \frac{1}{2}\rho_f |\vec{u}|\right)\vec{u} \tag{5}$$

$$\sigma = \frac{\varepsilon^3}{(1-\varepsilon)^2}\frac{{d_p}^2}{150} \tag{6}$$

$$C_F = \frac{3.5}{d_p}\frac{(1-\varepsilon)}{\varepsilon^3} \tag{7}$$

In the LTNE model, the energy equations are solved separately for each phase. These equations are coupled using a heat source term defined by the volumetric interstitial heat transfer rate. The energy conservation equations for the fluid and solid phases were described in Eqs. 8 and 9, respectively.

$$\varepsilon\,\rho_f\,C_{pf}\frac{\partial T_f}{\partial t} + \rho_f\,C_{pf}\,u\,\nabla T_f = \nabla(k_{eff,f}\nabla T_f) + h_{fs}\,A_{fs}(T_s - T_f) \tag{8}$$

$$(1-\varepsilon)\,\rho_s\,C_{ps}\frac{\partial T_s}{\partial t} = \nabla(k_{eff,s}\nabla T_s) + h_{fs}\,A_{fs}(T_f - T_s) \tag{9}$$

The specific surface area (A_{sf}) is defined as the surface area of the solid phase per unit volume of the bed and was described in Eq. 10. The model also considers the variation of the porosity of the packed bed (ε) as a function of the reservoir diameter (D) and the particle diameter (d_p). The correlation proposed by Dixon (1988) is used for this purpose (Eq. 11). The dimensionless Reynolds number of the particle (Re_p) and the Prandtl number (Pr) were defined in Eqs. 12 and 13, respectively.

$$A_{fs} = \frac{A_{s,tot}}{V_b} = \frac{6(1-\varepsilon)}{d_p} \tag{10}$$

$$\varepsilon = 0.4 + 0.05\left(\frac{d_p}{D}\right) + 0.412\left(\frac{d_p}{D}\right)^2 \tag{11}$$

$$Re_p = \frac{\rho_f\,u\,d_p}{\mu_f} \tag{12}$$

$$Pr = \frac{C_{pf}\,\mu_f}{k_f} \tag{13}$$

In this study, a sensitivity analysis was performed to evaluate the impact of different correlations on the interstitial heat transfer coefficient between the fluid and solid (h_{fs}) and the effective thermal conductivities ($k_{eff,f}$ and $k_{eff,s}$) on the predicted performance using the implemented model. The correlations evaluated for calculating h_{fs} and k_{eff} can be observed in Eqs. 14 to 18 and Eqs. 19 to 23, respectively (Xu et al., 2012; Calderón-Vásquez et al., 2021).

$$h_{fs}(C_1) = \frac{k_f}{d_p}\left(2 + 1.8\,Re_p^{\frac{1}{2}}Pr^{\frac{1}{3}}\right) \tag{14}$$

$$h_{fs}(C_2) = \frac{k_f}{d_p}\left(3.22\,Re_p^{\frac{1}{3}}Pr^{\frac{1}{3}} + 0.117\,Re_p^{0.8}Pr^{0.4}\right) \tag{15}$$

$$h_{fs}(C_3) = \left(\frac{d_p\,\varepsilon}{0.2555\,Re_p^{\frac{2}{3}}Pr^{\frac{1}{3}}k_f} + \frac{d_p}{10k_s}\right)^{-1} \tag{16}$$

$$h_{fs}(C_4) = \frac{k_f}{d_p}\left(2 + 1.1\,Re_p^{0.6}Pr^{\frac{1}{3}}\right) \tag{17}$$

$$h_{fs}(C_5) = \frac{k_f}{d_p}\left(ab + (1.33 - 2.4\,\varepsilon + 1.2\varepsilon^2)\,Re_p^{0.7}Pr^{\frac{1}{3}}\right) \tag{18}$$

where $a = (7 - 10\varepsilon + 5\varepsilon^2)$, $b = (1 + 0.7Re_p^{0.2}Pr^{\frac{1}{3}})$

$$k_{eff}(C_1) = \begin{cases} k_{eff,l} = \varepsilon k_f \\ k_{eff,s} = (1-\varepsilon)\, k_s \end{cases} \tag{19}$$

$$k_{eff}(C_2) = \begin{cases} k_{eff,f} \begin{cases} 0.7\varepsilon k_f, & Re_p < 0.8 \\ 0.5 Re_p Pr k_f, & Re_p > 0.8 \end{cases} \\ k_{eff,s} = k_{eff,t} - k_{eff,f}, \;\; where \;\; k_{eff,t} = k_f \left(\frac{k_s}{k_f}\right)^m + 0.5R\square\square_p Pr k_f, \;\; m = 0.28 - 0.757 \log \varepsilon - 0.057 \log\left(\frac{k_s}{k_f}\right) \end{cases} \tag{20}$$

$$k_{eff}(C_3) = \begin{cases} k_{eff,l} = \varepsilon k_f \\ k_{eff,s} = k_s \left(\frac{3(1-\varepsilon^2)}{3.6\, x\, 10^{10}} \frac{59.8 d_p}{2}\right)^{\frac{1}{3}} \frac{1}{0.531 d_p} + k_f \left[1 - \sqrt{1-\varepsilon} + \frac{2\sqrt{1-\varepsilon}}{1-aB}\left[\frac{(1-a)B}{(1-aB)^2} \ln\left(\frac{1}{aB}\right) - \frac{B+1}{2} - \frac{B-1}{1-aB}\right]\right], where\ a = \frac{k_f}{k_s}, B = 1.25\left(\frac{(1-\varepsilon)}{\varepsilon}\right)^{\frac{10}{9}} \end{cases} \tag{21}$$

$$k_{eff}(C_4) = \begin{cases} k_{eff,f} = \rho c_{p,f} |\vec{u}| d_p \left(\frac{0.73}{Re_p Pr} + \frac{0.5}{1 + \frac{9.7}{Re_p Pr}}\right) \\ k_{eff,s} = k_f \left[1 - \sqrt{1-\varepsilon} + \frac{2\sqrt{1-\varepsilon}}{1-aB}\left[\frac{(1-a)B}{(1-aB)^2} \ln\left(\frac{1}{aB}\right) - \frac{B+1}{2} - \frac{B-1}{1-aB}\right]\right], where\ a = \frac{k_f}{k_s}, B = 1.25\left(\frac{(1-\varepsilon)}{\varepsilon}\right)^{\frac{10}{9}} \end{cases} \tag{22}$$

$$k_{eff}(C_5) = \begin{cases} k_{eff,f} = k_f \left(\dfrac{1 + 2\left(\frac{k_s - k_f}{k_s + 2k_f}\right)(1-\varepsilon) + \left(2\left(\frac{k_s - k_f}{k_s + 2k_f}\right)^3 - 0.1\left(\frac{k_s - k_f}{k_s + 2k_f}\right)\right)(1-\varepsilon)^2 + (1-\varepsilon)^3 0.05 exp\left(4.5 \frac{k_s - k_f}{k_s + 2k_f}\right)}{1 - \left(\frac{k_s - k_f}{k_s + 2k_f}\right)(1-\varepsilon)} \right) \\ k_{eff,s} = k_s \end{cases} \tag{23}$$

2.3. Performance indicators

The thermal energy stored during the charging process (Q_C) is the total thermal energy stored during the effective charging time (t_C). Similarly, the thermal energy released during the discharging process (Q_D) is the total thermal energy released during the effective discharging time (t_D). The parameters Q_C and Q_D were calculated according to Eqs. 24 and 25, respectively (Li et al., 2018a).

$$Q_C = \int_0^{t \le t_C} \dot{m}\, C_{pf} \left(T_{f,in} - T_{f,out} \right) dt \tag{24}$$

$$Q_D = \int_0^{t \le t_D} \dot{m}\, C_{pf} \left(T_{f,out} - T_{f,in} \right) dt \tag{25}$$

The parameter t_C is defined as the time when the outlet temperature is lower than the cut-off temperature for charging ($T_{C,cut}$). Similarly, t_D is defined as the time when the outlet temperature is higher than the cut-off temperature for discharging ($T_{D,cut}$). The charging and discharging efficiencies (η_C and η_D) were calculated according to Eqs. 26 and 27, respectively, while the overall system efficiency (η) was calculated according to Eq. 28 (Mao and Cao, 2023).

$$\eta_C = \left(\frac{T_{f,in} - T_{f,out}}{T_{f,in} - T_{ini}} \right) \tag{26}$$

$$\eta_D = \left(\frac{T_{f,out} - T_{f,in}}{T_{ini} - T_{f,in}} \right) \tag{27}$$

$$\eta = \eta_C \, \eta_D \tag{28}$$

The second law efficiency or exergy efficiency (η_{ex}) of the PBTES can be determined by considering the maximum theoretical rate of work generated during the discharge, which is the exergy recovered in the discharging process, divided by the total exergetic content supplied during the charging process. This parameter was calculated as presented in Eqs. 29 to 31, respectively (Mao and Cao, 2023).

$$\eta_{ex} = \frac{E_{x,rec}}{E_{x,sup}} \tag{29}$$

$$E_{x,rec} = \int_0^{t \le t_D} \left[\dot{m}\, C_{pf} \left(T_{f,out} - T_{f,in} - T_w \ln\left(\frac{T_{f,out}}{T_{f,in}} \right) \right) \right] dt \quad (30)$$

$$E_{x,sup} = \int_0^{t \le t_C} \left[\dot{m}\, C_{pf} \left(T_{f,in} - T_{f,out} - T_w \ln\left(\frac{T_{f,in}}{T_{f,out}} \right) \right) \right] dt \quad (31)$$

The thermocline thickness (δ_T) is a measure that describes the temperature transition region in a PBTES. This region is characterized by an abrupt change in the temperature of the fluid in the bed, indicating the presence of a thermally stratified layer. This study calculated the thermocline thickness according to Eq. 32 (Li et al., 2018a).

$$\delta_T = \begin{cases} y(T_{up}) - 0, & T_{in} > T_{lo} \\ y(T_{up}) - y(T_{lo}), & T_{in} \le T_{lo} \; and \; T_{out} \ge T_{up} \\ H - y(T_{lo}), & T_{out} < T_{up} \end{cases} \quad (32)$$

The MIX number is a parameter that describes the thermal stratification of the PBTES at a specific point in time. Its value can range from 0 to 1, where 0 represents a fully stratified theoretical reservoir, and 1 represents a completely mixed reservoir. Equation 33 describes the calculation performed to evaluate the MIX number of the studied systems. The experimental energy moment (M_{exp}) was calculated according to Eqs. 34 and 35, the energy moment of the fully stratified reservoir (M_{str}) according to Eqs. 36 to 39, and the energy moment of the completely mixed reservoir (M_{mix}) according to Eqs. 40 and 41 (Liu et al., 2023).

$$MIX = \frac{M_{str} - M_{exp}}{M_{str} - M_{mix}} \quad (33)$$

$$EM_{exp} = \sum_{i=1}^{n} y_{ib}\; E_i \quad (34)$$

$$E_i = \rho_f\, C_{p,f}\, T_i\, V_i \quad (35)$$

$$EM_{str} = \sum_{i=1}^{n} y_{ib}\; E_{str,i} \quad (36)$$

$$E_{str} = \rho_f\, C_{p,f}\, T_{hot}\, V_{hot} + \rho_f\, C_{p,f}\, T_{cold}\, V_{cold} \quad (37)$$

$$V_T = V_{hot} + V_{cold} \quad (38)$$

$$V_{cold} = \pi\, \frac{D^2}{4}\, y_\delta \quad (39)$$

$$EM_{mix} = \sum_{i=1}^{n} y_{ib}\; E_{mix,i} \quad (40)$$

$$E_{mix} = \rho_f \, C_{p,f} \, T_{mix} \, V_i \tag{41}$$

The observed deviation between simulated results and experimental data was evaluated using the mean absolute percentage error (MAPE). This parameter was calculated according to Eq. 42. The dimensionless charging and discharging time (t*) and the dimensionless height of the PBTES (h*) were obtained according to Eqs. 43 and 44, respectively.

$$MAPE = \frac{1}{n}\sum_{i=1}^{n}\left|\frac{T_s - T_e}{T_e}\right| \tag{42}$$

$$t^* = \frac{t}{t_{\frac{C}{D}}} \tag{43}$$

$$h^* = \frac{x}{H} \tag{44}$$

2.4. Numerical method and mesh independence test

The governing equations were solved using the finite volume method in Ansys Fluent software version 23.1. The coupling between pressure and velocity was resolved using the SIMPLE (Semi-Implicit Method for Pressure Linked Equations) algorithm. The energy and momentum equations were discretized using the second-order upwind scheme. A time step of 1s and a maximum of 20 iterations per interval were used for the simulation. The convergence criterion for the continuity and momentum equations in each time interval was a root mean square residue (RMS) lower than 10^{-4}, while for the energy equation was RMS lower than 10^{-6}.

In this study, a mesh consisting of hexahedral cells was used for the discretize the computational domain (Fig. 3A). Mesh independence tests were performed to assess the quality and accuracy of the mesh, ensuring the independence of the results from spatial discretization errors. For this purpose, successive refinements in the mesh were performed, and the variation of fluid temperature at a central point in the PBTES was monitored and compared. The results of the mesh independence test are shown in Figure 3B. It can be observed that the numerical results converge to a stable value as the mesh resolution increases. Once the number of grids reaches 10187, further refinement has no significant influence on the simulation results. Therefore, considering the calculation accuracy and simulation time, mesh with 10187 cells was used for subsequent simulations.

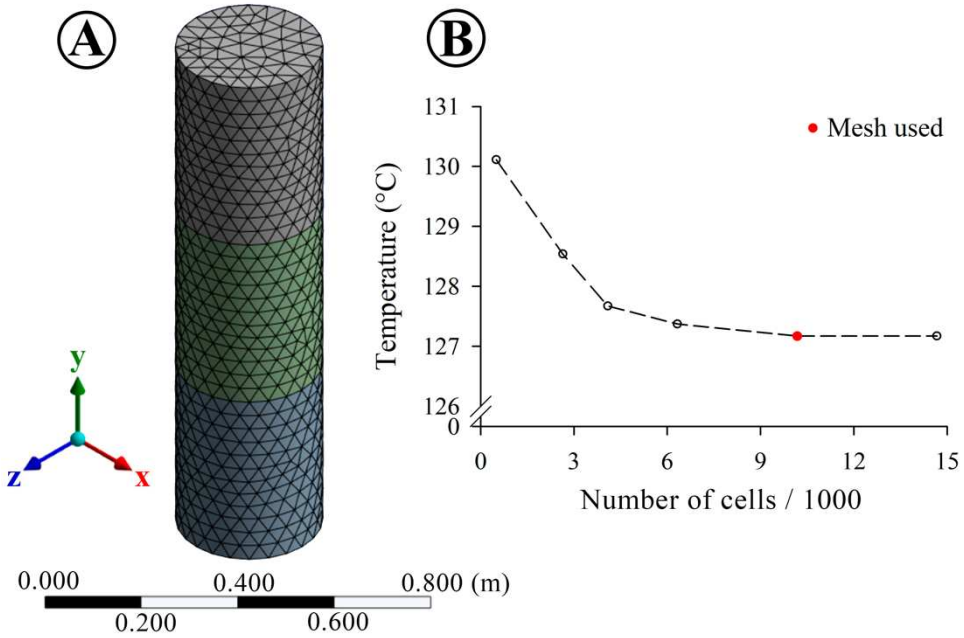

Fig. 3. (A) Distribution of cells in the selected mesh for the computational domain, and (B) mesh independence test.

3. SENSITIVITY ANALYSIS AND MODEL VALIDATION

The experimental data from Kocak and Paksoy (2020) were used in the sensitivity analysis and validation of the model developed in this study. The authors evaluated the performance of a sensible heat PBTES using a new material for heat storage during the charging and discharging process. The experimental system consisted of an insulated PBTES with a height of 0.9 m and a diameter of 0.3 m. Thermal oil was used as the heat transfer fluid (HTF), and demolition waste particles with a diameter of 0.01 m were used as the storage medium. The charging and discharging temperatures and the HTF inlet velocity were set to 150 °C, 24 °C, and 0.00095 m s^{-1}, respectively. Further details for the experimental conditions can be found in Kocak and Paksoy (2020).

The effect of using different correlations for h_{fs} and k_{eff} on the simulated temperature profiles of the storage material during the charging process can be observed in Fig. 4. The experimental temperature profile obtained by Kocak and Paksoy (2020), as well as the MAPE values, are also presented. It can be observed that the temperatures simulated by the $k_{eff}(C_2)$ and $k_{eff}(C_4)$ models experience a rapid increase between 0.1 and 0.3 of h* followed by stabilization. This behavior occurs for all h_{fs}, except for $h_{fs}(C_3)$. For the other k_{eff} models, temperatures gradually increase along the height of the PBTES for all evaluated h_{fs} models. Among the different h_{fs} models, correlation C_4 shows the most considerable deviations between simulated

and experimental values for almost all k_{eff} models (Fig. 4D). Among the k_{eff} models, the highest MAPE values were observed for correlations C_2 and C_4. The MAPE values ranged between 3.1% and 11.3% for the intrinsic thermal conductivities of the materials (k_f, k_s), 3.3% and 18.0% for $k_{eff}(C_1)$, 2.4% and 24.5% for $k_{eff}(C_2)$, 3.6% and 21.9% for $k_{eff}(C_3)$, 3.1% to 24.6% for $k_{eff}(C_4)$, and 4.0% and 7.4% for $k_{eff}(C_5)$. The simulated temperature profile that most accurately represented the experimental thermal behavior was obtained by combining $h_{fs}(C_3)$ and $k_{eff}(C_2)$. It should also be noted that, except for $h_{fs}(C_3)$, the use of k_{eff} correlations decreases the accuracy of the models. This fact is supported by the lower MAPE values obtained for the models that use the intrinsic thermal conductivities of the materials (k_f, k_s). Furthermore, the results obtained confirm that the type of correlation used to calculate h_{fs} and k_{eff} significantly affect the model performance. This highlights the importance of such analyses in numerical simulation studies.

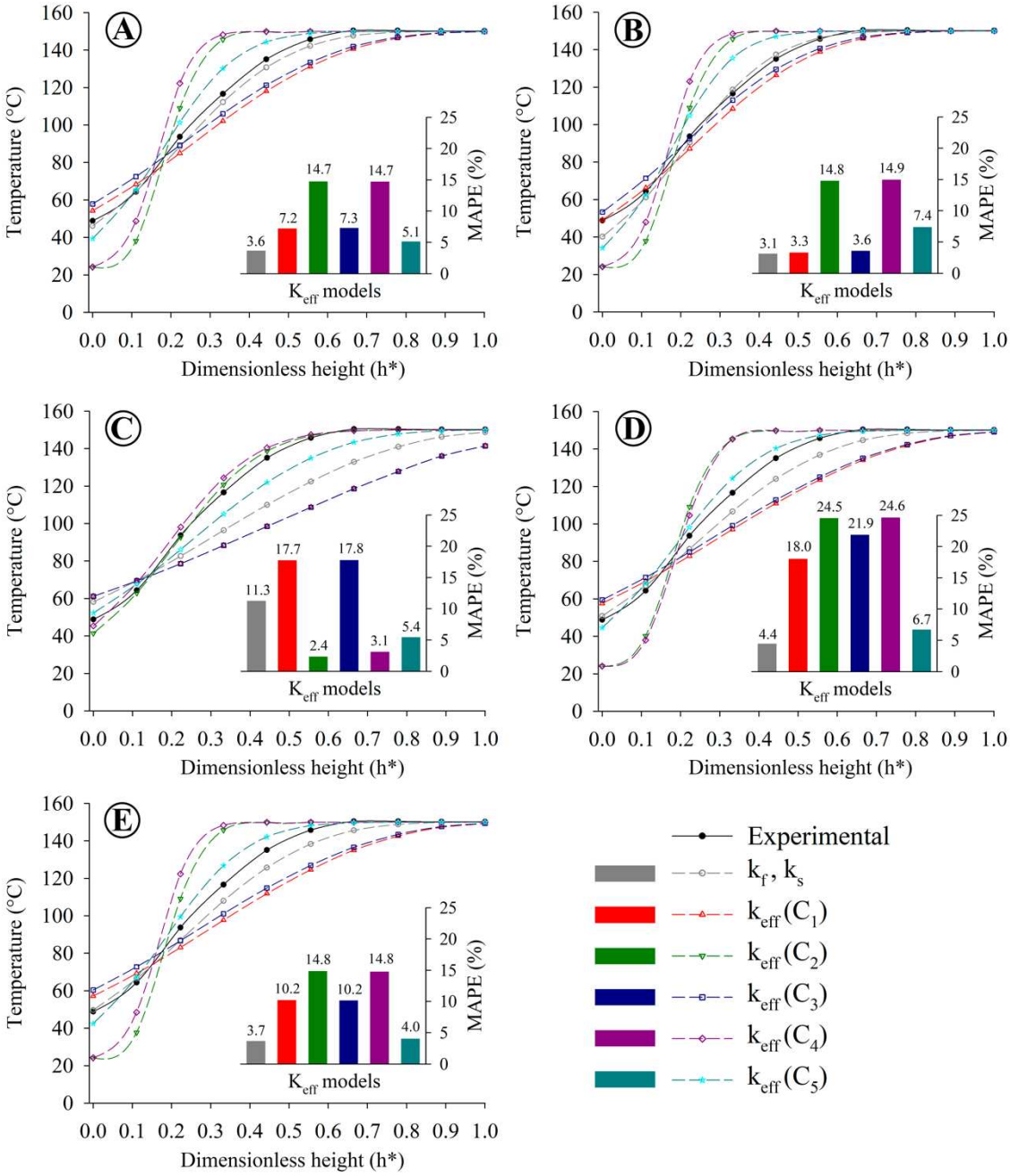

Fig. 4. Experimental temperature of the storage material, simulated temperatures, and MAPE for different k_{eff} correlations along the PBTES during the charging process for (A) $h_{fs}(C_1)$, (B) $h_{fs}(C_2)$, (C) $h_{fs}(C_3)$, (D) $h_{fs}(C_4)$, and (E) $h_{fs}(C_5)$.

As presented in the sensitivity analysis, using the third correlation (C_3) for calculating h_{fs} (Eq. 16) and the second correlation (C_2) for calculating $k_{eff,f}$ and $k_{eff,s}$ (Eq. 20) provided the lowest MAPE value among all the combinations (2.4%, Fig. 4B). Therefore, these correlations were selected to be used in subsequent analyses. Figure 5 compares experimental and numerical results of the temperature of the storage material along the PBTES during the charging and

discharging process. The observed MAPE values were 2.41% for the charging process and 6.63% for the discharging process. The results confirm the accuracy of the model, as it adequately predicted the thermal behavior of the evaluated PBTES.

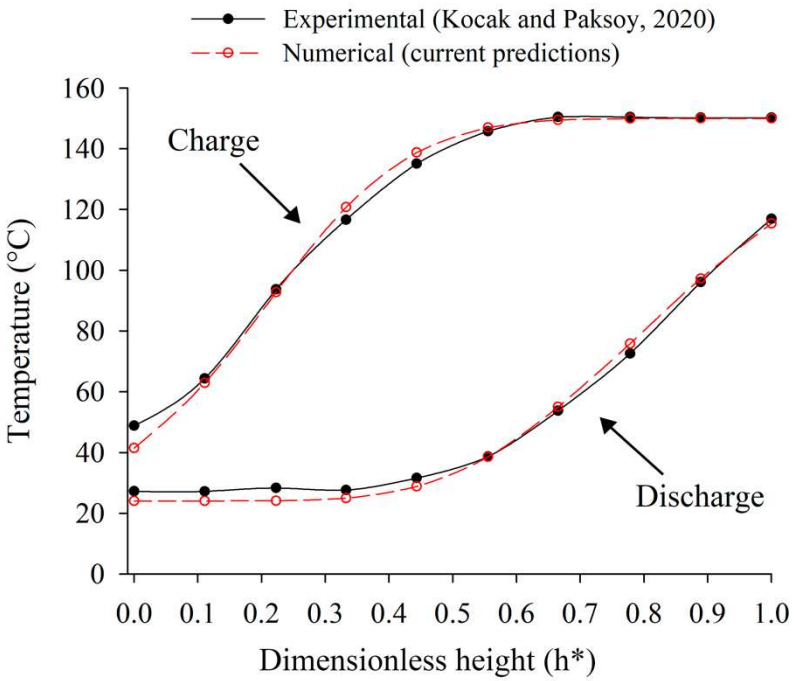

Fig. 5. Temperature of the storage material along the PBTES during the charging and discharging process: experimental and numerical results.

4. RESULTS AND DISCUSSION

Temperature profiles of the fluid and solid along the reservoir during the charging process are presented in Fig. 6. The temperature difference between the fluid and the solid phases ($\Delta T_{f\text{-}s}$) is also shown. The results are plotted at different times throughout the heat transfer process. As expected, the temperature at the reservoir outlet (h* = 1.00) increases until it reaches the predetermined cut-off temperature for charging. Analyzing the first three cases (Fig. 6A, 6B, and 6C), it can be observed that the particle diameter directly influences the heat transfer rate in the solid material. When reaching the layer with solid material of diameter 0.04 m, $\Delta T_{f\text{-}s}$ increases rapidly. This result is attributed to the reduction in specific surface area for heat exchange (Eq. 10) due to the increase in particle diameter. For cases 4 and 5 (Fig. 6D and 6E), the layer composed of concrete presents the highest $\Delta T_{f\text{-}s}$, demonstrating that material properties such as thermal conductivity also influence the system charging. The effects of particle diameter and thermal conductivity of the solid material are also observed in the other

cases. Therefore, the highest ΔT_{f-s} values were observed for layers composed of concrete (lower thermal conductivity among the materials) with particles of 0.04 m in diameter. Conversely, the smallest variations are observed for layers composed of cast iron (higher thermal conductivity among the materials) with particle diameter of 0.02 m. Taking two cases as an example, cases 7 (Fig. 6G) and 8 (Fig. 6H) presented the highest and lowest ΔT_{f-s} in the first layer of the reservoir during the charging process, respectively. At the end of the height of the first layer (0.33 h*), the temperatures were 46.7 and 25.1 °C for 0.13 t* and 109.5 and 83.0 °C for 0.36 t* for cases 7 and 8, respectively. This indicates that heat transfer occurs more efficiently in case 8, as the solid material absorbs a more significant amount of the available heat throughout the first layer.

The temperature profiles of the fluid and solid along the reservoir and ΔT_{f-s} during the discharge process are presented in Fig. 7. In the discharge process, h* equal to zero represents the entry of cold fluid. Similarly, increasing the particle diameter from 0.02 to 0.04 m results in a higher temperature difference between the solid and the fluid (Fig. 7B and 7C), for the same solid material. Evaluating cases with fixed particle diameters, higher ΔT_{f-s} values were observed for layers of concrete. This result is related to the thermal properties of the material, as concrete has the lowest thermal conductivity. On the other hand, layers composed of cast iron showed the lowest ΔT_{f-s} values, regardless of their position in the reservoir. Analyzing the combined effect of particle diameter and layer material, it can be observed that, in general, cases 6 (Fig. 7F) and 9 (Fig. 7I) exhibited the lowest ΔT_{f-s} values. The results indicate that for materials with lower thermal conductivity (concrete), heat transfer can be adjusted by increasing the specific surface area for heat exchange using smaller particles. In this way, it is possible to achieve more homogeneous temperature profiles between the fluid and the solid during the discharge process.

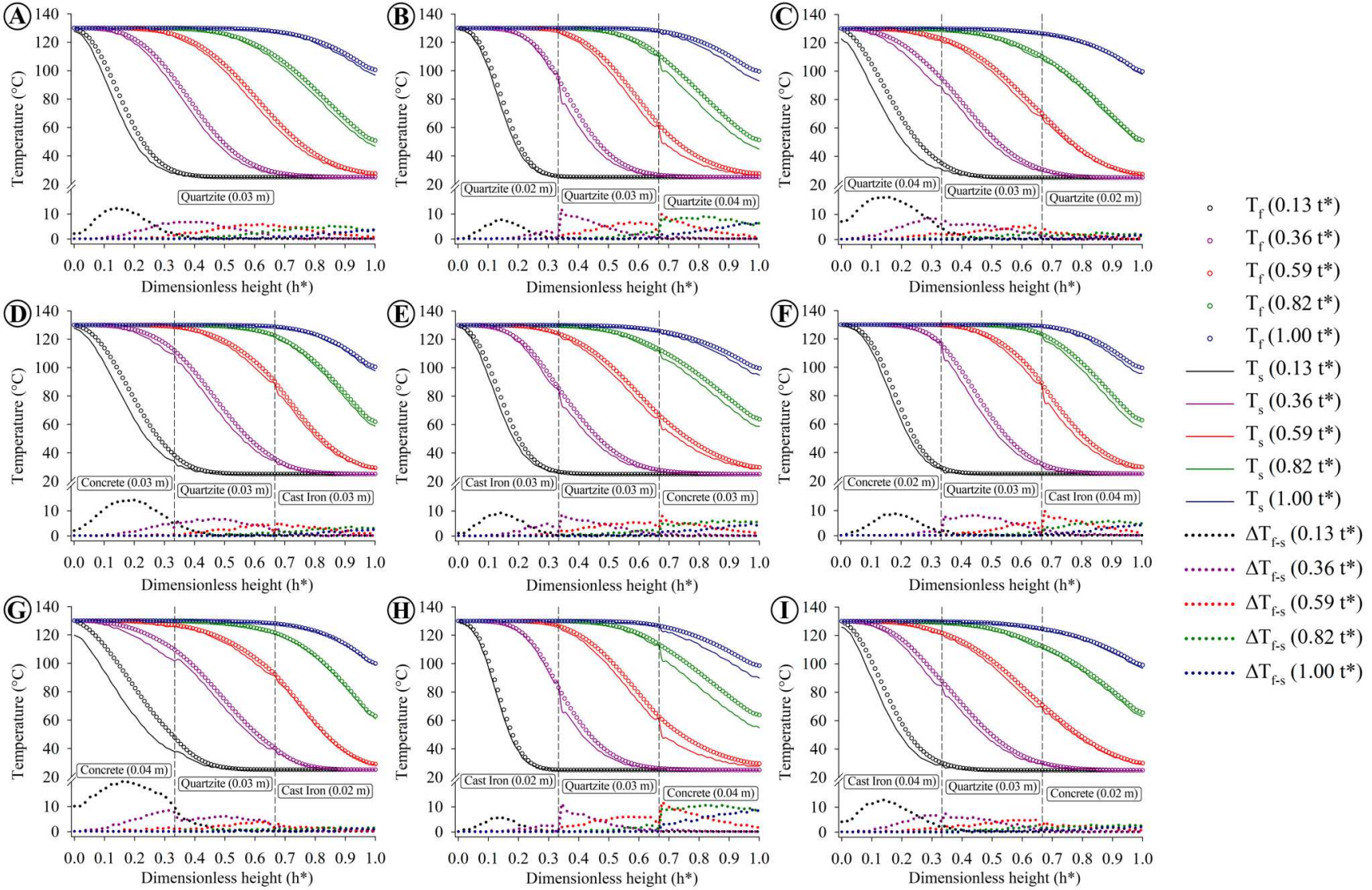

Fig. 6. Temperature profiles along h* for different t* during the charging process for (A) case 1, (B) case 2, (C) case 3, (D) case 4, (E) case 5, (F) case 6, (G) case 7, (H) case 8, and (I) case 9.

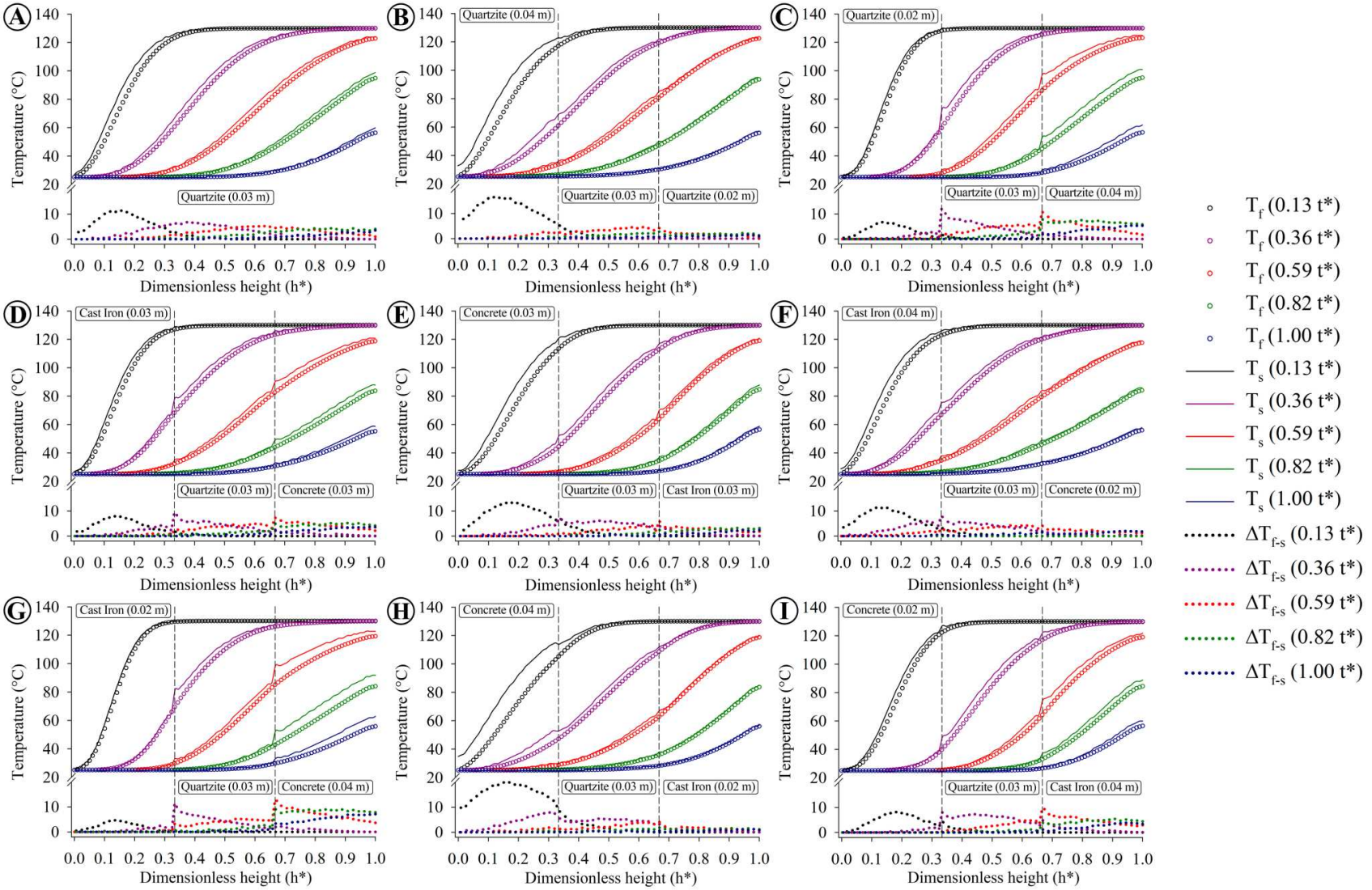

Fig. 7. Temperature profiles along h* for different t* during the discharging process for (A) case 1, (B) case 2, (C) case 3, (D) case 4, (E) case 5, (F) case 6, (G) case 7, (H) case 8, and (I) case.

The effective charging and discharging times (t_C and t_D) of the PBTES are presented in Table 2. The maximum variation between the charging and discharging times was 5.4% and 4.5%, respectively. The shortest and longest charging times were observed for cases 3 and 6, which were 7442 and 7884 seconds, respectively. For discharging, these values were 7462 and 7799 seconds for cases 2 and 9, respectively. It can be observed that the use of different materials in the multilayer configurations increased the charging and discharging times compared to the single-material cases. However, the effect of particle diameters on the charging and discharging times was not evident.

Table 2. PBTES charging and discharging times for the evaluated cases

Case	Charging time (s)	Discharging time (s)
1	7503	7490
2	7539	7462
3	7442	7502
4	7804	7729
5	7749	7797
6	7844	7669
7	7740	7755
8	7797	7771
9	7671	7799

The variations in stored thermal energy during the charging process (Q_C) and released thermal energy during the discharging process (Q_D) are presented in Fig. 8. It can be observed that compared to case 1, an increase in the values of Q_C and Q_D is observed for cases 4 and 5, contrary to observed for cases 2 and 3. This indicates that using multilayers with different materials in the PBTES is more effective for energy gain than using layers with different particle diameters for a single material. Furthermore, the combined use of multilayers with variable particle diameters (cases 6 to 9) demonstrates a favorable effect, as indicated by the higher values of Q_C and Q_D compared to the other cases. Cases 4 to 9 presented similar values of Q_D, ranging from 26.2 to 26.4 MJ. These values are higher than those presented by cases 1 to 3. Based on these results, it can be stated that using multilayers of materials for the discharging process increases the released energy by at least 3.4% when compared to the single-material PBTES. Considering Q_C, case 9 presented the highest value among all the evaluated cases, which was 27.2 MJ. This value was approximately 7.7% higher than that for the single-

material and diameter reservoir (case 1) and approximately 2.6% higher than the reservoir with the same material configuration and single diameter (case 5).

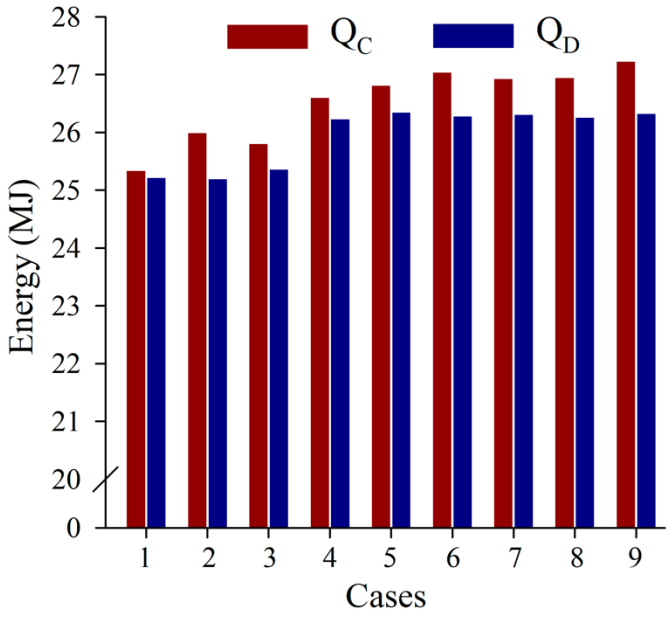

Fig. 8. Stored thermal energy during the charging process (Q_C) and released thermal energy during the discharging process (Q_D).

The charging and discharging efficiencies, overall efficiency, and exergy efficiency of the PBTES are presented in Fig. 9. It can be observed that case 9 exhibited the highest values for charging (87.5%) and discharging efficiency (80.5%), when compared to the other cases. Case 9 showed a charging and discharging efficiencies of 9.5% and 4.0% higher, respectively, than the reference case (case 1). Compared to the cases with a single-material PBTES, an increase in both charging and discharging efficiencies was observed for all cases with multilayer configurations using different materials. This indicates that utilizing different materials in the multilayer configuration enhances heat transfer and improves the efficiency of the PBTES. The results indicate that the discharging process generally exhibits lower efficiency than the charging process, regardless of the PBTES configuration. This behavior has been observed in previous studies on PBTES with different configurations and thermal storage materials (Li et al., 2018a; Mao and Cao, 2023). The overall efficiency of the system followed a similar pattern as the charging and discharging efficiencies. The reference case (case 1) had the lowest overall efficiency at 61.9%, while case 9 exhibited the highest overall efficiency at 70.5%. This indicates that case 9 achieved the highest efficiency in terms of both charging and discharging processes, making it the most efficient configuration among the cases evaluated.

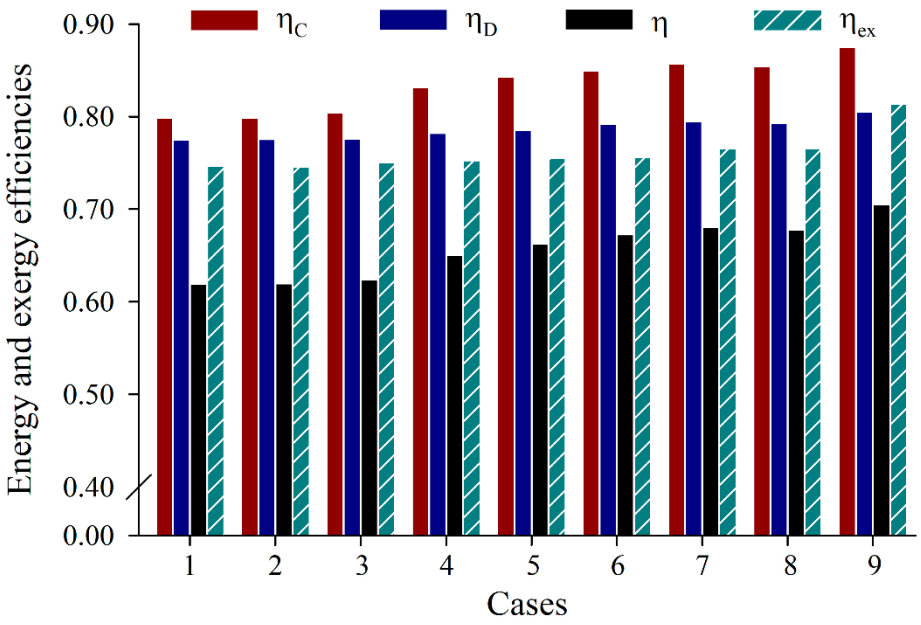

Fig. 9. Charging and discharging (η_C, η_D), energy (η), and exergy (η_{ex}) efficiencies of the PBTES.

According to Saha and Das (2020), the evaluation of the thermodynamic performance of a TES using the exergy principle is necessary to quantify the amount of available useful work. Case 9 exhibited the highest overall exergy efficiency, indicating better performance according to the second law of thermodynamics. The observed exergy efficiency in case 9 is approximately 9.0% higher than in the reference case (case 1). Furthermore, it is approximately 7.7% higher than case 5, which has the same configuration in terms of storage materials and equal diameters for all layers. This result indicates that the particle diameter also influences the thermal performance of the PBTES from the perspective of the second law. Huan et al. (2020) reported that in PBTES with sensible heat storage, higher energy density results in greater exergy recovery, although not all stored energy can be converted into useful work due to system entropy and irreversibilities (Koholé et al., 2022).

The results of the thermocline thickness (δ_T) for the charging and discharging processes of the PBTES are presented in Fig. 10. It can be observed that for both cases, δ_T increases until reaching a maximum at 50-55% ($t^* = 0.50$-0.55) of the charging or discharging time. Similar results were reported by Guo et al. (2021) for a PBTES of latent heat. The reservoir is homogeneous at the beginning of each process, so there is no temperature gradient, and thus no thermocline thickness. As the charging and discharging processes progress, a heat exchange front is formed, leading to an increase in the thermocline thickness. It should be noted

that a thin thermocline is desirable as it indicates better thermal exchange in the system. Subsequently, a reduction in δ_T is observed as part of the fluid has either released (charging) or absorbed (discharging) enough heat to become a homogeneous layer. For the charging process, it can be observed that the maximum values for all cases varied between 60% and 80% of the total height of the reservoir (Fig. 10A). The highest δ_T values occurred for cases 5 and 8, with values of 80.4% and 74.4% of the PBTES height, respectively. For the discharging process, the highest δ_T values were observed for cases 6 and 2, representing 87.6% and 86.4% of the total height of the PBTES, respectively (Fig. 10B).

According to Huan et al. (2020), the thermocline thickness is highly dependent on the HTF inlet temperature, the type of heat storage material, the length of the PBTES, and the temperature difference for heat transfer. The results indicate that during the charging process, the position of particles with smaller diameters and materials with lower thermal conductivity at the top of the PBTES leads to a lower maximum value of the thermocline thickness. This occurs because using materials with higher thermal conductivities promotes heat transfer by diffusion. When the contribution of heat transfer by diffusion is increased, thermal energy spreads more gradually, resulting in thicker temperature gradients. Based on the obtained results, it can be stated that the PBTES with concrete (0.02 m), quartzite rock (0.03 m), and cast iron (0.04 m) provided smaller temperature gradients within the PBTES. This is evidenced by the observation that the lowest average values of δ_T were observed for cases 6 (0.37 m) and 9 (0.40 m) for the charging and discharging processes, respectively. It is worth noting that during the discharging process, the flow direction is reversed. Therefore, cases 6 (charging) and case 9 (discharging) have the same configuration in relation to the HTF inlet.

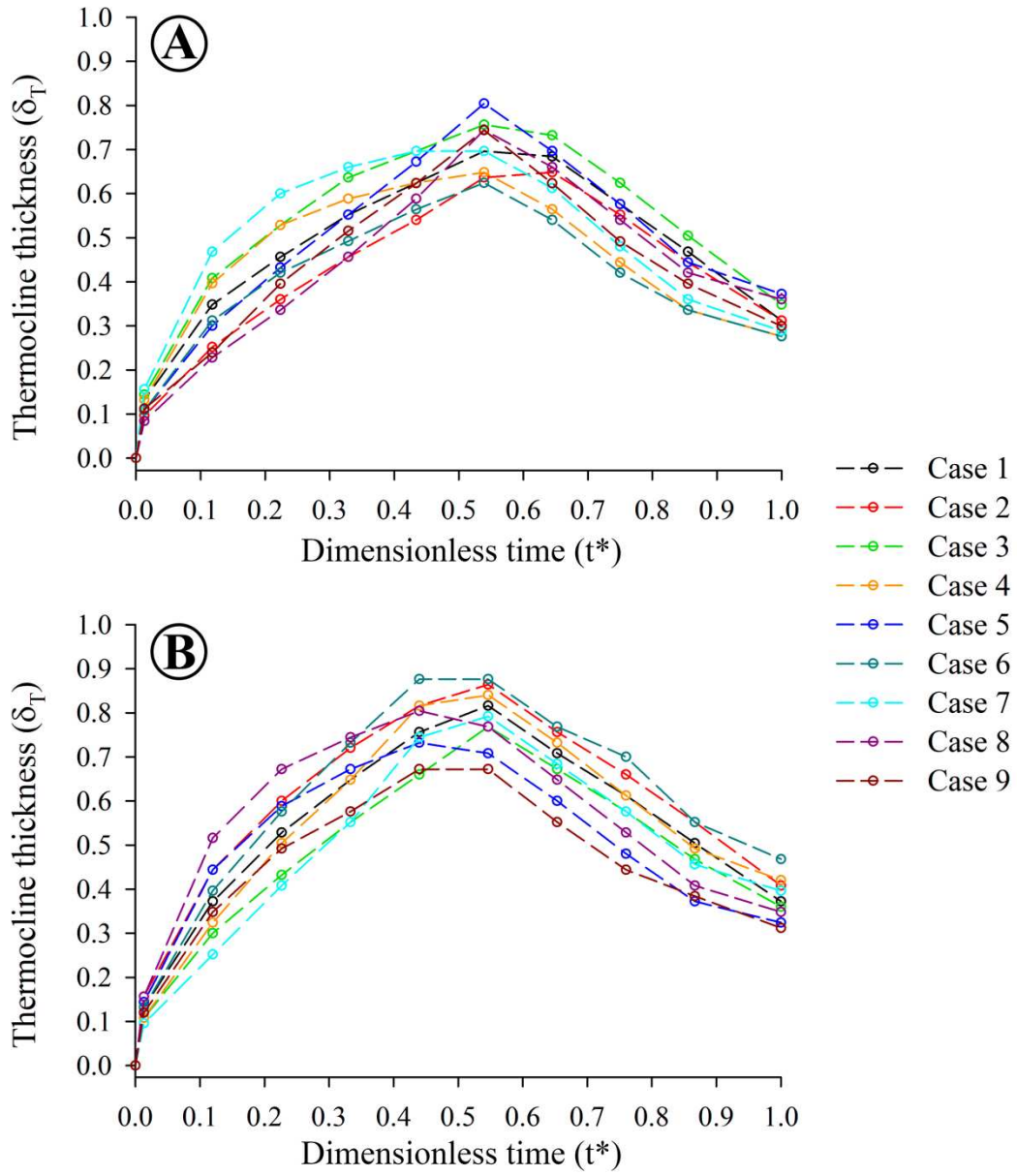

Fig.10. Variation of the thermocline thickness along dimensionless time (t*) for (A) charging and (B) discharging processes.

The variations of the MIX numbers along the dimensionless time (t*) for the charging and discharging processes are presented in Fig. 11. It can be observed that, both for charging and discharging, the MIX number shows similar trends, initially decreasing and then increasing with the increase in t*. This behavior is commonly observed in stratified reservoirs during heat transfer processes (Huang et al., 2019; Liu et al., 2023). Before starting the charging and discharging processes (t*=0), the MIX number for all cases is equal to 1, indicating a homogeneous temperature distribution within the PBTES. When the processes are initiated, the hot/cold HTF flows from the inlet to the outlet, disrupting the initial temperature uniformity

and forming thermal stratification. This leads to a decrease in the MIX number. The moment when the PBTES exhibits the highest temperature gradient is at t*≈ 0.1 for all evaluated cases. At this moment, the lowest values of the MIX number are observed, ranging between 0.15 and 0.19 for charging and 0.16 and 0.17 for discharging. As the charging time increases, the mass of hot/cold HTF flowing into the reservoir increases, intensifying the internal heat transfer. Consequently, the temperature of each layer tends to be equalized, reducing the thermal stratification and increasing the MIX number over time until it reaches its maximum value at t*=1.

For case 6 in the charging process and case 9 in the discharging process, the MIX number remains below 0.5 for approximately 43% of the total charging/discharging time. This time is about 10% higher than in case 1 in both processes. As expected, the highest values of the MIX number for the charging and discharging processes were obtained at t*=1, being 0.77 and 0.79 for case 1, 0.75 and 0.82 for case 2, 0.80 and 0.81 for case 3, 0.76 and 0.78 for case 4, 0.80 and 0.77 for case 5, 0.74 and 0.83 for case 6, 0.79 and 0.80 for case 7, 0.78 and 0.79 for case 8, and 0.77 and 0.75 for case 9, respectively. These values are lower than those reported by Huang et al. (2019), who investigated using phase change materials in PBTES.

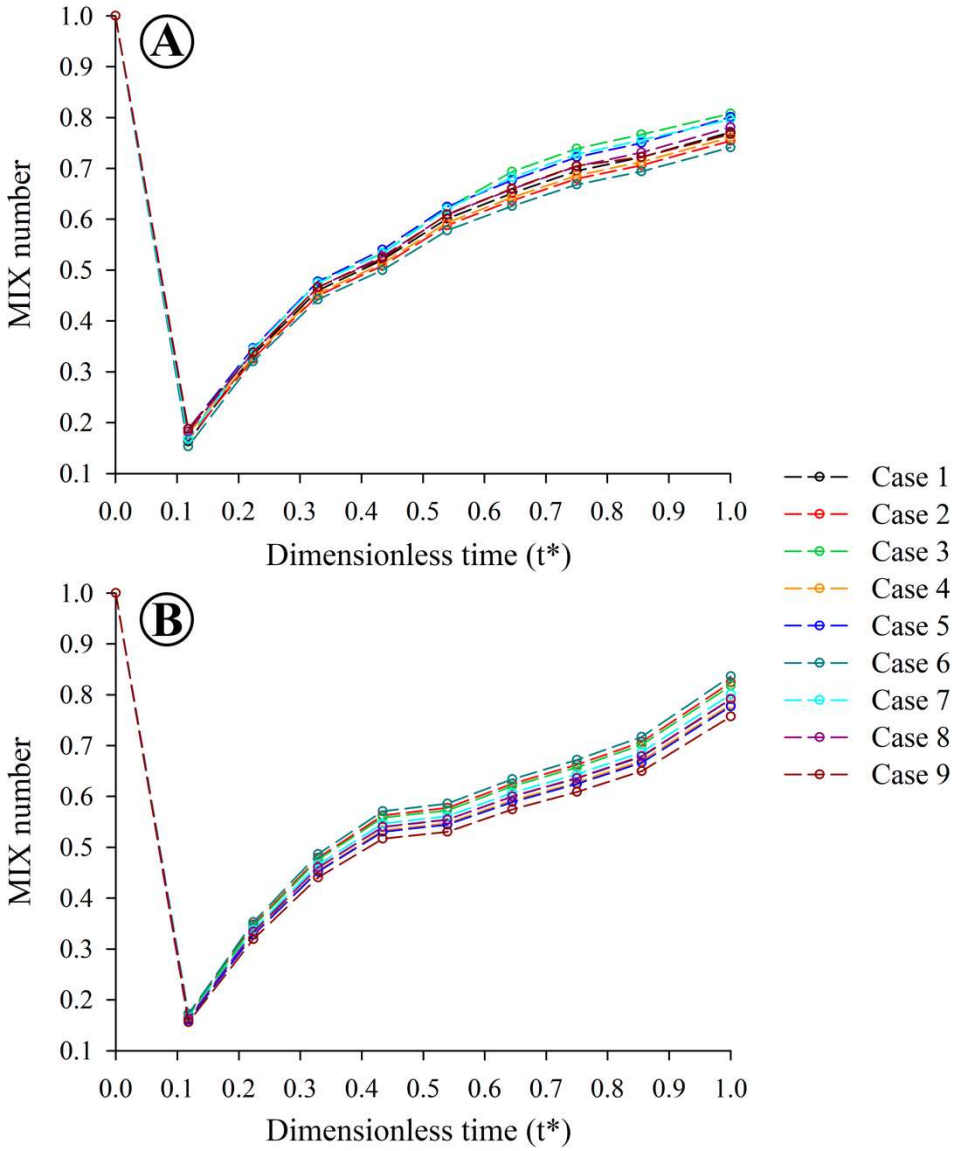

Fig. 11. Variation of the MIX numbers along t* for (A) charging and (B) discharging processes.

5. CONCLUSION

This study investigated by modeling and simulation the effect of different heat storage materials and particle sizes on the performance of a sensible heat packed bed thermal energy storage (PBTES) system. The numerical model used in this study was validated after a sensitivity analysis, which helped identify the most suitable correlations for heat transfer coefficient and effective thermal conductivity. The selected model exhibited the lowest mean absolute percentage error (MAPE) values, ensuring the accuracy of subsequent analyses. Based on the obtained results, the following main conclusions can be drawn:

- Particle diameter significantly affected packed bed temperature during charge and discharge cycles, influenced by heat exchange surface area. Lower thermal conductivity materials increase temperature difference between HTF and solid material.
- The use of different materials in multilayer configurations increased the charging and discharging times compared to the single material cases. However, the effect of particle sizes on the final times was not as evident.
- The multilayer configuration had a stronger impact on stored (Q_C) and released (Q_D) thermal energy than particle diameter. Combining varying particle sizes in multilayers, as in Case 9, yielded around 7.7% and 3.4% increases in Q_C and Q_D compared to a single material and diameter reservoir (Case 1).
- Contrasted with single-material PBTES cases, configurations using varied material layers showcased enhanced charging and discharging as well as overall system efficiency. Case 9 demonstrated roughly 9.5%, 4.0%, and 13.9% higher efficiencies in charging, discharging, and the overall system, respectively, compared to Case 1.
- The multilayer configuration and variable particle diameter influence the thermal performance of the PBTES from a second law perspective. The exergetic efficiency observed in case 9 was approximately 9.0% higher than that observed in case 1. Furthermore, it is approximately 7.7% higher than case 5, which has the same configuration regarding the storage materials and equal diameters for all layers.
- The thermal performance of the PBTES is influenced by multilayer design and variable particle diameter from a second law perspective. Case 9 showed approximately 9.0% higher exergetic efficiency than Case 1, and roughly 7.7% higher than Case 5 with the same material configuration and uniform layer diameters.
- Cases 6 for charging and 9 for discharging, composed of the same configuration related to the HTF inlet, namely concrete (0.02 m), quartzite rock (0.03 m), and cast iron (0.04 m), provided lower temperature gradients in the PBTES and generally had the smallest values for the thermocline thickness. Additionally, MIX number remained below 0.5 for about 43% of the total charging/discharging time, roughly 10% longer than observed in Case 1 for both processes.

6. REFERENCES

Al-Azawii M.M.S., Alhamdi, S.F.H., Braun, S., Hoffmann, J., Calvet, N., Anderson, R. **Journal of Energy Storage**, v.44, Part A, 103375, 2021.

Alptekin, E., Ezan, M.A. Performance investigations on a sensible heat thermal energy storage tank with a solar collector under variable climatic conditions. **Applied Thermal Engineering**, v.164, 114423, 2020.

Barbosa, E.G., Araujo, M.E.V., Oliveira, A.C.L., Martins, M.A. Thermal energy storage systems applied to solar dryers: Classification, performance, and numerical modeling: An updated review. **Case Studies in Thermal Engineering**, v.45, 102986, 2023.

Calderón-Vásquez, I., Cortés, E., García, J., Segovia, V., Caroca, A., Sarmiento, C., Barraza, R., Cardemil, J.M. Review on modeling approaches for packed-bed thermal storage systems. **Renewable and Sustainable Energy Reviews**, v.143, 110902, 2021.

Chekifi, T., Boukraa, M. CFD applications for sensible heat storage: A comprehensive review of numerical studies. **Journal of Energy Storage**, v.68, 107893, 2023.

Chen, Y., Guo, M., Liu, Y., Wang, D., Zhuang, Z., Quan, M. Energy, exergy, and economic analysis of a centralized solar and biogas hybrid heating system for rural areas. **Energy Conversion and Management**, v.275, 116591, 2023.

Días-Heras, M., Belmonte, J.F., Almendros-Ibáñez, J.A. Effective thermal conductivities in packed beds: Review of correlations and its influence on system performance. **Applied Thermal Engineering**, v.171, 115048, 2020.

Dixon, A.G. Correlations for wall and particle shape effects on fixed bed bulk voidage. **The Canadian Journal of Chemical Engineering**, v.66, p.705-708, 1988.

Elsihy, E.S., Liao, Z., Xu, C., Du, X. Dynamic characteristics of solid packed-bed thermocline tank using molten-salt as a heat transfer fluid. **International Journal of Heat and Mass Transfer**, v.165, Part A, 120677, 2021.

Ergun, S. Fluid flow through packed columns. **Chemical Engineering Progress**, v.48, p.89-94, 1952.

Gautam, A., Saini, R.P. A review on sensible heat based packed bed solar thermal energy storage system for low temperature applications. **Solar Energy**, v.207, p.937-956, 2020.

Guo, W., He, Z., Meng, Z., Zhang, P. A comprehensive investigation of the mathematical models for a packed bed latent heat thermal energy storage system. **International Journal of Energy Research**, v.45, p.15005-15021, 2021.

Huan, G., Yujie, X., Cong, G., Haisheng, C., Yifei, W., Zheng, Y., Ye, H., Binlin, D. Thermodynamic Analysis of Packed Bed Thermal Energy Storage System. **Journal of Thermal Science**, v.29, p.445-456, 2020.

Huang, H., Wang, Z., Zhang, H., Dou, B., Huang, X., Liang, H., Goula, M.A. An experimental investigation on thermal stratification characteristics with PCMs in solar water tank. **Solar Energy**, v.177, p.8-21, 2019.

IEA – **International Energy Agency. Technology Roadmap: Concentrating Solar Power**. OECD/IEA, France, 2010. 52p.

Kocak, B., Paksoy, H. Performance of laboratory scale packed-bed thermal energy storage using new demolition waste based sensible heat materials for industrial solar applications. **Solar Energy**, v.211, p.1335-1346, 2020.

Koholé, Y.W., Fohagui, F.C.V., Tchuen, G. Flat-plate solar collector thermal performance assessment via energy, exergy and irreversibility analysis. **Energy Conversion and Management: X**. v.15, 100247, 2022.

Li, M.-J., Jin, B., Yan, J.-J., Ma, Z., Li, M.-J. Numerical and Experimental study on the performance of a new two-layered high-temperature packed-bed thermal energy storage system with changed-diameter macro-encapsulation capsule. **Applied Thermal Engineering**, v.142, p.830-845, 2018b.

Li, M.-J., Qiu, Y., Li, M.-J. Cyclic thermal performance analysis of a traditional Single-Layered and of a novel Multi-Layered Packed-Bed molten salt Thermocline Tank. **Renewable Energy**, v.118, p.565-578, 2018a.

Liu, Y.-G., Zhang, J.-Y., Li, H.-J., Ji, Q.-Y., Zhou, Q. Numerical study on stratification performance of cascaded three-layered packed-bed in the thermal storage process. **Applied Thermal Engineering**, v.219, Part C, 119669, 2023.

Lugolole, R., Mawire, A., Lentswe, K.A., Okello, D., Nyeinga, K. Thermal performance comparison of three sensible heat thermal energy storage systems during charging cycles. **Sustainable Energy Technologies and Assessments**, v.30, p.37-51, 2018.

Ma, Z., Li, M.-J., Zhang, K.M., Yuan, F. Novel designs of hybrid thermal energy storage system and operation strategies for concentrated solar power plant. **Energy**, v.216, 119281, 2021.

Mao, Q., Cao, W. Effect of variable capsule size on energy storage performances in a high-temperature three-layered packed bed system. **Energy**, v.273, 127166, 2023.

Martí, J., Geissbuhler, L., Becattini, V., Haselbacher, A., Steinfeld, A. Constrained multi-objective optimization of thermocline packed-bed thermal-energy storage. **Applied Energy**, v.216, p.694-708, 2018.

Mehos, M., Turchi, C., Vidal, J., Wagner, M., Ma, Z., Ho, C., Kolb, W., Andraka, C., Kruizenga, A. **Concentrating solar power Gen3 demonstration roadmap**. National Renewable Energy Lab. (NREL), Golden, CO (United States), 2017.

Palomba, V., Frazzica, A. Application of numerical methods for the design of thermocline thermal energy storage: Literature review and critical analysis. **Journal of Energy Storage**, v.46, 103875, 2022.

Saha, S.K., Das, R.B. Exergetic and performance analyses of two-layered packedbed latent heat thermal energy storage system. **International Journal of Energy Research**, v.44, p.2208-2225, 2020.

Seyitini, L., Belgasim, B., Enweremadu, C.C. Solid state sensible heat storage technology for industrial applications – A review. **Journal of Energy Storage**, v.62, 106919, 2023.

SunShot. SunShot **Vision Study, Energy Efficiency and Renewable Energy**. U.S. Department of Energy (2012). NREL Report No. BK5200-47927; DOE/GO-102012-3037.

Türkakar, G. Performance analysis and optimal charging time investigation of solar air heater with packed bed sensible heat storage device. **Solar Energy**, v.224, p.718-729, 2021.

Xu, C., Wang, Z., He, Y., Li, X., Bai, F. Sensitivity analysis of the numerical study on the thermal performance of a packed-bed molten salt thermocline thermal storage system. **Applied Energy**, v.92, p.65-75, 2012.

Zhou, H., Lai, Z., Cen, K. Experimental study on energy storage performances of packed bed with different solid materials. **Energy**, v.246, 123416, 2022.

Zhu, Y., Wang, D., Li, P., Yuan, Y., Tan, H. Optimization of exergy efficiency of a cascaded packed bed containing variable diameter particles. **Applied Thermal Engineering**, v.188, 116680, 2021.

GENERAL CONCLUSION

In this study, different types of dryers were addressed and the importance of thermal energy storage methods was emphasized. The importance of computational numerical modeling for heat and mass transfer in drying systems and thermal energy storage was also presented. Furthermore, the thermal and economic performance of a U-tube CPC was experimentally evaluated. Different filling fluids of the evacuated tube and different mass flowrates were evaluated. A detailed energy analysis was carried out for the different components of the collector. In the final topic, a sensible heat thermal storage system was numerically evaluated using CFD. A thermal non-equilibrium model was implemented to evaluate the charge and discharge of heat from the thermal reservoir. An optimization of this system was carried out evaluating different heat storage materials and different particle sizes. In view of the results obtained, the following conclusions can be cited:

- The search for more efficient dryers has become crucial nowadays due to the high energy and time consumption of this operation. In this scenario, dryers based on solar energy have gained more and more space because their energy efficiency can surpass that of conventional sources.
- Solar technologies are promising, however solar intermittency is still a bottleneck. Therefore, several researchers are currently focusing their research on thermal energy storage systems. The advancement of computers has allowed numerical evaluation of these systems in different configurations and operations, and has made them increasingly efficient.
- The highest temperature gains for all evaluated cases were observed around noon when the highest solar radiation values were recorded. The use of air as the FF resulted in the highest temperature inside the evacuated tube, followed by oil and water. Furthermore, increasing the mass flowrate of the heat transfer fluid (HTF) caused a significant reduction in temperature gain.
- The type of FF used considerably influences the thermal performance of the CPC. An increase of approximately 30.0% and 32.5% in thermal efficiency values was observed when thermal oil was used as the FF, compared to water and air, respectively. It can also be stated that an increase in the flow rate of the working fluid decreases the thermal efficiency of the CPC. A reduction of up to 36.2% was observed with increasing flow rate.

- For all evaluated hours, thermal oil as the FF provided the best condition for solar energy absorption. It can also be affirmed that during hours with lower solar incidence, this fluid transferred the absorbed energy more efficiently to the HTF. Although air showed the highest values of heat transfer efficiency, the useful energy absorbed by the HTF is low for this configuration. Additionally, there was a reduction in the amount of energy absorbed by the HTF with increasing mass flowrate.
- The lowest values of Levelized Cost of Heat (LCOH) and Simple Payback Period (SPP) were observed in the collector configuration using thermal oil as the filling fluid and with the lowest HTF mass flowrate, indicating that this was the best configuration in economic terms.
- The particle diameter directly influenced the temperature of the packed bed during the charging and discharging processes due to its impact on the specific surface area for heat exchange. Additionally, the use of materials with lower thermal conductivity led to an increase in the temperature difference between the heat transfer fluid (HTF) and the solid material.
- The use of different materials in multilayer configurations increased the charging and discharging times compared to the single material cases. However, the effect of particle sizes on the final times was not as evident.
- The multilayer configuration had a greater influence on the stored (Q_C) and released (Q_D) thermal energy than the particle diameter. Additionally, the favorable effect of using a combination of multilayers with varying particle sizes was also confirmed. Case 9 showed an increase of approximately 7.7% and 3.4% for Q_C and Q_D, respectively, compared to the single material and diameter reservoir (case 1).
- Compared to cases with a PBTES composed of a single material, an increase in charging and discharging efficiency and overall system efficiency was observed for all cases where the PBTES was evaluated with layers of different materials. Compared to case 1, case 9 exhibited approximately 9.5%, 4.0%, and 13.9% higher charging and discharging efficiency and overall system efficiency, respectively.
- The multilayer configuration and variable particle diameter influence the thermal performance of the PBTES from a second law perspective. The exergetic efficiency observed in case 9 was approximately 9.0% higher than that observed in the reference treatment (case 1). Furthermore, it is approximately 7.7% higher than case 5, which has

the same configuration regarding the storage materials and equal diameters for all layers.

- Cases 6 for charging and 9 for discharging, composed of the same configuration related to the HTF inlet, namely concrete (0.02 m), quartzite rock (0.03 m), and cast iron (0.04 m), provided lower temperature gradients in the PBTES and generally had the smallest values for the thermocline thickness. It was also observed for these cases that the MIX number remains below 0.5 for approximately 43% of the total charging/discharging time. This time is approximately 10% longer than that observed for the reference treatment (case 1) in both processes.

The agricultural sector has a significant demand for thermal energy, which is utilized as process heat in various operations. The drying process accounts for a substantial portion of the total energy consumption in this sector. The technologies addressed in this study offer great potential to meet this energy demand by utilizing solar thermal energy. It has been demonstrated that the investigated U-tube CPC can absorb a significant amount of solar energy concentrated by the reflective surfaces onto the central tube. By directing this energy to the PBTES, it can be stored during periods of high solar incidence and used during intermittent periods, ensuring a continuous energy supply. These technologies are highly versatile and can be easily integrated into different agro-industrial processes, including drying. Additionally, their modular nature allows for adaptation to varying sizes and configurations, offering greater flexibility in design and application. Consequently, a drying system comprising the coupling of the U-tube CPC, PBTES, and the dryer emerges as an efficient, sustainable, and versatile alternative for this application. It is important to emphasize the need for future investigations to experimentally evaluate the performance of this system under uncontrolled environmental conditions. Furthermore, environmental assessments should be conducted to evaluate the ecological impacts associated with the construction and operation of the proposed system.